NTNU
Norwegian University of
Science and Technology

Master's thesis

2022

Andreas Rosnes

Master's thesis

NTNU
Norwegian University of
Science and Technology
Faculty of Natural Sciences
Department of Physics

Andreas Rosnes

TEM Study of Cr, N Codoped TiO_2 Thin Film

Structural Properties of Continous Compositional Spread Film

June 2022

NTNU
Norwegian University of
Science and Technology

NTNU
Norwegian University of
Science and Technology

TEM Study of Cr, N Codoped TiO_2 Thin Film

Structural Properties of Continous Compositional Spread Film

Andreas Rosnes

Master of Science Physics
Submission date: June 2022
Supervisor: Randi Holmestad
Co-supervisor: Turid Reenaas and Hogne Lysne

Norwegian University of Science and Technology
Department of Physics

Abstract

The Solar Cell Physics group at NTNU is exploring the concept of intermediate band materials for high-efficiency solar cells. Cr,N codoped TiO_2 is a proposed candidate, however, the ideal doping concentration is not determined. The group thus grows films with continuous compositional spread (CCS) by combinatorial pulsed laser deposition (c-PLD) to speed up the search. The spread is obtained by letting TiO_2 and CrN plumes deposit at two different locations at a controlled distance in the c-PLD process. The CCS film is grown on a 2" Si (100) wafer, and has a Cr and N spread between 2.2 to 9.4% for the region studied in this thesis. The thesis work aims to study the influence of increasing doping concentration and other deposition parameters on the structural properties. Seven cross-sectional lamellae were prepared by focused ion beam in a series across the wafer center line, while an additional two were prepared in a series perpendicular to it. Conventional transmission electron microscopy together with scanning precession electron diffraction were used for characterization.

The characterization by the transmission electron microscope (TEM) showed that the structural properties vary continuously across the CCS film. From the series parallel to the wafer center line at the first plume center, the structure is polycrystalline with a dominant preference for {100} and {110} rutile planes stacked parallel to the substrate. The preference occurs in the early stages of growth. The crystalline regions results from columnar growth, with columns consisting of smaller crystalline grains and showing moiré effects. Anatase is also found locally in the CCS film. At the wafer center, the CCS film is amorphous with growth of inverse crystalline cones. At the second plume center, nanocrystalline columns grow within an amorphous film. These columns disappear across the series perpendicular to the wafer center line.

One can conclude from the TEM study that the growth conditions and dominating processes vary continuously across the film. Along the wafer center line, one parameter clearly increases the energy barrier for crystal growth as the structure goes from a crystalline to an amorphous structure. From the series perpendicular to the wafer center line, one can conclude that the growth of the nanocrystalline columns are sensitive to the position in relation to the plume centers. As the structural properties vary continuously, the transmission electron microscope is an effective technique for revealing the results of local structural variations within the CCS film.

Sammendrag

Solcellefysikkgruppen ved NTNU utforsker konseptet for mellombåndmaterialer for anvendelse i høyeffektive solceller. Kr,N dopet TiO_2 er en foreslått kandidat, men den ideelle dopingkonsentrasjonen er ikke bestemt. Gruppen gror derfor prøver med en kontinuerlig komposisjonsspredning (CCS) med kombinatorisk pulserende laseravsetning (c-PLD) for å søke mer effektivt. Spredningen er oppnådd ved å la TiO_2 og KrN plymer avsettes ved forskjellige lokasjoner ved en kontrollert avstand under c-PLD prosessen. CCS filmen er grodd på en 2" Si (100) wafer, og har en Kr og N spredning mellom 2.2 og 9.4% i området som er studert. Arbeidets mål er å studere innflytelsen av økt dopingkonsentrasjon og andre avsetningsparametere på de strukturelle egenskapene. Syv tverrsnittlameller er forberedt med fokusert ion-stråle i en serie på tvers av waferlinjen, i tillegg er to ekstra lameller forberedt i en serie perpendikulært på waferlinjen. Konvensjonell transmisjonselektronmikroskopi sammen med skannende presserende elektron diffraksjon er teknikker brukt for karakterisering.

Karakterisering fra transmisjonselektronmikroskopet (TEM) viser at de strukturelle egenskapene varierer på tvers av CCS filmen. Ved første plymesenter er strukturen polykrystallinsk med en preferanse for {100} og {110} rutil plan stablet parallelt med substratet. Preferansen tar sted i de tidlige vekstfasene. De krystalline områdene er av søyle-formet vekst bestående av mindre krystallitter og moiré effekter. Anatas strukturen er også tilstede lokalt i filmen. Ved sentrumet i waferen er filmen amorf med vekst av inverse krystalline kjegler. Nanokrystalline kolonner vokser ved andre plymesenter i en ellers amorf struktur, men forsvinner på tvers av serien perpendikulært på waferlinjen fra denne posisjonen.

En kan konkludere fra studien at vekstbetingelsene og de dominerende vekstprosessene varierer kontinuerlig på tverrs av filmen. Fra serien parallelt med waferlinjen kan man konkludere at en av parameterne tydelig øker energibarrieren for krystallinsk vekst ettersom strukturen går fra krystallinsk til amorft. Fra serien perpendikulært til waferlinjen kan man konkludere at veksten av nanokrystalline kolonner er sensitive til posisjonen i forhold til plymesenterne. Ettersom de strukturelle egenskapene varierer kontinuerlig så er transmisjonselektronmikrosopet et effektivt verktøy for å avdekke resultatene som viser lokale variasjoner innad i filmen.

Acknowledgements

The thesis is my final contribution to the MSc of Physics degree at the Department of Physics at NTNU, Trondheim. The work is a collaboration between the Solar Cell Physics and TEM Gemini group, and has been supervised by Professors **Randi Holmestad** and **Turid Reenaas** together with PhD candidate **Hogne Lysne**. I want to acknowledge darely their guidance during my thesis work. Your insight, feedback and passion for the project have been an inspiration, and truly facilitated for me to do my best work. The lessons I have learned through our discussion will stay with me on my road going forward. I believe you have prepared me well. Thank you.

Bjørn Soleim and **Emil Frang Christiansen**, thank you for the training at the TEM instrument, and answering all my questions along the way. I want to note a special thanks to Emil for operating the instrument during the SPED experiments, and for providing me with guidance and assisting codes for the data analysis. The TEM group as a whole is also highly appreciated for the interest in my thesis, and for its professional and healthy work environment. Additionally, the thesis work would not be possible without the efficient help of **Kasper Aas Hunnestad** and **Verner Håkonsen** at Nanolab. Thank you for the training and finding solutions to maintenance issues keeping up the pace of my work. Lastly, I want to express an appreciation for the close cooperation in the Solar Cell Physics group. The interesting discussions surrounding our different characterization results, trying to understand the continous compositional spread film structure as a whole, have been energizing. Thank you to the other master students, and PhD candidate **Thomas Brakstad Vågenes**, on this manner.

The work has been of experimental nature and performed within the Research Centre for Sustainable Cell Technology (**FME SusolTech, RCN 257639**). I want to acknowledge the support from the Research Council of Norway for the sponsorship of the Oxide based intermediate band materials project (**RCN 240466**) together with the Norwegian Micro- and NanoFabrication Facility (**RCN 295864**) and the Norwegian Center for Transmission Electron Microscopy (**RCN 197405**) infrastructure at NTNU. Additionally, the **Department of Physics, NTNU**, is acknowledged for the funding of the thesis activities.

Finally, I want to thank my girlfriend, **Siri Stoknes**, family and close friends for love, support and encouragement during the thesis work period.

Andreas Rosnes
NTNU, Trondheim
17th June 2022

Acronyms

4D-STEM Four-dimensional STEM

BFP Back-Focal Plane

BFTEM Bright-Field TEM

BSE Backscattered Electrons

BSS Blind Source Separation

CDFTEM Centered-Dark Field TEM

c-PLD Combinatorial Pulsed Laser Deposition

CCS Continous Compositional Spread

DFTEM Dark-Field TEM

DP Diffraction Pattern

EDS Energy-Dispersive X-Ray Spectroscopy

EELS Electron Energy Loss Spectroscopy

FIB Focused Ion Beam

GIS Gas-Injection System

HRTEM High-Resolution TEM

IB Intermediate Band

IBSC Intermediate Band Solar Cell

ICA Independent Component Analysis

MJSC Multi-Junction Solar Cell

NBD Nanobeam Electron Diffraction

NTNU Norwegian University of Science and Technology

PDF Pair Distribution Function

PLD Pulsed Laser Deposition

PED Precession Electron Diffraction

PCA	Principal Component Analysis
ROI	Region of Interest
SAED	Selected-Area Electron Diffraction
SE	Secondary Electrons
SEM	Scanning Electron Microscope
SIM	Scanning Ion Microscope
SPED	Scanning Precession Electron Diffraction
SVD	Singular-Value Decomposition
TEM	Transmission Electron Microscope
VADF-TEM	Virtual Annular Dark-Field TEM
VBF-TEM	Virtual Bright-Field TEM
VDF-TEM	Virtual Dark-Field TEM
XRD	X-Ray Diffraction

Table of Contents

1 Introduction **1**

2 Materials and Experimental Methods **3**

2.1 Crystalline Materials 3

2.1.1 Basic Crystallography 3

2.1.2 Structural Properties of Different Polymorph of TiO_2 6

2.2 Transmission Electron Microscopy 8

2.2.1 Electron-Matter Interaction: Diffraction 8

2.2.2 The TEM Hardware and Operations Modes 13

2.2.3 TEM Sample Preparation by Focused Ion Beam 19

2.3 Amorphous Materials 21

2.3.1 Pair Distribution Function 21

2.3.2 Experimental Method for Electron Pair Distribution Function 24

2.3.3 Structural Properties of Amorphous SiO_2 and TiO_2 26

2.4 Pulsed Laser Deposition 28

2.4.1 Conventional and Combinatorial PLD 28

2.4.2 Kinetic Energy Driven Film Growth 30

3 CCS Film Growth and Experimental Details **37**

3.1 CCS Film Growth by PLD 37

3.2 Properties of TiO_2 Grown by PLD 39

3.3 TEM Sample Preparation by FIB 44

3.4 Characterization by TEM 50

4 Results and Discussion **53**

4.1 Structural Trends Parallel and Perpendicular to the Wafer Center Line 53

4.2 Column Growth at the First Plume 61

4.3 The Precence of Anatase Locally in the CCS Film 76

4.4 Growth of Inverse Crystalline Cones at the Wafer Center 81

4.5 Quenched Growth Past Wafer Center 88

4.6 Nanocrystalline Columns at Second Plume 89

4.7 Electron PDF Method to Study Amorphous and Nanocrystalline Regions 97

5 Conclusion **104**

6 Future Work **105**

References **106**

A Appendix - Supporting Results **113**

B Appendix - Code for PDF analysis of Amorphous SiO_2 **118**

C Appendix - Tables with d-spacings **124**

D Appendix - Training Issues and Lessons **135**

1 Introduction

The transition to a sustainable and low-emission society requires that we find renewable ways to provide energy that meets out demand as alternatives to conventional fossil fuels. Directly conversion of solar radiation into electrical energy in solar cells has developed into a mature technology since the first silicon solar cell was produced in 1954 [1]. However, these cells are based on single band gap materials and their efficiencies are thus inherently constrained by the Schokley-Quisser limit [2]. It is of interest to construct cells with efficiencies beyond the theoretical limit to reduce the cost per kWh, and make it even more competitive as an energy provider. An additional motivation is to provide energy in areas with limited space, such as in cities and interstellar space. Such cells are referred to as third generation solar cells.

There are different approaches to how one may construct such a cell [3]. An approach is to construct cells with multiple band gaps, which can be achieved in two ways. One option is to design cells which utilize multiple p-n junctions with absorbent layers of different band gaps to harness more of the solar radiance [4]. Radiance from different parts of the solar spectra, can be harnessed at the different p-n junctions, and will thus reduce the transparency and thermalization losses compared to a single p-n junction. Such a cell is referred to as a Multi-Junction Solar Cell (MJSC). However, a high demand is put on the cell design when utilizing multiple p-n junctions. An additional challenge is that MJSCs are often based on non-abundant and toxic materials, making them costly and not sustainable for application [5, 6].

Alternatively, one can base the cells on new materials with new functional properties that have multiple band gaps. An Intermediate Band Solar Cell (IBSC) utilize a wide band gap semiconductor with an energy band located within its forbidden band gap. Higher energy photons can excite electrons across the intrinsic band gap, and lower energy photons can similarly do this in a two-step process via the Intermediate Band (IB). The result is an increased photogenerated current, while the wide band gap provides a high voltage over the cell. As a result, one gets a higher output power than conventional cells. There are three band transitions between the valence band, the IB and the conduction band in an IB material. The efficiency is thus theoretically equivalent to a MJSC with three p-n junctions. The theoretical efficiency for such cells mount to 63.2% if all the available light is concentrated into the cell, which is substantially higher than the efficiency of 40.8% for conventional cells under the same conditions [3]. IBSC is an interesting approach as one potentially utilizes simpler design and reduce the material cost to make it more competitive. The concept has been demonstrated experimentally, but based on toxic materials such as zinc telleruide and quantum dots [7]. Materials with the necessary functional properties and qualities have not yet been developed.

In the Solar Cell Physics group at Norwegian University of Science and Technology (NTNU), the IBSC concept is explored by searching for sustainable materials with IB qualities. One of the approaches that the group is pursuing, is by doping oxide based semiconductors to alter the optical properties. Theoretical studies propose Cr and N codoped TiO_2 as a novel candidate for an IB material [8, 9, 10]. IBSC based on such a material has a theoretical efficiency of 52.7% [11]. TiO_2 is abundant and non-toxic, and together with its wide band gap (3-3.2 eV), a good candidate for host material. This is the motivation for why the group explores the candidacy of Cr, N codoped TiO_2.

The exact doping level is, however, not determined. Pulsed Laser Deposition (PLD) is a flexible and fast physical vapour deposition method that serves well for material development and screening in the search for new materials. The group is utilizing combinatorial setups in so-called Combinatorial Pulsed Laser Deposition (c-PLD) to produce Continous Compositional Spread (CCS) within single films. As a part of the material characterization activity within the research group, this thesis work focuses on studying the local structure by Transmission Electron Microscope (TEM). Specifically, the motivation is to prepare cross-sectional thin membranes, referred to as a lamella, by Focused Ion Beam (FIB) across the CCS film to study the local structural variations as a function of doping concentration and other deposition parameters. The gained insight will be used for further optimized growth by c-PLD, and to link local variations of structural properties to functional performed by other members of the group. The findings are a contribution to the search for sustainable IB materials for high-efficiency solar cells. An additional focus is given to method development within the TEM Gemini group for studying amorphous materials with the Pair Distribution Function (PDF). The thesis work will thus also govern theory, results and discussion for combining TEM and PDF characterization.

The Outline of the Thesis

In the following chapter, **Ch.2 Materials and Experimental Methods**, the relevant theory for the performed work will be presented. The chapter includes characteristic features of crystalline and amorphous materials, the fundamentals of electron diffraction and PDF, the growth modes of PLD and the fundamentals of the FIB, PLD, and TEM instrument. The **Ch.3 Experimental Details** chapter provides details of the experimental methods. It includes parameters for CCS film growth by c-PLD, a detailed guide on the lamella preparation by the FIB, and the experiment details and post-data-processing of the TEM work. The results are presented in **Ch.4 Results and Discussion** for the lamella series parallel and perpendicular to the wafer center line to evaluate the influence of doping concentration and other deposition parameters. In the first section, the results are viewed in a broader context before a section of further details will follow. A third section presents results of characterization by PDF in the TEM. Concluding remarks and suggestions for future work will finish the thesis in the **Ch.5 Conclusion** and **Ch.6 Future Work**, respectively. Supporting results will be included in the **Appendix**.

2 Materials and Experimental Methods

The relevant theory for the performed works is presented in this chapter. It contains a brief presentation of crystalline material followed by a section of the fundamentals of the TEM instrument. A section on amorphous materials and how they can be studied in the TEM will follow, before the principles of conventional and combinatorial PLD together with relevant theory for kinetic energy driven film growth is presented in the last section.

2.1 Crystalline Materials

2.1.1 Basic Crystallography

The following section is based on Ch.1-2 of Kittel and Ch.1 of Hofmann [12, 13]. The citations throughout this section are thus omitted. Basic crystallography is introduced to setup for diffraction theory in the TEM.

Crystalline materials are classified as structures with a periodic arrangement of atoms. A full description of the structure can be broken down by identifying the group of atoms, *basis*, and the evenly grid of points, *lattice*, that they can occupy. A three-dimensional lattice is defined by three translation vectors, $\vec{a_1}$, $\vec{a_2}$, and $\vec{a_3}$, where a translation of an integer combination of these leaves the environment identical for the basis. The lattice vector is presented in eq. (1).

$$\vec{r_g} = m\vec{a_1} + n\vec{a_2} + o\vec{a_3} \tag{1}$$

Here, m, n, and o are arbitrary integers, and $\vec{r_g}$ is the translation vector. Such a lattice is called a *Bravais lattice*, and the uniqueness of its description is limited to 5 and 14 different systems in two- and three-dimensions, respectively. The different lattices are distinguished by the relation between $\vec{a_1}$, $\vec{a_2}$, and $\vec{a_3}$, in terms of length and angle between them, together with the allowed positions of the basis. The combination of lattice and basis which provide a unique description is further classified into seven crystal system which are called *triclinic*, *monoclinic*, *orthorhombic*, *tetragonal*, *cubic*, *trigonal* and *hexagonal*. Triclinic is the most general with no equivalent crystal axes or angles, and cubic the most rigid with all of them equal.

The smallest volume which can, by the translational vectors, expand and occupy all of space is commonly identified in a crystal. This is called the *primitive unit cell*. The basis at the lattice point may contain multiple atoms. Their relation to the lattice points in the system can be expressed as a translation of a fraction of the lattice vectors, and is presented in eq. (2).

$$\vec{r_k} = x_k\vec{a_1} + y_k\vec{a_2} + z_k\vec{a_3} \tag{2}$$

Here $\vec{r_k}$ denotes the location of atom k from the lattice points, and x_k, y_k and z_k are fractions of the lattice vectors, $\vec{a_1}$, $\vec{a_2}$, and $\vec{a_3}$, presented in eq. (1).

A special focus will be given to the tetragonal system since both the most common polymorphs of TiO_2 is described by this system. Here, the base of the structure is a square expanded by two identical vectors, $\vec{a}$, that are different from the height, $\vec{c}$. All angles between them are 90°. There are further two lattice types in this system, *primitive* and *body-centered* denoted by the letter P and I, respectively. The former only contains lattice sites at the corners, while the latter additionally contains one in the center.

Further description of the lattice governs what symmetry operations other than translational, can be carried out which leaves the environment unchanged. Rotational symmetry governs incremental rotations about an axis, and are restricted to 2, 3, 4 and 6 due to their uniqueness and requirement to occupy all of space. A n-rotation axis rotates by 360°/n where $n = 2, 3, 4, 6$. A reflection plane that mirrors the structure, denoted by m, is a mirror symmetry operation. Additionally, one has the identity operation of inverting the structure of its center points, $\bar{n}$, called inversion symmetry. An improper rotation axis where the system is only equivalent after an additional inversion of the center point is called a roto-inversion symmetry operation [15]. The description containing all such symmetry operations in the unit cell, gives the unit cell its *point group*. Figure 1 shows the symmetry operations on a primitive tetragonal lattice, and provides a simple example. The point group is *4/mmm*, where the dashed lines indicate mirror planes, and A_2 and A_4 denotes two- and four-fold rotation axes, respectively. There are 32 unique such point groups across the mentioned crystal systems [15].

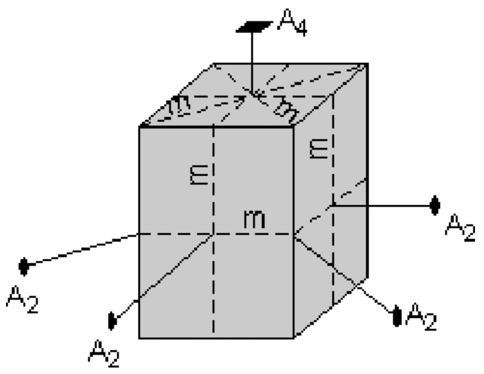

Figure 1: Three-dimensional visualization of point group *4/mmm*. Image adapted from Mascarenhas [14].

For a full description of the crystal, the translational symmetry of the lattice has to be combined with point group symmetry of the unit cell. The combination gives rise to new symmetry operations such as *screw axes* and *glide planes*. There are 230 unique such descriptions in three-dimensional space [15]. The description is called the *Space group* of the crystal, and provides a unique description which can be identified to characterize the crystal structure.

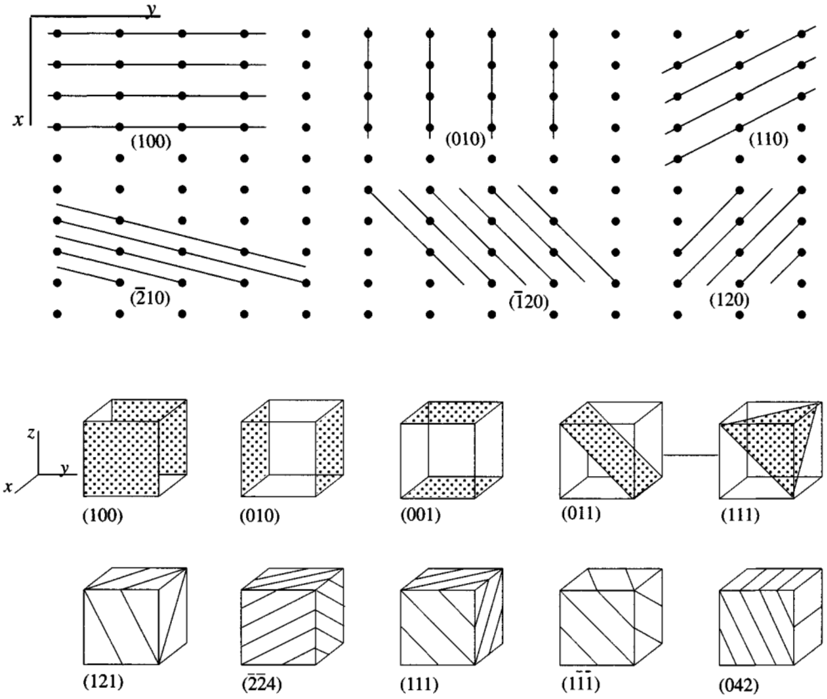

Figure 2: Schematic of two-dimensional crystal lattice (top) with different atomic planes denoted (hkl). There intersection in a cubic unit cell is visualised (bottom) together with planes of higher index numbers. Figure adapted from Putnis [16].

The periodicity of the lattice results in parallel planes of atoms within the structure. A useful description for material characterization is to express how these planes intersect the unit cell. Such a description can be obtained expressing the planes through the Miller indices, h, k and l, which intersect the cell at $\vec{a_1}/h$, $\vec{a_2}/k$ and $\vec{a_3}/l$ in a general system. The indices are thus the reciprocal of the intercept of the cell. Figure 2 visualises such atomic planes in a two-dimensional lattice together with how they intersect a cubic unit cell in three-dimensions. The interplanar spacing between such planes in a tetragonal system is given by eq. (3).

$$\frac{1}{d_{hkl}^2} = \frac{(h^2 + k^2)}{a^2} + \frac{l^2}{c^2} \tag{3}$$

Here, d_{hkl} is the interplanar spacing of the planes denoted by the Miller indices (hkl), while a and c are the lattice constant of the base and the height of the tetragonal lattice, respectively. A set of planes is denoted (hkl) whereas a family of planes that are equivalent by symmetry is expressed {hkl}. Additionally, a certain set of planes will be parallel to the crystallographic direction in which one is viewing the structure. This governs the *zone axis*, and is denoted by [hkl]. Zone axes which are equivalent by symmetry are expressed <hkl>. Crystals thus contain a frequency of evenly spaced atomic planes. The Bravais lattice may thus be described in frequency space as well through a fourier transform, and this alternative description is called the reciprocal lattice, and is similarly described by a set of integers, {m', n', l'}, and vectors, $\{\vec{b_1}, \vec{b_2}, \vec{b_3}\}$, expressing how the lattice points are distributed. The reciprocal lattice vector is presented in eq. (4).

$$\vec{g} = m'\vec{b_1} + n'\vec{b_2} + o'\vec{b_3} \tag{4}$$

The relation between $\vec{r_g}$ and $\vec{g}$ for the two descriptions is that $\vec{r_g} \cdot \vec{g} = 2\pi l$ where l is an integer. The relation tells us that the vectors are perpendicular to each other, and thus also the plane of atoms and the direction of the reciprocal lattice points. The relation between the two lattices will be useful for electron diffraction presented later.

It is, however, extremely rare in nature that crystals are perfectly periodic as they extend to the nano- and microstructure scale. Deviation from ideal crystals results in points, lines, planes and volume defected regions. Individual crystalline regions may be separated, making the material *polycrystalline*. Defects introduce local disturbance, and may lead to deformation and decrystallization of the structure.

2.1.2 Structural Properties of Different Polymorph of TiO_2

TiO_2 can exist in three phases at atmospheric conditions, making it a polymorphic structure. The different phases are named *rutile*, *anatase* and *brookite*. Rutile is the most stable phase as it holds the lowest Gibbs free energy which makes it favorable as a bulk structure. The other two are metastable, and will transition into rutile except for at low temperatures under thermodynamic equilibrium [17]. Brookite is highly unstable, and not identified in the results of this thesis. It is thus not further introduced.

Both structures have a tetragonal unit cell. However, they differ significantly as the base of rutile is larger than that of anatase while its height is shorter. The lattice constants of the former are a = 4.5936 Å and c = 2.9587 Å, while the latter are a = 3.784 Å and c = 9.515 Å [18]. The tetragonal shape of the unit cell is thus truncated along the c-axis, while that of anatase is elongated compared to a cubic cell. Their unit cells are visualised in Figure 3 where both belong to the *4/mmm* point group introduced in Figure 1. Their space groups, however, differ. They are $P4_2/mnm$ and $I4_1/amd$ for rutile and anatase, respectively, and reveal a difference in their lattice type where rutile contains a primitive (P) while anatase contains a body-centered (I). They also differ in terms of the type and position of their screw-axis and mirror planes.

The two phases also differ in terms of the number of atoms in their unit cells, which is referred to as the *formula units*, and is denoted by the letter Z. One formula unit of TiO_2 consists of one Ti atom, and two oxygen. The formula unit of rutile and anatase is two and four, respectively. The rutile structure thus have two Ti and four O atoms in its unit cell, while anatase has four Ti and eight O. The density of the rutile unit cell is thus only slightly larger even though the volume of the unit cell of anatase is greater [18].

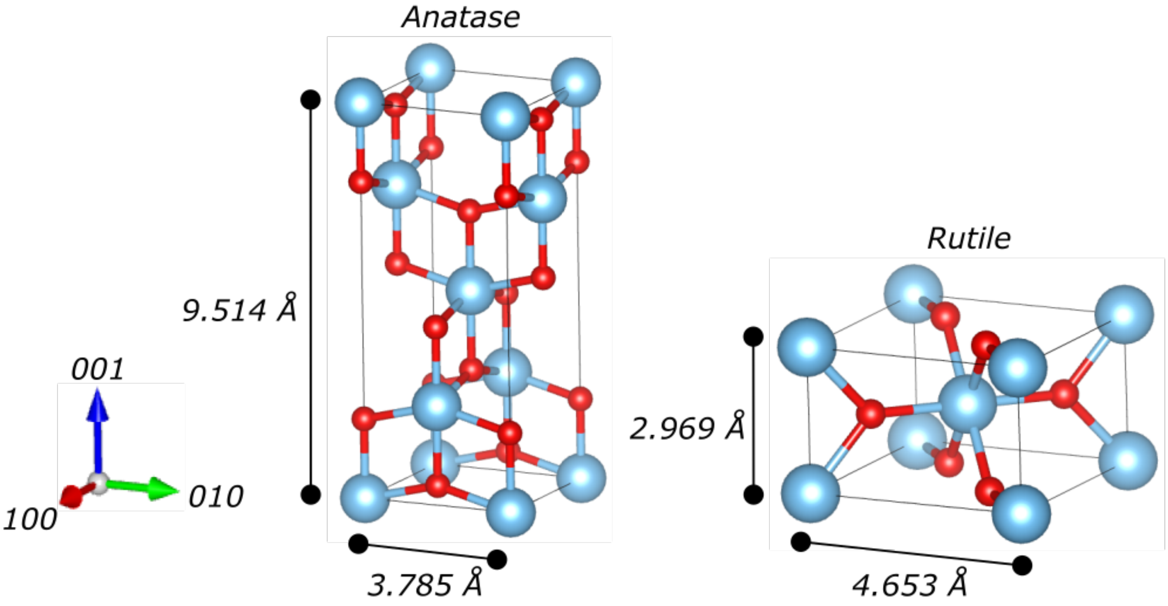

Figure 3: The tetragonal unit cell of anatase and rutile are visualised. The Ti (blue) and O (red) atom make up the structure, and are linked with their bonds visualized. Their lattice spacing are presented. Figure made in Vesta [19].

Both structures can be considered as an ordering of Ti atoms at lattice sites surrounded by an octahedral arrangement of O atoms. An alternative way to view the structure is through the stacking of the oxygen atoms. The oxygen atoms of anatase and rutile order in a closest three layer (ABCABC...) and hexagonal two-layer (ABAB...), respectively. The Ti atoms in both structure occupy half of the octahedal sites [20]. The resemblance between the stacking of the oxygen atoms, results in planes which are equivalent in nature. The {100} and {112} planes of rutile and anatase, respectively, show the closest packing of the oxygen atoms [21]. Since they are similar in nature, parallel stacking of these planes are commonly observed in materials where both the phases are presence [17]. A specific crystallographic orientation relation has been observed equivalent to ($[110]_{\mathrm{A}}||[011]_{\mathrm{R}}, \{112\}_{\mathrm{A}}||\{200\}_{\mathrm{R}}$) [21], where the planes are stacked parallel when viewed down the [110] axis of anatase, and the <011> of the rutile structure simultaneously. Other orientation relationships are also documented [22].

2.2 Transmission Electron Microscopy

2.2.1 Electron-Matter Interaction: Diffraction

The TEM instrument sends in a high energy and focused electron probe to interact locally with the matter in the material. As the electrons of the probe propagate through the material, a variety of different interactions may occur as visualized in Figure 4. The electrons interact strongly with both the electron cloud and the nucleus of the atoms through the Coulomb force, which is why the signal is so diverse. The different signals are typically classified into whether energy is conserved or not, *elastic* or *inelastic*, and whether the phase of the wave nature is conserved or not, *coherent* or *incoherent*. Generally, elastic scattered electrons are coherent, and inelastic are incoherent [23].

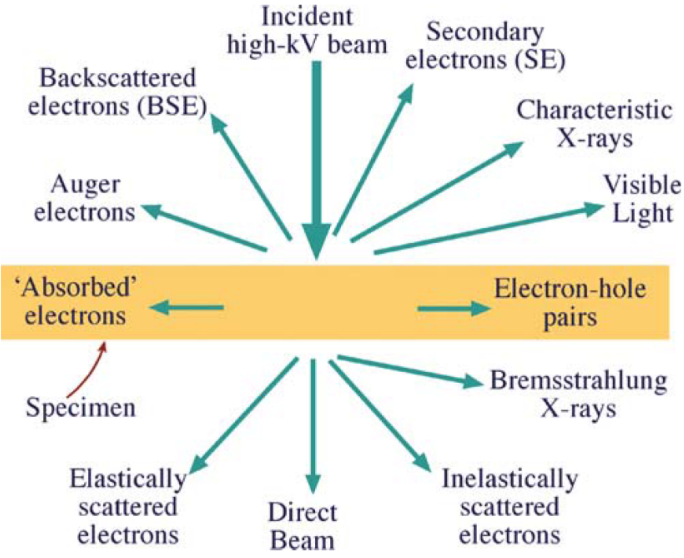

Figure 4: Visualization of the cascade of different outgoing signals from the interactions between the incoming high-energy electrons with the matter. See section 2.2.1 for description of the different interactions and their uses. Image adapted from Williams and Carter [23].

The electrons can transfer energy to the atom by exciting bound electrons to a higher energy state, such that the reverse relaxation into the initial stage occurs together with an omitted characteristic x-rays. The outgoing characterisitc x-rays can be collected and used for chemical mapping by Energy-Dispersive X-Ray Spectroscopy (EDS). The electrons can also knock weakly bound outer shell electron out of their orbit. The electrons are referred to as *Auger electrons*, and close to the surface they may have sufficient energy to escape, and can thus be used for imaging of the topological features. Both interactions result in an energy loss of the electrons of the probe, and correspond to inelastically scattered electrons. The electrons that scatter inelastically and transmit through the material, can be collected by a detector to perform Electron Energy Loss Spectroscopy (EELS), which thus contains chemical information of the structure. EELS and EDS are commonly referred to as analytical TEM.

Conventional TEM techniques utilize scattered electrons, and are of the most importance for this work. When the electrons scatter off an atom, then the scattering amplitude of the outgoing wave is a result of the *atomic form factor*, f_{at}, of the scattering object, and is expressed by the Mott formula in eq. (5).

$$f_{at}(\Delta k) = \frac{2me^2}{\hbar^2 \Delta k^2} * (Z - \int_{-\infty}^{\infty} \rho(r) \mathrm{e}^{-i\Delta k \cdot r} \, d^3 r) \tag{5}$$

In eq. (5), m and e are the electrons mass and charge, respectively. $\hbar$ is Planck's constant. Z is the atomic number, and the integral governs the spatial extension of the electron density, $\rho(r)$. Δk is the change in wavevector as a result of the scattering event.

Rutherford scattering governs elastic scattering of the nucleus. The angular distribution of scattering from an atom in Rutherford scattering, is given by the differential cross section, $\frac{d\sigma_R}{d\Omega}$, which indicates how many electrons scatter into a specific scattering and solid angle. Close to the nucleus, the screening of the electrons is negligible, and the f_{at} reduces to only the contribution from the nucleus. Eq. (6a) is eq. (5) reduced by the contribution from the electron cloud, whereas eq. (6b) is the more common form obtained when neglecting quantum mechanical effects [24].

$$(a) \quad \frac{d\sigma_R}{d\Omega} = |f_{at}|^2 = \frac{4Z^2 e^4 m^2}{\bar{h}^4 \Delta k^4} \quad \longrightarrow \quad (b) \quad \frac{d\sigma_R}{d\Omega} = \frac{Z^2 e^4}{16E^2 \sin^4(\theta)} \tag{6}$$

The variables in eq. (6a) was defined in eq. 5, while E is the kinetic energy of the electrons, and θ is the scattering angle. Rutherford scattering is collected at large scattering angles, and as the scattering scales quadratically with the atomic number, the intensity variation here can provide information about the elements present. Elements of higher atomic numbers scatter to larger angles.

The electrons may even be backscattered, and escape from the same surface of the incoming probe. The Backscattered Electrons (BSE) can be collected to form an image of the topological features with elemental contrast. The incoming probe, or any electron traveling towards the incoming surface, can knock electrons out of their shell. Such electrons are low in energy, and only the near surface electrons may escape. These Secondary Electrons (SE) can be utilized for high resolution images of the topological features. Both these signals are commonly used in lower energy electron microscopes, such as in the Scanning Electron Microscope (SEM). The former has a greater interaction volume than the latter, in addition to containing elemental information.

Diffraction in Crystals: The atomic distribution in crystals presents a periodic array of scattering objects for an incoming plane-wave, and provides a similar scattering object to a grating. The scattered waves can therefore interfere constructively and destructively. The wave phenomenon, called *diffraction*, is a useful tool for studying crystal structures, and is important for characterization by the TEM. The final intensity distribution, the Diffraction Pattern (DP) is well captured by Bragg's law in eq. (7) considering that incoming waves scatter specularly of the crystalline planes according to Snell's law [24]. Neighbouring atomic planes will interfere constructively when the difference in path length equals an integer number, n, of the wavelength, λ, and destructively otherwise. The DP thus provides strong peaks whose spacing's provide insight into the lattice spacing, d, and can be used to identify the crystal structure.

$$2d \sin\theta = n\lambda \tag{7}$$

Here, θ, is the angle between the incoming wavevector, $\vec{k}$, to the lattice planes, and d is the interplanar spacing presented in eq. (3) for a tetragonal lattice. A plane which provides constructive interference is said to be *in Bragg*. The Bragg approach is sufficient to explain the angle for the scattering of the electrons, but insufficient to capture the physical nature of the interaction. Huygens' principle describing the outgoing wave as a summation of smaller wavelets combining into a wave front provides a more correct physical picture for diffraction [24]. The Laue approach captures this, and is thus more correct for electrons in the TEM. Electron diffraction according to Huygen' principle is visualised in Figure 5.

A criterion for the Laue approach is that the energy and phase of the electrons are conserved. A wavefront scattering of an atom pair separated by a distance, $\vec{r}$, will similarly to the Bragg approach interfere constructively if the difference in path is equal to an integer of the wavelength, $\vec{r} \cdot (\vec{k_f} - \vec{k_i}) = 2\pi n$. Here, $\vec{k_f} - \vec{k_i}$ is the change in vector, which is further denoted Δk. The criterion has to hold for the crystal at large, and the description of our lattice and basis as introduced in section 2.1.1 is thus very helpful for diffraction of crystals.

The distances separating the atoms in a perfect crystal are expressed by the lattice vectors, r_g, and the vectors expressing the distribution of the atoms in the basis, r_k. The sum can thus be separated into two contributions - one for the lattice and one for the basis. They are called the shape, S, and structure factor, F, and are presented in eq. (8a) and eq. (8b), respectively.

$$(a) \quad S(\Delta k) = \sum_{r_g}^{lattice} \mathrm{e}^{-i2\pi\Delta k \cdot r_g} \qquad (b) \quad F(\Delta k) = \sum_{r_k}^{basis} f_{at}(r_k)\mathrm{e}^{-i2\pi\Delta k \cdot r_k} \tag{8}$$

As the basis is located at each lattice site, the scattered wave can be expressed as the sum of wavelets

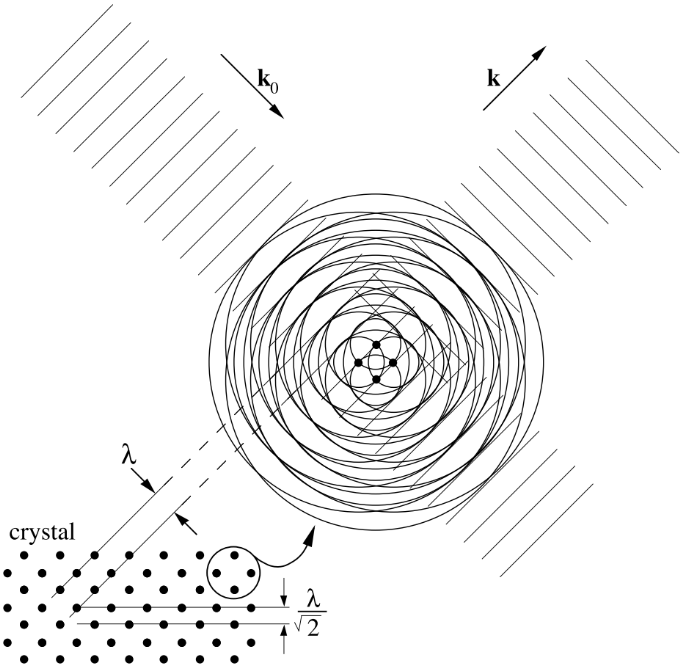

Figure 5: Schematic visualization of electron diffraction in crystals according to Huygens' principle. Constructive interference occur when the change in path length is equal to an integer of the λ. Planes separated by $\lambda/\sqrt{2}$ result in constructive interference at a 45° angle. Image adapted from Fultz and Howie [24].

scattering of the structure factor at each lattice site as expressed in eq. (9a). The intensity of the reflections from these waves is a complex conjugate of the diffracted wave as described in eq. (9b), and the maximum value occurs when the exponential is equal to zero.

$$(a) \quad \Psi(\Delta k) = S(\Delta k)F(\Delta k) = \sum_{r_g}^{lattice} F(\Delta k)\mathrm{e}^{-i\Delta k \cdot r_g} \quad \longrightarrow \quad (b) \quad I(\Delta k) = |\Psi^*\Psi| \tag{9}$$

What becomes evident in eq. (9a), is that the diffracted wave is proportional to the fourier transform of the scattering factor distribution in the material. Here, distinct reflections occur at locations when the change in Δk, is equal to one of the reciprocal lattice vectors, g. This occur at the Laue condition for diffraction, and is presented in eq. (10).

$$\Delta k = g \tag{10}$$

Specific combinations of the Miller indices thus provide us with a description for when the condition is satisfied, and give rise to allowed and disallowed reflection conditions. The resulting pattern depends on the orientation of the projection vector as the planes have to be orthogonal to this direction to be *in Bragg*. Diffraction of crystals thus provides a fourier transform of the crystal structure, and is the reciprocal lattice with constructive interference at $\vec{r_g} \cdot \vec{g} = 2\pi l$.

The Ewald Sphere: The Ewald sphere is a geometrical construct which visualizes when the Laue condition is satisfied. By letting the incident wavevector, k_0, intersect the (000) reflection for the transmitted beam, then diffraction occurs whenever the scattered wavevector, k, intersects a lattice point. Considering elastic scattered electrons, the magnitude of the wavevectors are equal, $|k_0| = |k|$. One can thus draw a circle whose radius equals the magnitude of the wavevector, and whenever this circle touches a point on the reciprocal lattice, then the Laue condition for diffraction is satisfied [24].

The interplanar spacings are small compared to the wavevector of the high-energy electrons [24]. The radius of the Evald sphere is thus large, compared to the distance to the neighbouring reciprocal lattice points. Δk for when the Ewald sphere intersects a lattice point is thus almost perpendicular to k_0 in reciprocal space. In this direction, the TEM sample geometry is thin in order for the electrons to transmit, and the crystal thus occupies only a small finite volume. The shape of the crystals is expressed through the shape factor, $S(\Delta k)$, introduced in eq. (8). The fourier transform of S, thus broadens the points of our reciprocal lattice as the crystal occupies a finite volume. The broadened reflections are commonly referred to as *relrods*. According to Laue, diffraction occur when the Evald sphere intersects a lattice point in our reciprocal lattice. Since these points are braodend to rods, one does not need to be exactly at a reciprocal lattice point for diffraction to occur. One can thus define an excitation error, s, for how far away one is from the reciprocal lattice point ($g = \Delta k + s$).

Diffracted Beams: Here, one will see that s is a very important parameter for the intensity of the diffracted beam. By considering only two beams, the direct and diffracted beams denoted I_0 and I_g, respectively, one can see that their intensities are correlative as the electrons travel through the specimen. The relation between the two beams are presented in eq. (11a). The intensities vary as they repeatedly interact with atoms via the Coulomb forces. The I_g varies periodically through the thickness, t, of the specimen according to the Howie-Whelan equation presented in eq. (11b) [23].

$$(a) \quad I_0 = 1 - I_g \quad \Longrightarrow \quad (b) \quad I_g = (\frac{\pi t}{\epsilon_g})^2 \cdot \frac{\sin^2(\pi t s_{eff})}{(\pi t s_{eff})^2} \quad where \quad s_{eff} = \sqrt{s^2 + \epsilon_g^{-2}} \tag{11}$$

Here, ϵ_g is the extinction distance and s_{eff} is the effective excitation error. The former is the distance of one period of the intensity oscillation, and the latter is a corrected excitation error. The intensity variation is a result of multiple scattering events, and is important for imaging of the specimen as the electrons leave the sample.

Kinematic versus Dynamical Theory: The introduced theory for electron diffraction, except for the Howie-Whelan equation, assumes a single scattering event for each electron. Scattering according to such a theory is typically referred to as kinematical, whereas multiple scattering events are commonly referred to as dynamical. An electron is likely to scatter off atomic planes during its path through the specimen. A dynamical effect is thus *double diffraction* which results in a redistribution of the intensity which may alter the reflection conditions. A forbidden reflection may be allowed through a combination of scattering events. A detailed dynamical theory of crystalline materials goes beyond the scope of this thesis, but a basic understanding is important for the thesis work.

2.2.2 The TEM Hardware and Operations Modes

The following section section is based on the Williams and Carters textbook Ch.9 and section 18.8 [23]. The citations throughout this section are thus omitted.

The TEM hardware can be separated into three components - the illumination system, the objective lens, and the imaging system. The electrons are first accelerated to high energies by an electron gun. The aim of the illumination system is to prepare the electrons for the interaction with the specimen. It contains two condenser lenses, which primarily either prepare a broad and parallel beam, or a focused and convergent one. The objective lens and stage are where the specimen is inserted, and thus where the electron-matter interaction takes place. It is inserted inside a polepiece in the objective lens, and the quality of the lens determines the resolution and contrasts of the final image. Here, quality is determined by any aberrations in the lens resulting in distortion of the image. The objective lens collects the outgoing electrons to either form a DP in the Back-Focal Plane (BFP) or an image in the image plane. The imaging system then magnifies these signals and display them on a viewing screen.

Selected-Area Electron Diffraction: A Selected-Area Electron Diffraction (SAED) utilizes a parallel beam to form a DP on the viewing screen from a limited area of the specimen. Such a pattern can be formed by placing a selected-area aperture in the image plane of the optical column such that only electrons scattering from this region will form the DP on the viewing screen. A ray-diagram within the illumination system of the TEM is presented in Figure 6 to visualize the fundamentals of the SAED technique.

Bright-Field TEM: An image can be prepared on the viewing screen by altering the strength of the lenses in the imaging system as seen in Figure 7 (a). A common technique is to utilize a SAED pattern on the viewing screen to choose which reflections in the DP that one wants to form an image from, and thus be able to increase contrast between regions of the direct and scattered beam. The technique can be performed by placing an objective aperture in the BFP. If one places the objective aperture around the center beam, then one obtains an image of only electrons which have not scattered to an angle. The technique is referred to as Bright-Field TEM (BFTEM) imaging, and is visualized in Figure 7 (b).

Dark-Field TEM: Conversely, by placing the aperture around a distinct reflection, then one can trace the scattered electrons back to the region in which they scattered from, and form an image. This is called Dark-Field TEM (DFTEM) imaging, and is visualized in Figure 7 (c). By choosing a reflection directly, then some of the electrons will travel off the optical axis, and thus experience uneven aberrations and astigmatism. The distortion of the image can be avoided by tilting the incident beam to center the reflection of interest. The technique is called Centered-Dark Field TEM (CDFTEM), and is visualized in Figure (d). The tilting can be performed by scanning coils which deflect the electrons prior to the interaction with the specimen.

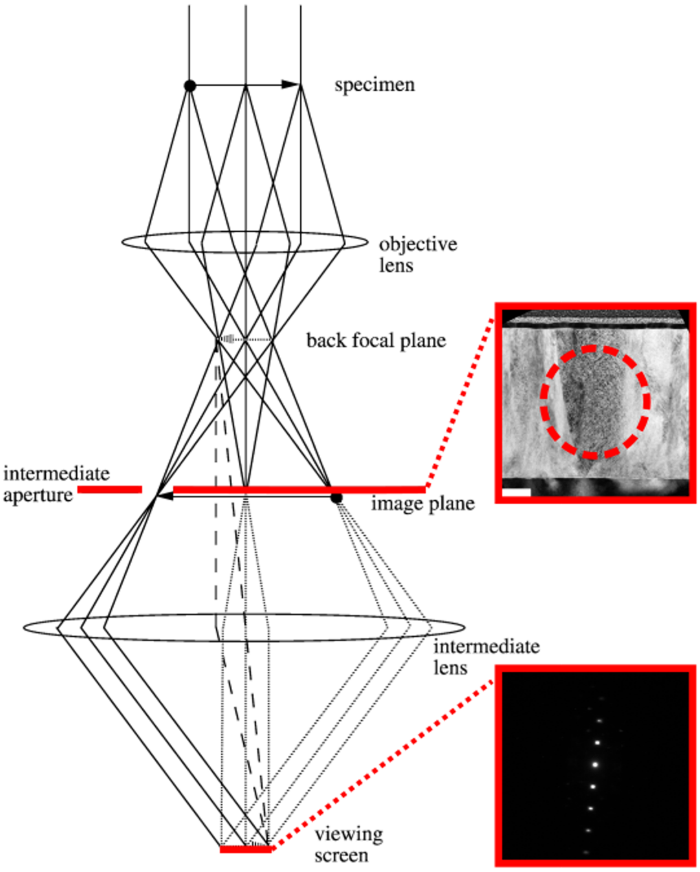

Figure 6: Schematic ray-diagram within the illumination system of the TEM for the SAED technique. A parallel beam is prepared by the optical column and interacts with the specimen in the top part of the image. The objective lens then forms a DP in the BFP. By placing a selected-area aperture in the image plane, one can select an area which the electrons in the DP scatter from. Image adapted from Fultz and Howie [24].

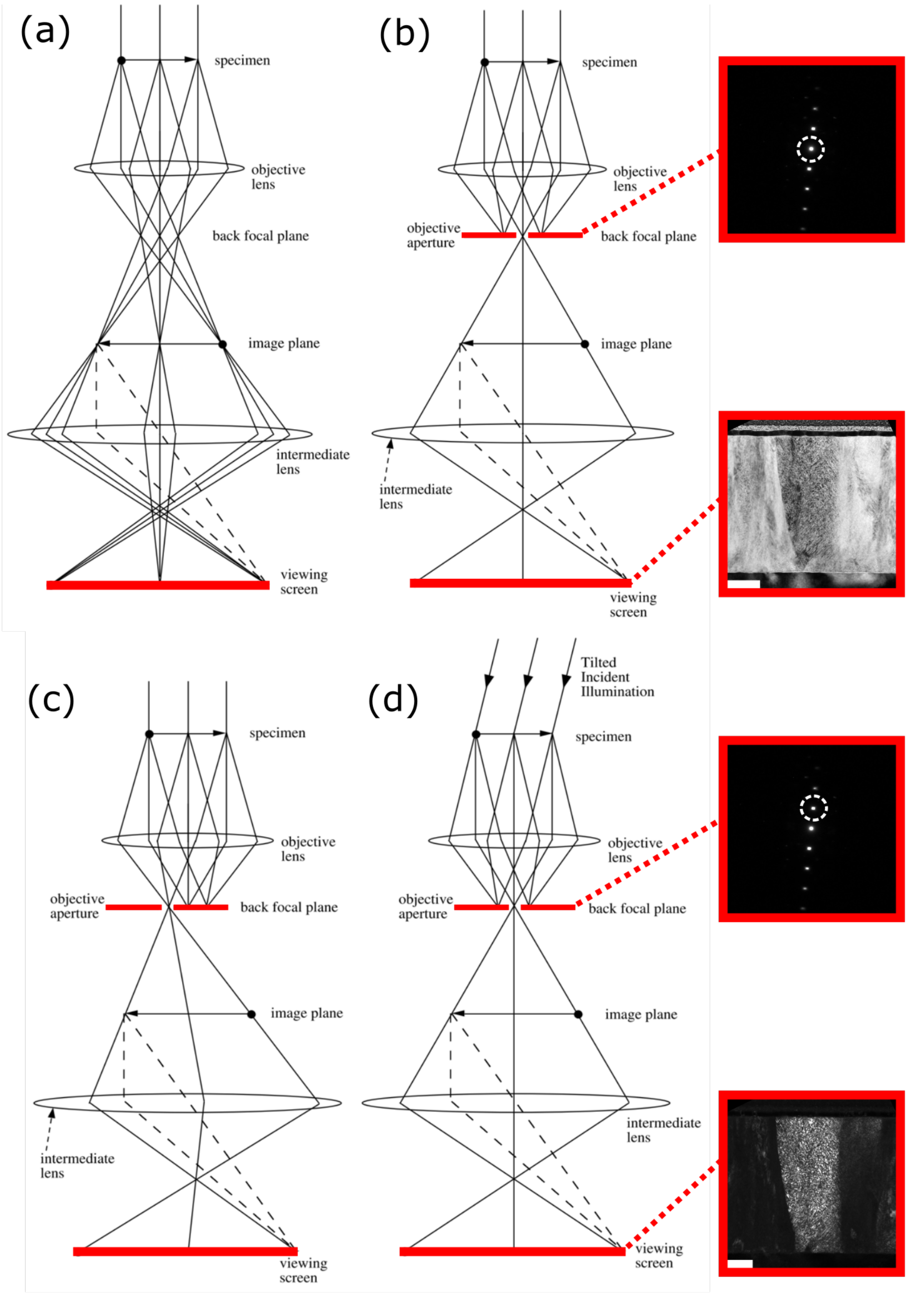

Figure 7: Schematic ray-diagrams within the illumination system of the TEM for different imaging techniques. (a) The illumination system can prepare the scattered signal to form an image on the viewing screen. By placing an objective aperture in the BFP, then one can obtain an image only from the direct beam, and thus increase the contrast between the direct and scattered regions, resulting in a (b) BFTEM image. Similarly, one can place the aperture around a reflection to form a (c) DFTEM image only of the electrons scattering to this angle. To reduce aberration and astigmatism, one can tilt the incident beam to make the electrons travel on the optical axis, as in (d) CDFTEM. Image adapted from Fultz and Howie [24].

Scanning Precession Electron Diffraction: Precession Electron Diffraction (PED) takes the tilting an extra step by simultaneously rocking the beam around a center axis prior to the specimen interaction, and de-scan it after onto the BFP to focus the reflections to spots again. The basic mechanisms are visualised in Figure 8. As one precesses, one changes the diffraction conditions, which means that one is effectively rocking the Ewald sphere in reciprocal space. One can thus integrate over the Bragg condition by collecting the intensities from multiple tilt angles into one DP. In this way, one can average out dynamical effects. De-rocking is commonly combined with a nanosized probe for Nanobeam Electron Diffraction (NBD). The scan coils can simultaneously be utilized to shift the location of the focused electron beam. One can stepwise raster over a larger area, and collect a precession DP pattern at each step. Such an experiment is referred to as Scanning Precession Electron Diffraction (SPED). An experiment where one picks up a DP at each step over a scanned region is commonly referred to as a Four-dimensional STEM (4D-STEM) experiment, where SPED is a subgroup of this group.

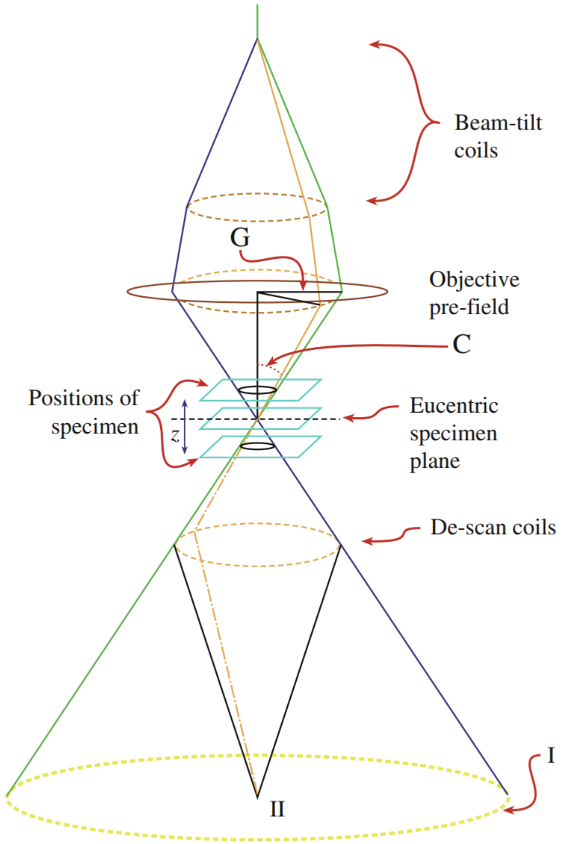

Figure 8: Schematic of the SPED technique. The beam is tilted of the optical axis (C), and precessed at the objective prefield (D) such that cross-over of the convergent beam is located at the eucentric specimen plane. After the interaction it is de-scanned onto the BFP to form distinct reflections in the DP. Image adapted from Williams and Carter [23]

Virtual TEM and Data Processing: An experiment such as SPED provides a four-dimensional datacube as the scanned image contains a two-dimensional DP in each pixel. The large stack of DPs can be utilized to perform virtual TEM experiments in post-data processing steps. In analog to BFTEM and DFTEM, one can place a virtual aperture around the direct and scattered beams to produce Virtual Bright-Field TEM (VBF-TEM) and Virtual Dark-Field TEM (VDF-TEM) images, respectively. One can then form an image in the scan with weighted intensity similarly to a performed physical experiment in the TEM. Alternatively, one can utilize an annular aperture to integrate over the radial dependence to obtain a Virtual Annular Dark-Field TEM (VADF-TEM) image. Such an aperture can be very useful in materials with no preferred orientation, such as in amorphous or polycrystalline structures.

Unsupervised Machine Learning: The datacube from a SPED experiment contains a large amount of data extending to a couple of gigabytes and a hundred thousands of DPs. Depending on the specimen, multiple phases and orientations of the crystals can be presence over the scanned region. The set can thus be highly complex, and make it challenging, if not merely impossible in a realistic amount of time, to depict the common features and relate them to independent sources. A useful tool for such a large multivariate and -dimensional datacube, is to use Blind Source Separation (BSS) algorithms for dimensional reduction. The aim of such an algorithm is to separate out independent sources from a mixed signal, and identify their weighting in the set. The former indicates what are the common features, and the latter indicates where in the set these sources are present.

A special focus is given to the Independent Component Analysis (ICA) algorithm. It assumes that the observed variables can be modelled as a linear combination of hidden variables with some mixing coefficient in the set. For a multidimensional dataset, the observed variables are stored in a $m \times n$ matrix denoted $\mathbf{X}$. ICA reconstructs the set by matrix multiplication of the mixing coefficients, $\mathbf{A}$, and the independent components, $\mathbf{S}$ as presented in eq. (12) [25].

$$\mathbf{X} = \mathbf{A}\mathbf{S} \tag{12}$$

The algorithm thus decomposes the set into a few independent sources and their weighting indicated by their mixing coefficients, which are the eigenvalues of $\mathbf{S}$ and $\mathbf{A}$, respectively. The sources and their weighting are referred to as the components and their loading maps, respectively. The method further assumes that the components are mutually statistically independent, have a non-Gaussian distribution, and that the mixing matrix is a square and invertible [25].

A challenge is to determine the number of independent components in $\mathbf{X}$, and thus the number of rows in $\mathbf{S}$. Such information is a necessary input in the ICA algorithm. An effective method is to preprocess the set by a similar decomposition algorithm called Principal Component Analysis (PCA). It similarly decomposes the set into principal components and their loadings, but also provides the statistical variance of each component. Noise usually decreases exponentially with increasing component index [26]. If one plots the eigenvalues of the component matrix on a logarithmic scale as a function of the component index, one can obtain a so-called *scree plot*. Components dominated by noise should follow a linear curve in a scree plot. The number of components above this line indicates the number of uncorrelated components in $\mathbf{X}$. The component index where the uncorrelated and correlated componets meet are commonly referred to as the *elbow* in the scree plot.

The dataset from a SPED or 4D-STEM experiment can be represented by a two-dimensional matrix where the rows and columns are x- and y-positions of the DPs, which are represented as the observed variables stored in the matrix $\mathbf{X}$. The scanned region can be considered as a linear combination of the individual phases present in the set. The mixed signal can thus be decomposed by the ICA algorithm into independent sources which reveal itself as DPs. However, it is a challenge to determine the physical nature of these components - differentiating between actual sources revealing structural properties and artifacts from the method. It is thus necessary to compare the components and their loading maps to other results with physical meaning. Such a comparison can be done to DPs and VDF-TEM images, which is performed in this thesis.

2.2.3 TEM Sample Preparation by Focused Ion Beam

Sample preparation is a major part of TEM work as the sample needs to be sufficiently thin for the electrons to transmit. As the operating cost of the FIB instrument has gone down, it has become increasingly popular for the TEM sample preparation. Methodologies are established to prepare cross-sectional and plan view lamellae together with nanoneedles. Its great versatility stems from the flexibility of the dual beam system design. It consists primarily of a SEM, a FIB column, which also functions as a Scanning Ion Microscope (SIM), and a sample stage with a goniometric mobility. When the beams are coincidence on the same spot on the sample, and aligned at the eucentric height, it is possible to rotate and tilt the stage without moving away from the workspace. The fundamentals of the instrument is visualized in Figure 9.

The beam sample interaction of electrons was previously covered in section 2.2.1. The interaction is similar for the SEM, but here SE and BSE are used for imaging due to lower accelerating voltages and interest in topological features. The ion-sample interaction is comparatively different where the main reason is the increase in mass. The variation makes it possible to convert sufficient energy to the atoms in the structure to break their binding energy, and for them to leave the structure of the targeted material. The material removal is referred to as sputtering, and can be utilized in a controlled

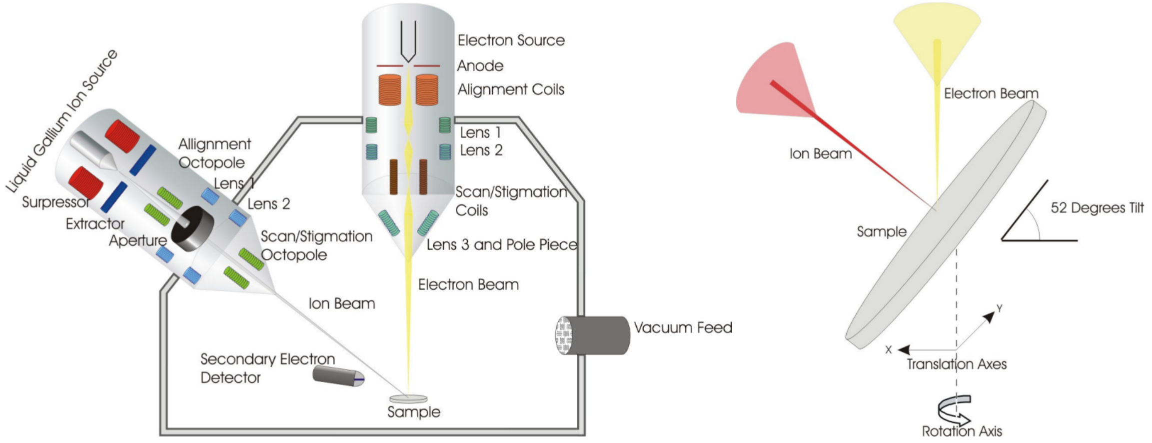

Figure 9: Schematic of the FIB instrument. It is a dualbeam system consisting of a SEM and FIB column together with a goniometric movable stage. Its versatility stems from the interplay between the two columns and the flexibility of the stage. Figure adapted from Yao et al. [27].

manner as ion milling. The rate of sputtering can be controlled by setting the accelerating voltage. The binding energy in the material, and the angle of the ion beam towards the surface, have a great affect on the sputtering rate.

The instrument is equipped with a Gas-Injection System (GIS), which can introduce reactive species into the chamber for deposition to occur. The precursor atoms can relax onto the surface. By letting one of the beams raster over a Region of Interest (ROI), the interaction with the ions or electrons results in deposition of a layer of a desired thickness. Milling, deposition and imaging are the three main functions in the FIB, and the dual beam system lets one supervise the process by forming an image with one and performing fabrication by the other.

An issue that arises in non-conductive samples is that SEs are not transported away from the workspace. Over time, this will build up charge on the surface [28]. The accumulation of charge forms a potential field in the trajectory of both the incoming probe and the outgoing electrons. Electrons thus have to pass through a region of an electric field, and their trajectory can be altered by interaction via the Lorentz force. Consequently, the field may deflect the charged particles and cause disturbance of the image, deflection of the beam and other related charging effects.

2.3 Amorphous Materials

The characteristic features of amorphous materials are presented in this section together with the main theory of the Pair Distribution Function (PDF). A detailed proof of the PDF in general, and specifically for electron diffraction in thin films, can be found in Weber et al. [29] and Cockayne et al. [30], respectively.

2.3.1 Pair Distribution Function

Another class of structural materials is amorphous or glass structures. In many ways, these can be considered as the counterpart of crystal structures as the atoms in an ideal amorphous structure are placed at random intervals and orientations to each other resulting in the absence of any long-range periodicity [31]. Similarly to the ideal crystal, the ideal amorphous structure is rare in nature. Typically, they contain a short range (1-5 nm) order as a consequence of the nature of their chemical bonds [32]. The atoms may also order in the medium range (1-10 nm) between the two. Even though the atoms do not order into lattice sites, they may obtain some correlated disorder within the amorphous structure, such as seen by the correlated disorder of the hydrogen atoms in square ice [33]. They may also cluster in a larger amorphous network of smaller regions such as in nanoglass or -composite [34]. Structural properties in the medium range (1-10 nm) are typically what is desired to study of amorphous materials to better understand their functional properties [31, 32, 35].

The lack of preferred orientation results in diffracted rings, and the lack of long range order results in broadening of the reflections. The characteristic diffraction pattern (DP) for an amorphous structure is thus diffuse rings. The broadening is also a result of thermal vibration of the atoms in the lattice sites. The medium range order of amorphous structures is hard to study quantitatively as the diffuse scattering inhibits the number of diffracted peaks accessible to determine the atomic positions in real space. The crystallographic approach is thus not very effective. The challenge is referred to as the so-called "nanostructure problem", and highlights why these structures are experimentally difficult to study with high precision [36].

As the periodicity of the lattice is absent, our initial description of the solid structure through space group symmetries and lattice spacing becomes insufficient. The structure may alternatively be described by expressing the atom positions through their correlated distances. By picking a central atom and sum over all the interatomic distances, one can obtain a statistically weighted sum, which provides the probability of finding an atom a certain distance away from the central atom. The resulting function is called the PDF, $g(r)$, also called the auto correlation function, and is presented in eq. (13).

$$g(r) = \frac{\rho(r)}{\rho_0} = \frac{1}{4\pi r^2 N \rho_0} \sum_i \sum_{ij} \delta(r - r_{ij}) \tag{13}$$

Here, $\rho(r)$ and ρ_0 are the the local and average atomic distribution, respectively. r_{ij} is the interatomic distance between atom i and j in a system of N atoms. The Dirac delta function, $\delta(r - r_{ij})$, makes a contribution to the sum only when an interatomic distance is present, and the denominator scales the function as the shell surrounding the central atom becomes larger [31, 32, 37].

The PDF is a real space function, and is thus only obtainable from a diffraction experiment through a fourier transform of the intensity distribution. Practically, a reduced form of the PDF, $G(r)$, is obtained such that the function oscillate around zero instead of 1 as r goes to infinity, and it is presented in eq. (14).

$$G(r) = 4\pi r \rho_0 [g(r) - \gamma_0] \tag{14}$$

Here, γ_0 is the PDF shape factor expressing the shape of the nanosized domain. It is a nonlinear component which functions as the baseline of the PDF, and it is commonly set to 1 to approximate the oscillation of the PDF to the material bulk density at long distances [31, 32, 37].

Experimentally, the total scattered intensity includes contributions from elastically, inelastically, and dynamical scattering events. Additionally, thermal and background intensity contributions influence the profile. For a PDF analysis, only scattering events containing structural contributions are of interest, which governs kinematical and elastic scattering events. Artifacts, challenges and solutions to the influence of these contributions will be elaborated further in section 2.3.2.

The PDF can be calculated from a two-dimensional elastic powder DP by first performing an azimuthal integration of the intensity plot. The background then needs to be subtracted from the one-dimensional signal to obtain the structure factor, $F(\Delta k)$ presented in eq. (8b). The independent atom approximation, which sums the scattering contribution from the individual isolated atoms, can be utilized to obtain the $F(\Delta k)$ from the one-dimensinoal scattering profile, $I(\Delta k)$, and is presented in eq. (15) [31, 32, 37].

$$F(\Delta k) = \frac{I(\Delta k) - A(\Delta k)}{B(\Delta k)} = \frac{I(\Delta k) - \sum_\alpha c_\alpha f_\alpha^2(\Delta k)}{|\sum_\alpha c_\alpha f_\alpha(\Delta k)|^2} \tag{15}$$

Here, $A(\Delta k)$ and $B(\Delta k)$ are the atom-weighted total form factor and the total weighted factor, respectively. For electrons, f_α is the atomic form factor presented in eq. (5) of atom α, and c_α is the concentration of the atom in the system. The reduced structure factor is related to the reduced PDF by a sine fourier transform as presented in eq. (16).

$$G(r) = \frac{2}{\pi} \int_0^\infty F(\Delta k) \times \sin(\Delta k \cdot r)\, d\Delta k \tag{16}$$

An example taken from Gorelik et al. [31] is provided for presenting the information obtained in the PDF. Figure 10 compares the PDF of Ih crystalline ice (solid line) with that of liquid water (dotted line), which provide an example of crystalline and amorphous structure, respectively. An illustration of the crystalline structure is included to visualize the interatomic pair distances.

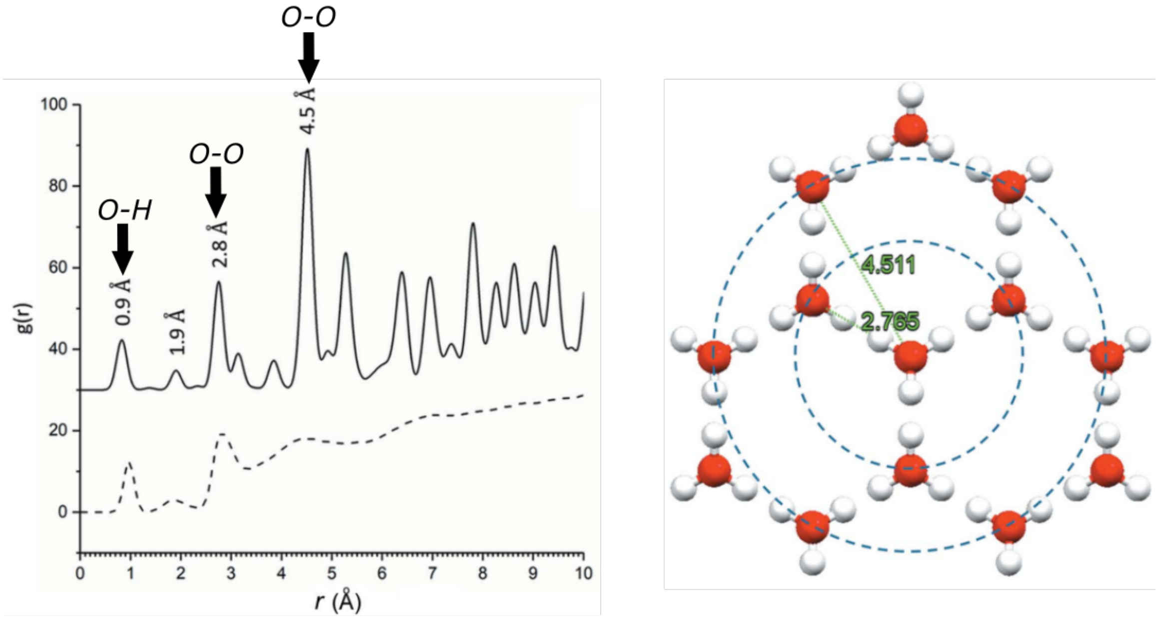

Figure 10: The PDF of Ih crystalline ice (solid line) and liquid water (dashed line) provide an example of crystalline and amorphous PDFs, respectively. Visualization of the atomic distribution of Ih ice is included together with highlighted O-O pair distances. O and H atoms are marked in red and white, respectively. The first O-H and the two first O-O pair distances are marked in the PDF. Figure adapted from Goerelik et al. [31].

The position in the PDF indicates the interatomic distances, and in the crystalline structure, these are clearly defined. From a central O atom, the two first O-O distances are indicated in the PDFs, and in the illustration of the crystalline phase. The height of the peak is determined by the multiplicity of the interatomic distance and the mean scattering power of the two atoms. There are three and six O atoms in the first and second O-O pair distances, which is the reason why the second peak is twice as large. It is only the case as the atom pairs are equivalent. For comparison, the first O-H bond also contains three atoms at this distance, but the intensity is lower due to the weaker scattering intensity of the H atom. The coordination number can thus be obtained from the height of the peak. The width of the peak is determined by the thermal factor of the structure, and the experimental parameters [32].

If the structure is heated up beyond the melting point, the solid structure turns into an amorphous liquid of the same molecules. As a result, the two PDFs function well for a simple comparison of crystalline and amorphous structures. In the latter, there are no distinct peaks beyond the first O-O bond due to great variation in the positioning of the atoms. However, the chemical bonds in the molecules still hold the atoms together, which is why peaks are present in the short-range distance. The PDF can thus be used to determine how large any ordered region extends to.

Each amorphous structure has a unique PDF, and the method can thus be used as a fingerprint for phase identification in order to study the structure as one can identify the main phases present based on the position and height of the peaks. Commonly, the short- to medium range is of interest as the origin of the functional properties are typically located in this range.

2.3.2 Experimental Method for Electron Pair Distribution Function

The calculation of the PDF from the experimental total scattering signal assumes only kinematical and elastic scattering. As electrons interact strongly with matter, it is likely that the outgoing signal will contain dynamical contributions, which reduces the reliability of the intensity distribution of the final PDF, and provides challenges for phase identification based on the coordination number. The challenge could be overcome by increasing the mean free path by increasing the accelerating voltage of the TEM, or by reducing the thickness of the sample in the beam direction such that the mean free path extends the thickness. This is a common feature in most TEM studies, but should be given extra consideration for quantitative PDFs.

PED pattern appears quasi-kinematical as the precession of the beam averages out the dynamical effects rather than omitting them, which means that the kinematical contribution becomes stronger while the dynamical weaker, but the relative intensities between the kinematical peaks are maintained [38]. PED is thus suggested as a novel approach to overcome the dynamical challenges [32]. The effect of precession was investigated by Hoque et al. [38], which systematically tested the effect of precession and temperature of the environment on the PDF of nanocrystal gold particles of 4.2 to 4.5 nm size. They documented a clear reduction in the least-square residual when precession was on.

Additionally, thermal vibrations of the atoms broaden the diffraction peaks as their position fluctuates. Cryo TEM is also necessary for quantitative results for reliable PDFs. Hoque et al. [38] also systematically studied the effect by comparison of results at room temperature and at 90K under liquid N. They documented a clear reduction in the least-square residual between simulated and experimental PDFs for PED at low temperatures [38]. Correa et al. [39] performed a quantitative structural analysis of AuAg nanoparticles using the PDF method from PED. They documented that the PED-PDF combination was an effective method for quantitatively determining the atomic structure and domain size of nanocrystalline structures.

The method requires elastic and coherent scattered electrons to dominate the signal. The inelastic contribution mainly distributes itself as a background signal [31]. An energy filter could thus effectively improve the quality of the PDF by eliminating the inelastic scattered electrons. Mu et al. [40] utilized an energy filter in their PDF study of amorphous and crystalline MgF_2 from electron diffraction.

Gorelik et al. [31] and Souza et al. [32] systematically reviewed quantitative PDF for electron diffraction. An important notation is that the information revealing the short- to medium range order is located at large scattering angels as it is related to the DP by a fourier transform. Both X-Ray Diffraction (XRD) and neutron scattering experiments can provide diffraction data at scattering angels above 30 $Å^{-1}$ [32]. This is a limitation in the TEM, and the camera length should thus be as low as possible to push to higher scattering angles to improve the resolution in the PDF.

An azimuthal integration of the total scattering is necessary to obtain the experimental PDF. Any parameter which alters the circular symmetry may thus alter the PDF. An issue in TEMs is optical aberration from the magnetic lenses. Astigmatism, which results from uneven focal points perpendicular to the optical axis, will stretch the image asymmetrically, and produce an elliptical signal. Astigmatism is thus necessary to minimize either pre- or post-experiment. Additionally, the centering of the DPs is essential to obtain as high-resolution in the PDF as possible.

The ordering at the nanoscale requires a nanobeam such that the electrons only interact at the ROI. A methodology is thus to combine NBD with a scanning probe to obtain a 4D-STEM dataset where local variations can be studied. Mu et al. [26] combined 4D-STEM experiment together with unsupervised machine learning to identify nanoscale regions of different amorphous phases and composition. Potentially most impressively, they were able to identify shear bands and study their variations from the bulk in a multilayer amorphous CuZr/Cu structure. The final PDF can to a good approximation be considered as a linear combination of the individual amorphous phases. BSS algorithm can thus be an effective tool to separate out independent phases and their weighting in the set. ICA is applicable to decompose a PDF dataset as the components need to oscillate around zero, and the components need to be statistically independent [26].

2.3.3 Structural Properties of Amorphous SiO_2 and TiO_2

An amorphous region in a multipurpose SPED dataset from a CPU sample was used as proof of principle for combining SPED, PDF and BSS algorithms. The author was informed that this region had two distinct layers of different amorphous SiO_2 *phases, and the data analysis was performed accordingly. Two days prior to the thesis deadline, it turned out that this was the wrong chemical composition. The layers are experimentally verified to consist of* Si_3N_4*, and not* SiO_2*. The results and analysis were thus performed as if the amorphous region is* SiO_2 *and not* Si_3N_4*. Due to the limited time, the results section is left untouched, but the method will be discussed in the light of the new information.*

Polyamorphous structures are compositions of atoms which can exist in different amorphous phases, and thus contain different functional and structural properties. This is similar to crystalline polymorphous structures such as the introduced TiO_2 in section 2.1.2.

Figure 11 contains the phase diagram of SiO_2 [41]. The solid line noted T_{cr} marks the temperature limit for crystal growth. The phases are thus crystalline above, and amorphous below. Low-pressure phases (up until coesite in Figure 11) are variations of ordered chains of tetrahedrons, while high-pressure phases, such as stishovite, are ordered chains of octahedrons [41]. The polyamorphous structures below T_{cr} are mainly differentiated into two phases - a disordered chains of tetrahedrons (cristobalite- and coesite-like structures) or octahedrons (stishovite-like sturctures). SiO_2 phases with tetrahedral coordinates (SiO_4) contain a Si-O bond length which varies between 1.55-1.61 Å [42]. Conversely, in the high-pressure phases with octahedral coordinates (SiO_6), the Si-O bond length is 1.77 Å [42]. The difference in amorphous phases can thus be distinguished based on the shift in the first Si-O pair distance.

Similarly, the polymorphous TiO_2 phases vary in their ordering of octahedral units (TiO_6) and how these share side, edges or corners. Below the temperature of crystal growth, one can similarly have disordered chains of octahedrons which in the short- to medium-range resembles a stacking similar to the different phases [43].

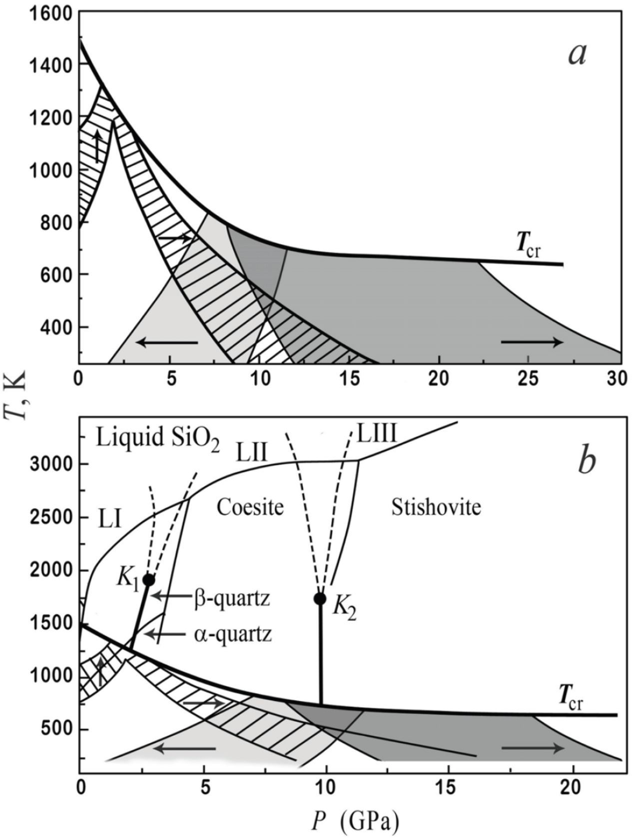

Figure 11: The phase diagram of SiO$_2$ is presented. The solid line noted T_{cr} marks the temperature needed for crystal growth. (a) is a zoomed image of the phase diagram below T_{cr}, while (b) is with the crystalline phases. See section for further description. Figure adapted from Polyakova et al. [41]

2.4 Pulsed Laser Deposition

The material properties are highly dependent on the synthesis method. The relevant theory for growth by PLD is presented in this section. The principle of conventional and combinatorial PLD to produce a CCS film together with kinetic energy driven thin film growth are included.

2.4.1 Conventional and Combinatorial PLD

The scope of this section is based on Ch. 1 section 6 in Mihailescu et al. [44] textbook titled ”Pulsed Laser Ablation: Advanced and Applications in Nanoparticles and Nanostructuring Thin Films”. The citations throughout the section are thus omitted.

Conventional PLD is a mature physical vapour deposition method, which is utilized both for new materials search and engineering, but also for commercial production [45]. The film growth and deposition are performed inside a vacuum chamber, and utilize a high-intensity pulsed laser beam to transfer energy to a target material. Material at the target evaporate from ablation, and forms a strongly forwarded directed plasma plume which can transfer material from the target to a substrate surface where it may deposit. A process gas is commonly introduced into the chamber as a reactive species, and to alter the kinetic energy of the atoms as the species in the plume will collide with the atoms of the process gas. The atoms will also collide with each other within the plume during their paths from the target to the substrate. Each plume transfers a small amount of material, and by repeating the process, one can build up a thin film layer-by-layer. The principles are illustrated in Figure 12.

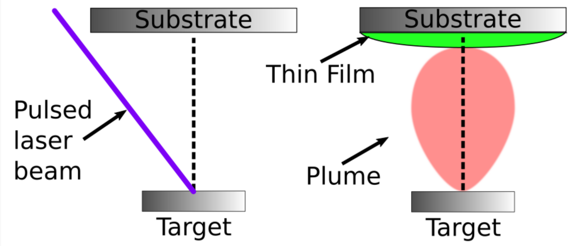

Figure 12: Schematic of the basics of conventional PLD. A pulsed laser beam is utilized to evaporate material from a target surface (left). The evaporated material forms a strongly forwarded directed plasma plume, and can transfer the material to a substrate surface where it may deposit (right). Illustration provided by Hogne Lysne.

The growth in PLD is a far-from-equilibrium process, meaning that the atoms that deposit to the substrate surface do not necessarily have sufficient energy and time to arrange themselves in a structure minimizing their Gibbs and surface free energy. The process is rather driven by the kinetic energy available for the atoms that deposit to diffuse and find nucleation sites in the time available before the rest of the plume deposits, and the atoms from the following plume. The deposition rate for each plume is instantaneous, which can quench the growth before any diffusion can occur. Additionally, the energy landscape of the surface may prohibit or facilitate for certain growth processes by introducing energy barriers.

The different experimental parameters can thus be chosen to alter the kinetic energy of the adatoms and the energy landscape. A few important parameters are the frequency, fluence and shape of the laser beam as they determine the deposition rate and the energy transferred to the evaporated atoms, the morphology and composition of the target surface as they determine the species population in the plume, the process gas determines the kinetic energy of the plume and the reactive species at the surface, geometry or dynamical movement of the substrate holder during deposition determine the distribution of the material, and the substrate type and surface topography determine the initial energy landscape. The large number of parameters makes PLD excellent for material search. Combinatorial setups give further advanced possibilities.

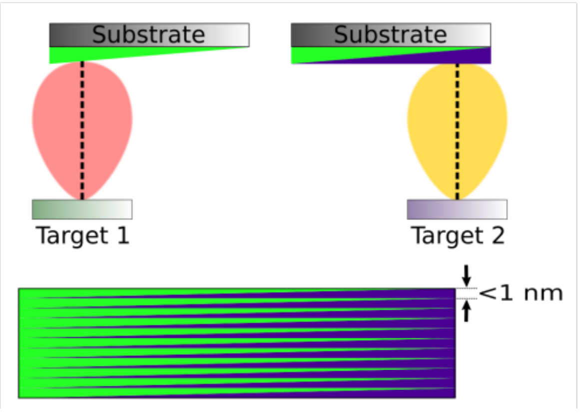

Figure 13: Schematic of the basics of conventional PLD for producing a CCS film. The non-uniformity of the plume can be utilized by depositing material from different target iterative at separate locations to produce a CCS. Illustration provided by Hogne Lysne.

There are a variety of possible ways in which one can setup deposition by c-PLD. In the Solar Cell Physics group at NTNU, the non-uniformity of the distribution of mass within the plume is utilized to produce a CCS film. The non-uniformity is a consequence of the plume being strongly forwarded directed, and thus reshapes as it propagates [46]. As a result, most mass is deposited at the plume center and less on the flanks. Additionally to the mass gradient, there is also a kinetic energy gradient away from the plume center as the atoms at the flanks of the deposited plume have to travel a further distance to reach the substrate. Consequently, they will be exposed to more collision events, which will reduce their kinetic energies.

The CCS film is grown by utilizing multiple targets of different materials. By letting their plumes deposit at different locations and carefully choosing the distance between them and the number of plumes deposited, one can minimize thickness variations and simultaneously produce a CCS between the two plume centers. A simplified schematic is presented in Figure 13, which aims to illustrate the main procedure for CCS growth. Similarly to PLD, one builds the structure layer-by-layer by depositing ablated material in an iterative process. The difference is that the chemical composition varies repeatedly through the layers as the material comes from different targets. The chemical composition will vary continuously laterally, and this makes it possible to study numerous doping concentrations and their influence on the growth and material properties in a single film.

2.4.2 Kinetic Energy Driven Film Growth

The following section is based on Ch.1 of Mihailescu et al. [44] textbook ”Pulsed Laser Ablation: Advances and Applications in Nanoparticles and Nanostructuring Thin Films”. The citation throughout this section is thus omitted.

Growth by PLD is a far from thermodynamic equilibrium process due to the instantaneous deposition rate of the plume. The atoms do not contain sufficient time to order into a structure which minimize their Gibbs and surface free energy. Growth is rather driven by the kinetic energy available to activate different diffusion mechanisms within the time frame between plumes. Nucleation and structural development thus digress from common equilibrium growth modes such as layer-by-layer (Fran-van der Merve), 3D islands (Volmer-Weber) and layer-plus-island (Stranski-Krastanov) found in other deposition methods [47]. These processes minimize the surface free energy between a supersaturated nuclei in relation to the substrate and interface energy, while atomistic processes are dominant in PLD. Growth modes and the resulting structural properties are thus quit different. The kinetic energy of the atoms in relation to the energy landscape and deposition rate is driving growth. The principal experimental variables are the substrate temperature, the deposition flux, the process gas and the kinetic energy of the deposited species. Their importance will be seen in the different stages of structural development.

Atomistic processes in the early stages: The atoms in the plume are deposited on the substrate directly. Atoms which only form loose bonds with the substrate through van der Waals forces, may contain sufficient energy to diffuse on the surface. These are referred to as *adatoms.* Stronger bonds, such as ionic or covalent, increase the energy barrier for such diffusion. Crystalline and amorphous substrates would provide an anisotropic and isotropic surface tension, respectively. The former may thus force the atoms into lattice sites as it is energy demanding to diffuse over them. The choice of substrate can be effective if one wants to grow epitaxial films. However, surface mobility is generally higher on crystalline surfaces than amorphous, between lattice sites.

Once the adatoms start to diffuse, they commonly have four faiths. Firstly, they can re-evaporate back into the gas. Secondly, if they do not contain sufficient energy to diffuse, they may deposit directly where they land. Further, if they contain sufficient energy, they may diffuse to find other adatoms to form a nuclei, or they may find an existing one. Nuclei consisting of two adatoms are referred to as a *dimmer*, and that of larger numbers, an *island.* Dimmers and islands may also contain sufficient

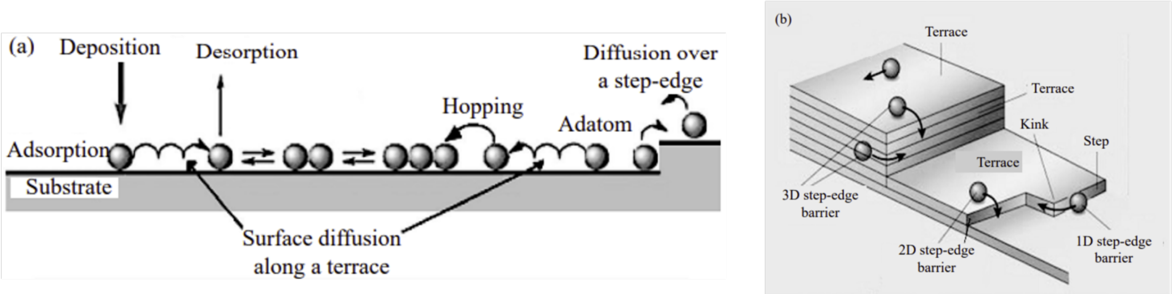

Figure 14: Schematic image of atomistic processes in PLD. (a) One-dimensional side-view and (b) three-dimensional view of atomistic processes. Image adapted from Mihailescu et al. [44].

energy to diffuse, or if they are unstable, resolve into separate adatoms. Larger islands commonly resolve less than smaller ones. The phenomenon is referred to as *Ostwald ripening* [48, 49]. Such an island would form a one-atomic layer, or terrace, for the other adatoms. With sufficient energy, the adatoms may hop on top of a layer where diffusion and growth of 3D islands can continue. However, this is energy demanding and edges of such a layer may cumulate adatoms and drive lateral growth of the islands. Steps, kinks, and holes, or anything which provides an energy barrier, may thus function as nucleation centers. The mentioned atomistic processes are visualised in Figure 14. The number of adatoms is important for the likelihood of these processes, which illustrate the importance of the deposition flux. The process gas inside the chamber is also important as it increases the number of adatoms on the surface, and alters the kinetic energy of the adatoms to diffuse. Additionally, the substrate temperature provides thermal energy to the adatoms. It is thus an important variable for surface diffusion length. All these variables are importance within the residence time before the subsequent plumes arrive.

Atomistic processes in the later stages: Structural development and thickness growth follow after nucleation and lateral growth in the early stages. Atomistic processes also drive growth here. Four different processes are commonly identified in relation to the kinetic energy of the adatoms. They are linked to the substrate temperature, T_S. Kaiser [47, p.3055] summarize them as follow:

- ”*Shadowing: A geometric interaction between the arriving admolecules and the roughness of the growing surface. This effect is dominant at low substrate temperatures T_S. It occurs because the vapor beam is directed.*
- *Surface diffusion: Mobility of admolecules at surfaces and interfaces such as grain boundaries; dominant at medium substrate temperatures T_S.*
- *Bulk diffusion: Mobility of admolecules in the volume of grains; dominant at high T_S.*

- *Recrystallization: Phase transition as a complete change of crystal orientation; dominant percolation thickness, large film thickness, and high T_S.*" (Kaiser, 2002).

Further, one commonly classifies thickness growth into three structure zones (I, II and III) based on when these atomistic processes are dominant [47]. The classification is primarily based on findings from film deposition methods with a continuous flux of atoms. There is a discontinuity in the flux provided in PLD as the atoms come in separate pulses. However, the kinetic energy driven processes are expected to be similar. The zones are separated based on the activation energy for different diffusion mechanisms. It is linked to the normalised temperature, T_r, which is the ratio between the melting temperature of the deposit material, T_m, and substrate temperature, T_s, such that $T_r = T_m/T_s$. Kaiser [47, p.3055] summarizes them as follows:

- *"Zone I: $T_S/T_M < 0.3$ (low mobility; admolecules stick where they land; the results is a fine-grained porous real structure).*
- *Zone II: $0.3 < T_S/T_M < 0.5$ (surface diffusion occurs with activation energies of 0.1-0.3* eV*; a columnar real structure is obtained).*
- *Zone III: $T_S/T_M > 0.5$ (bulk diffusion occurs with activation energies above 0.3* eV*, resulting in a rough equiaxed grained real structure).*" (Kaiser, 2002).

An overview of the trends in the zone model is presented in Figure 15 (a). The influence of partial pressure is also included in the overview. The characteristic features of zone I are an amorphous structure, or nanocrystalline columns extending to 10-20 nm with defected regions and voids. As the atoms more or less deposit where they land, the likelihood of adatoms finding each other is low. Nucleation is thus a rare event. However, local surface or roughness variations may result in nucleation of an initial nanoparticle. A competitive growth then occurs between the amorphous and nanocrystalline regions as more material is deposited. An inverse crystalline cone develops as lateral growth becomes a function of film thickness due to variation in surface diffusion between the amorphous and crystalline regions [50, 51]. The cone is visualised in zone I in Figure 15 (b) A transition zone, zone T, is also commonly identified between zones I and II where the voids between the crystalline columns disappear as seen in Figure 15 (b).

Surface diffusion becomes dominant in zone II. Here, the surface diffusion distance exceeds the lattice constant, and the adatoms may find each other to form islands initially. As thickness increases, column growth is the common characteristic with higher crystallinity (fewer defects) than the columns in the previous zones as seen in Figure 15 (b). The preferred orientation of these columns is determined by the growth rate, rather than the thermodynamical most stable structure. Here, van der Drift has

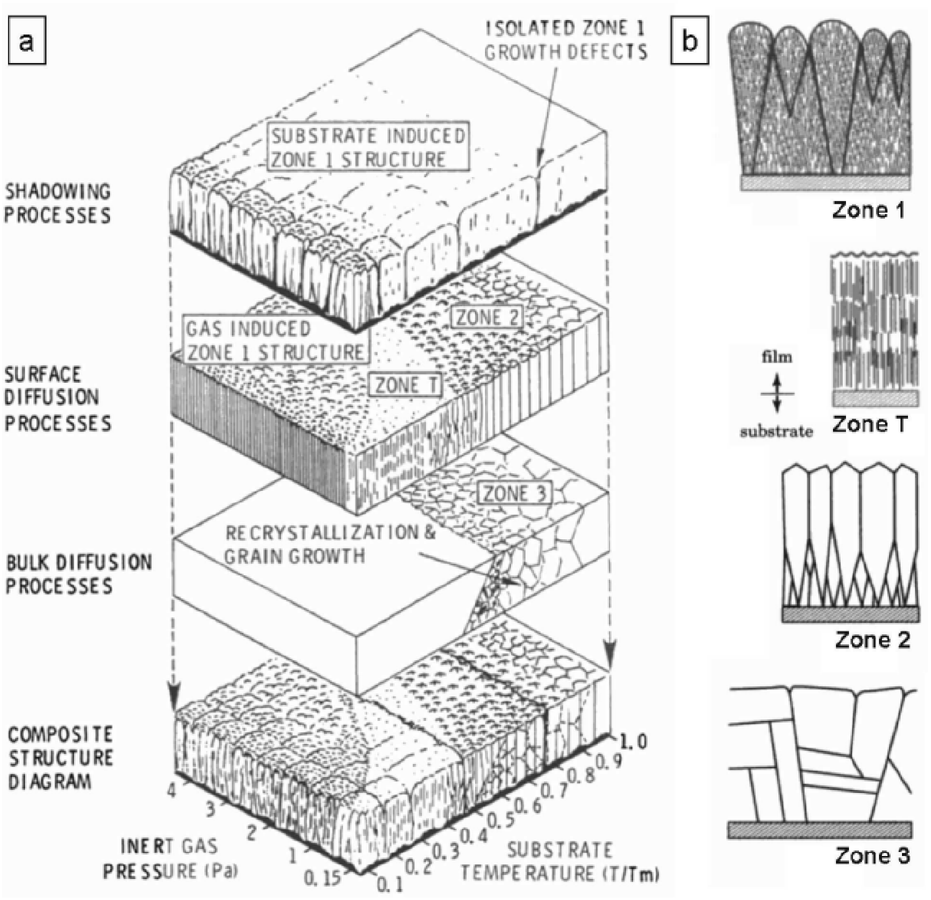

Figure 15: Overview figure of the structure development (a) for the dominance of different atomistic processes together with a superposition of them. (b) Schematic of the characterisitic features for the different zones in the structure model. See section 2.4.2 for further description. Image adapted from Lackner et al. [52].

listed three general outcomes driven by kinetic energy which has been observed [53]. The outcomes are paraphrased here [53, pp.268-270]:

1. An initial preferred orientation of the very nuclei. Epitaxial growth on a mono- or polycrystalline substrate may develop due to lattice matching with the structure. Additionally, the preference for a certain set of planes parallel to an amorphous substrate may develop. This is commonly observed to be the densest one. Conversely, a rough surface may develop a preferred orientation from increased horizontal growth and decreased vertical.
2. Starting from random nuclei, a preferred orientation develops as a result of evolutionary selection based on lateral and vertical growth rate.
3. Re-crystallization of the columns into a more thermodynamic stable structure with a preferred

orientation.

Common for 1 and 2, is that the relative lateral and vertical growth rate chooses the preferred orientation. The growth rate is determined by the reactivity of the surfaces, which is related to the density of the atoms, and the nature of their bonds. Adatoms can diffuse further on stable and low-energy facets compared to unstable ones with high surface energies. Adatoms are more likely to stick to reactive surfaces, and diffuse on stable ones [48], which is the reason why high-energy facets orientated vertically are commonly preferred after evolutionary selection from random nuclei. As the thickness increase, these columns can shadow over its neighbours and overrule them. Similarly, an initial preferred orientation may result from fast lateral growth with higher energy facets orientated laterally and lower vertically such that larger crystalline terrace can form, which growth of crystalline columns can advance from.

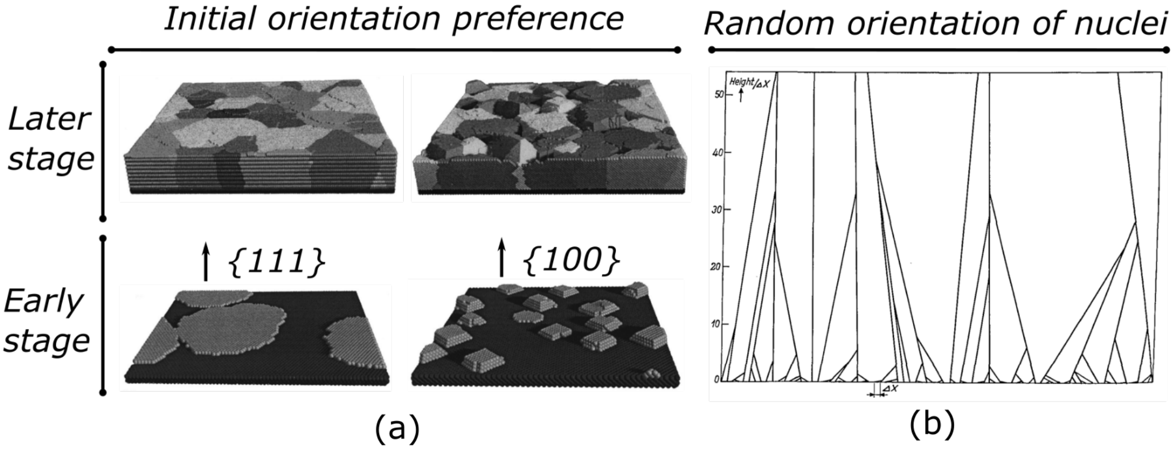

Figure 16: Illustration of structure development in thin film growth in (a) the early and later stages with different preferred initial orientation, and (b) evolutionary selection from random nuclei. See section 2.4.2 for further description. Figure (a) and (b) are adapted from Huang et al. [54] and van der Drift [53], respectively.

Figure 16 presents an overview of the development of different orientation preferences. Huang et al. [54] performed an atomistic simulation of thin film growth of Al by simulating growth of different planes normal to the substrate, and their results function as an example for film growth. With the same amount of atoms deposited, the development of the early stages is quite different between the low energy {111} and high-energy {100} planes as seen in Figure 16 (a). The former has one-atomic terraces with large surface areas while the latter has many smaller three-dimensional islands. The development in the later stages is presented as well. The simulation governs that the initial planes orientated normally to the substrate are fixed. If the initial orientation is random, an evolutionary selection occurs where the fastest vertical growth rate survives, which is seen by the development from random nuclei in Figure 16 (b).

The zone III activates bulk diffusion, and recrystallization of the structure to a more thermodynamic favorable structure. The common feature is equiaxed grains as seen in Figure 15 (b). The zone is not further introduced as the growth is far from the melting temperature of TiO_2. The zones are not as distinct as they may appear, and the T_r may vary depending on the experimental parameters. Different structure zone models are developed for other parameters which alter the kinetic energy in the deposition. As an example, structure zone models according to Thorton and Barna include the effect of the process gas and impurity content, respectively, in addition to T_S [47]. The dominant processes may also vary as the thickness increases. The structural development may thus transition between zones within a single film. Additionally, when growing with c-PLD such as the Solar Cell Physics group, the growth conditions vary between each layer in the cycle as the experimental parameters are changed. This may complicate these atomistic processes further.

Surface Energy of Different TiO_2 Facets: Due to the importance of the surface energy in zone II, the stability of different TiO_2 facets of rutile and anatase is presented. The relative surface area in relation to the bulk, becomes more dominant as the particle size decrease. Even though rutile contains a lower Gibbs free energy, and is more stable for bulk structures, anatase has a lower surface free energy and can thus be preferable for nanocrystalline grains [17, 55]. The far-from-equilibrium growth in PLD enables the growth of structures with large areas of high-energy facets within the film. An example is how Fan et al. observed kinetically controlled fabrication of anatase with the high-energy {001} facet orientated parallel to the substrate [56].

Table 1: Surface free energy of different low-index facets of anatase and rutile. They are organized with decreasing kinetic energy from left to right. Values taken from Jiang et al. [57] and Liu et al. [58] for rutile and anatase, respectively.

Rutile						
Facets {hkl}	{001}	{111}	{011}	{101}	{100}	{110}
E_{Surf} (J/m^2)	1.51	1.51	1.11	1.11	0.76	0.74

Anatase						
Facets {hkl}	{110}	{001}	{010}	{101}	-	-
E_{Surf} (J/m^2)	1.09	0.90	0.53	0.44	-	-

The anisotropy of the tetragonal unit cell results in great variation in the surface free energy of the facets in the two structures. The surface free energy of the low-index facets of rutile and anatase is presented in Table 1. For the rutile structure, the {001} and {111} facet have the highest surface free energy and is thus the most unstable and reactive surface. The {011} and {101} are also highly reactive seen by their high surface free energies. Such facets will grow fast for the rutile structure in zone model II conditions for growth. {100} and {110} are noticeably more stable with their lower surface free energy.

The energies of the anatase structure are on average lower than that of rutile. However, the {110} and {001} facets have higher surface free energies than the lowest, but noticeably less than the high-energy facets, of the rutile structure. The {010} and {101} facets have the lowest surface free energy among the two polymorphs, which illustrate why anatase can be preferential for nanocrystalline structures. The facets are low-index ones, and those of higher index typically result in dense planes of atoms. They are thus commonly of high energy and are highly reactive. As an example, the surface energy of the {103} anatase facet is 0.83 J/m^2 which is comparative to its high energy {001} [58]. It is unknown how the introduction of the Cr and N may alter the stability and reactivity of the facets.

3 CCS Film Growth and Experimental Details

3.1 CCS Film Growth by PLD

The c-PLD growth of the CCS film was performed by Hogne Lysne and Thomas Brakstad as a part of their PhD work. The reader is guided to their work for a detailed documentation of the mathematical modelling of the plume thickness and the CCS film deposition which has lead to the CCS film studied in this thesis [59]. A Neocera PLD system with a base pressure of 10^{-9} to 10^{-10} torr and Coherent ComPexpro 110 KRF excimer laser was used for growth of the CCS film. The CCS film was grown on a 2" Si (100) wafer kept at 550 °C during growth. Prior to the deposition, the substrate was cleaned with acetone and isopronal. This does not remove any oxidation layer on the surface. A PI-KEM TiO_2 and a Standford Advanced Materials CrN target were utilized with 99.9 % and 99.5 % purity, respectively. The following routine was used.

1. **Deposition of TiO_2 at 1st plume center:** The initial step deposits material from the TiO_2 target, and was performed under a $1.3*10^{-2}$ torr O_2 gas flow. 26 pulses of ablated material were deposited with the plume center 1.3 cm away from the wafer center. This represents -1.3 cm in Figure 17. A laser repetition and fluence of 5 Hz and 1.5 J/cm^2, respectively, were used for the deposition.

2. **Deposition of TiO_2 at 2nd plume center:** The stage was then rotated 180 degrees around the wafer center such that the following plumes were deposited 1.3 cm away from the wafer center in the other direction. This regards +1.3 cm in Figure 17. 22 pulses of ablate material from the TiO_2 target was depisited with the equivalent nominals for laser fluence and repretition rate in the $1.3*10^{-2}$ torr O_2 gas flow.

3. **Deposition of CrN:** The gas flow was then changed to $1.6*10^{-2}$ torr N_2. 90 pulses of ablated material from the CrN target was deposited at this location. A laser repetition and fluence of 10 Hz and 1.5 J/cm^2, respectively, were used for the deposition.

4. **Deposition of TiO_2 for capping:** The material target was then switched back to the TiO_2 target to deposit a layer of TiO_2 in the N atmosphere to "cap" the Cr and N atoms to avoid oxidation. Earlier studies found formation of CrO_2 when grown in O process gas. 10 pulses with laser repetition of 5 Hz was then deposited from the target before the process gas was changed back to $1.3*10^{-2}$ torr with O_2 flow. 12 pulses of material from the TiO_2 target was deposited with a laser repetition and fluence of 10 Hz and 1.5 J/cm^2, respectively, to complete the capping of the doping layer.

The simulated thickness variations is shown in Figure 17 (a), together with a cross-sectional view of

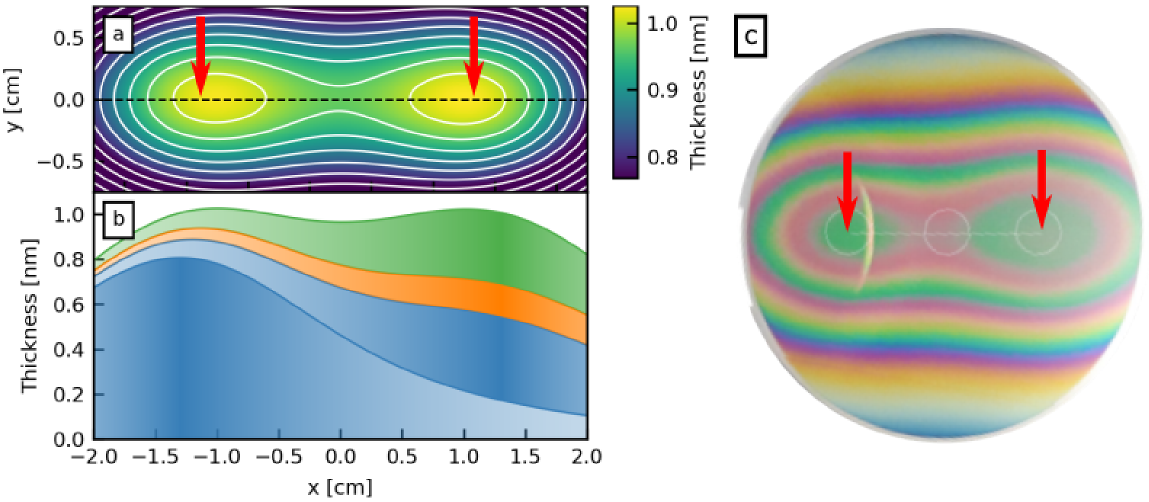

Figure 17: (a) Plan view of simulated film thickness across the CCS film. (b) Cross-sectional view of one routine where blue represent TiO_2 grown under O_2 process gas, orange deposition from the CrN target, and green TiO_2 grown under N_2 process gas. The gradient in the colours indicate kinetic energy reduction away from the plume centers. (c) Plan view photograph of the CCS film studied in this thesis. Red arrows indicate the center positions where the two plumes are deposited. The locations are referred to as plume centers. The figure (a) and (b) is provided by Hogne Lysne.

the deposition from one repetition of the routine in (b). A plan view photograph of the CCS film is included in Figure 17 (c), where the red arrows indicate the location of the plume centers to relate the images. The doping concentration is expected to vary between 2.2 and 9.4% between -1.75 cm to 1.75 cm in Figure 17 based on the simulation. As seen in Figure 17, the deposition from one c-PLD routine deposits material which is ∼1 nm in thickness. The process was repeated for 600 loops for the CCS film studied in this thesis to build up a film of ∼600 nm thickness.

3.2 Properties of TiO_2 Grown by PLD

The variation of the different deposition parameters in PLD as introduced in section 2.4 can all alter the growth conditions. Therefore, the final structure of the CCS film is sensitive to what deposition parameters are used. A literature study will be presented here for growth of TiO_2 by PLD. The study includes work done on similar films by other groups, and characterization done within the Solar Cell Physics group on the CCS and other films studied in this thesis.

Growth of TiO_2: The phase diagram of TiO_2 is presented in Figure 18. The anatase-to-rutile phase transition occurs at ~600 °C, which is close to the substrate temperature at 550 °C kept during deposition. The phase diagram governs bulk material at thermodynamic equilibrium. As particles approaches the nanoscale, minimization of the surface free energy becomes dominant. Anatase holds a lower surface free energy than rutile, and can thus be preferential on the nanoscale [17]. Khatim et al. [60] studied the different in phase stability of amorphous, anatase and rutile bulk for nanoparticles. They observed that phase transformation from amorphous to anatase and from anatase-to-rutile were shifted to higher temperatures for 5 nm sized particles.

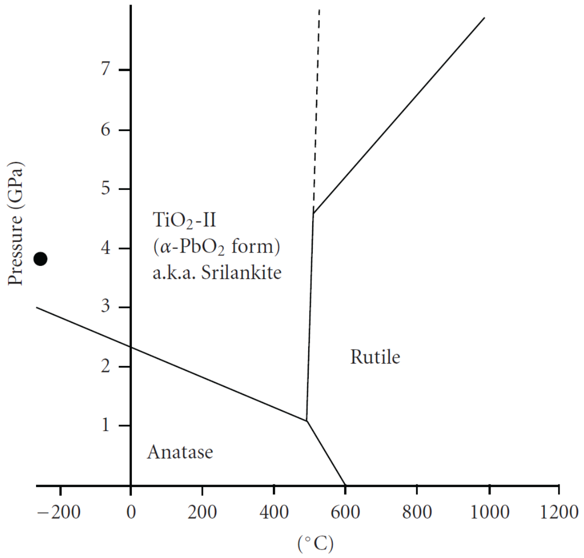

Figure 18: Phase diagram of TiO_2 polymorphs. The anatase-to-rutile phase transition occurs at ~600 °C. Figure adapted from Nie et al. [61].

The effect of substrate temperature was investigated by Balakrisnan et al. [62] where they studied the microstructure by XRD on samples grown on Si (100) and quartz substrates at temperatures between 300-873 °C. They utilized a 2.25×10^{-2} torr O partial pressure for the process gas together with a laser with repetition rate of 10 Hz. They reported the presence of both anatase and rutile on all samples, but a dominant rutile phase at higher temperatures.

Additionally, Gyorgy et al. [63] reported crystalline anatase growth on SiO_2 (100) substrate in the temperature range 300-500 °C. They used a process gas of 7.50×10^{-2} torr O pressure and laser fluence of 2 J/cm^2 with a repetition rate of 2 Hz. At 400 °C and 500 °C, they observed a preference for {004} and {112} planes parallel to the substrate, respectively. The film was of poor crystallinity in the temperature range 100-300 °C.

The influence of process gas pressure on the growth mechanisms on a Si (100) substrate was studied by Gyorgy et al. [64]. The substrate was kept at 500 °C and a laser fluence of 3 J/m^2 with a repetition rate of 3 Hz. At low pressure, 75×10^{-6} torr, the rutile phase was dominant while a transition to the anatase occurred as the process gas oxygen pressure was increased to 7.5×10^{-2} torr. They concluded that this was due to the decrease of the kinetic energy of the ablated species as the mean free path decreased, and effectively slowing the species in the plume down. This was also supported by Long et al. [65], Sanz et al. [66] and Walczak et al. [67] which concluded that both anatase and rutile could be obtained on a Si (100) substrate by tuning the substrate temperature and ambient pressure.

The species type of the adatoms that are deposited also influence the growth mechanism in PLD. Ions are more susceptible to Columbic forces from the substrate surface than neutral species. This is expected to alter the surface diffusion, and thus the growth modes. Chu et al. [46] studied the kinetic energy and species distribution of a laser ablated plume of Ti in PLD. They varied the fluence between 3 and 8 J/cm^2, and the pressure of the process gas between 10^{-6} and 20 torr, observed that ionic Ti atoms occupied the front of the expanding plume while neutral Ti atoms were present in the center and back parts. The ionic atoms were faster moving than the neutral, and thus contained a higher kinetic energy. Additionally, the kinetic energy decreased gradually away from the plume center, and the decline was more dramatic with lower laser fluence and at higher pressure of the process gas. The lower laser fluence provided less initial momentum of the atoms while the higher pressure increased the number of collisions during flight.

Wijnands et al. [68] combined numerical modeling of the plasma plume together with experimental observation using TiO_2 as an example. They observed a negligible variation in Ti:TiO and Ti:TiO_2 ratios across a deposition area of 5 cm for high pressure (0.75×10^{-2} torr), but significant variations at lower (1.5×10^{-2} torr). Additionally, at low pressures the fast O atoms were observed to arrive at the substrate surface before slower Ti atoms. This could be expected to influence the oxidation state at the surface. For a Si (100) substrate, this could lead to the formation of a thin amorphous layer of SiO_2 [69]. However, the substrate used for the CCS film studied in this thesis is expected to contain such a layer as it has not been polished prior to deposition.

The CCS film studied in this thesis is in part built up of alternating layers of TiO_2 grown in O and N atmosphere. Zhao et al. [70] investigated the influence of the atmospheric pressure by studying N-doped TiO_2 grown by PLD on a glass substrate from a rutile target in both a O and N process gas.

They utilized a 20 Hz repetition rate, a laser fluence of 60 J/cm^2, and a pressure of 7.5×10^{-2} torr for deposition on a quartz substrate kept at 600 °C. Both films contained the anatase structure, but the film grown in O process gas had a preferred orientation (004) while that in N process gas had random growth orientation. Under O process gas, the topography showed columnar morphology of roughly 100 nm thickness, while that of N showed inhomogenous distribution of the columns ranging from 70 to 200 nm.

Albu et al. [71] reported similar column growth in both O and N pressure when growing TiO_2 by PLD, and an increase in crystalite size together with a greater size variation under N process gas. They utilized a Si (100) substrate at 450 °C, a laser fluence of 2.8 J/cm^2, a repetition rate of 40 Hz and a process gas pressure of 75×10^{-3} torr.

Socol et al. [72] similarly investigated the influence of atmospheric pressure by growing TiO_2 under O, methane, N and a mixture of O and N atmosphere. They utilized a glass substrate kept at 450 °C, a laser fluence of 9 J/cm^2 and a repetition rate of 2 Hz at a constant pressure of 0.15 torr. Their XRD results indicated a polycrystalline anatase structure with a preferred orientation (004) under a pure O and O-N mixture process gas whereas a pure N resulted in a random orientation. They considered the generation of O vacancies within the structure as a potential cause for the lower crystallinity of TiO_2 grown in N atmosphere.

Growth of Cr and N doped TiO_2: It is unknown if the rutile or anatase structure will be favorable when one is incorporating Cr and N. Structurally, an important factor affecting what is the preferred phase, is the amount of defects on the oxygen sublattice. The oxygen vacancies reduce the structural rigidity and facilitate for the favoring of the rutile phase [17]. Dopants that alter the oxygen vacancies may thus promote or inhibit a favoring of the rutile structure. Cathionic substitution of Ti with a specie of lower valency (less than four), will increase the number of oxygen vacancies, or potentially push the Ti into an interstitial site, as a result of balancing the charges, which is the case for Cr [17]. Similarly, if the N^{-3} substitutes O^{-2} then two N atoms can be balanced by the removal of three O, and thus leave one site vacant. The increased number of oxygen vacancies is expected to facilitate for the rutile structure.

The doping layer will alter the energy landscape for the following atoms, and thus strongly influence the surface diffusion and growth mechanisms. Similar studies of TiO_2 doped with other dopants thus also provide valuable insight. Ali et al. [73] investigated the consequence of O_2 partial pressure and Nd doping on the phase transformation of TiO_2 grown by PLD. They observed how the introduction of Nd resulted in reconstructed surfaces in order to minimize the surface energy of an initial anatase nanoparticle. The change resulted in a transition to rutile nanoparticle first, then to an amorphous structure as the Nd concentration was increased and partial pressure decreased. Additionally, they reported a drastic decrease in the size of the particles.

The incorporation of Cr into PLD grown films has been proposed to function as nucleation sites [74]. The referred study looked at Cr levels of 2 to 5% into ZnS thin films, and they documented a decrease in grain size as they went to higher levels. As the Cr atoms are higher in mass, they may have a shorter surface diffusion length, and can thus function as a point barrier for the other adatoms.

The characteristics of the CrN plume are also expected to differ both in terms of the kinetic energy, and the species distribution. The N atoms are lighter than O, and the Cr are heavier than Ti. The N atom is thus expected to move faster than O, and Cr slower than Ti, which may result in a greater volume of the plume. The difference in mass was investigated by Bauer et al. [75] in a comparative study of Al and Ti plume dynamics. They documented a slightly higher expansion rate of the Al plume than the Ti due to its lower mass.

Supporting Characterization within the Research Group: Within the Solar Cell Physics group, a variety of different material characterization techniques have been performed on the CCS film. Macroscopic techniques such as Raman Spectroscopy and X-Ray Diffraction provide statistical support to the findings of the TEM study of the structural properties. Former masterstudent Herman Solstrand [76] performed Raman Spectroscopy at three different locations on the CCS film, and a similar film without the incorporation of the doping layer. In the film without the dopants, an equivalent time of wait was included instead of deposition from the CrN target. The approximate location of his characterization is indicated in Figure 19, and the results are included in Figure 20.

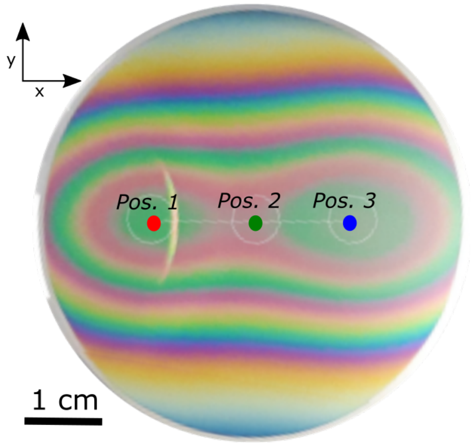

Figure 19: Plan view photography of the whole 2" wafer with the the CCS film. The colored circles indicate approximate location of the characterization by Raman Spectroscopy performed by Herman Solstrand [76].

The lower panels of Figure 20 show the results for the CCS film without incorporation of the dopants. One of the deposition parameters are thus the increasing thickness of the capping layer of TiO_2 grown under N process gas. The thickness of the capping layer is thinnest at the first plume center (position 1), thicker at the wafer center (position 2), and thickest at the second plume center (position 3). The experimental details of the deposition of the capping layer was introduced in section 3.1. Solstrand observed crystalline anatase at the first plume center (position 1) which transitions to an amorphous structure with a mixture of crystalline anatase and rutile at the wafer center (position 2) and the second plume center (position 3).

The higher panels of Figure 20 show the results for the CCS film with incorporation of the dopants. Here, Solstrand observed crystalline structure at the first plume center (position 1) with a strong signal from the rutile structure. The structural properties was amorphous at the wafer (position 2) and second plume center (position 3) [76]. Raman spectroscopy gains statically average from a circular region of roughly one μm. The material properties may thus vary within a single scan. Additionally, the crystalline regions could be dominated by diffuse spread from the amorphous regions. Solstrand hypotheses that the structure might be nanocrystalline at the second plume center [76].

Masterstudent Marcus Grand Michaelsen [77] studied the CCS film with the incorporation of the dopants by XRD. He observed a similar transition from crystalline rutile to an amorphous structure across the CCS film. At the first plume center similar to position 1, the rutile appears to be polycrystalline with a preferential growth of {200} and {110} planes parallel to the substrate.

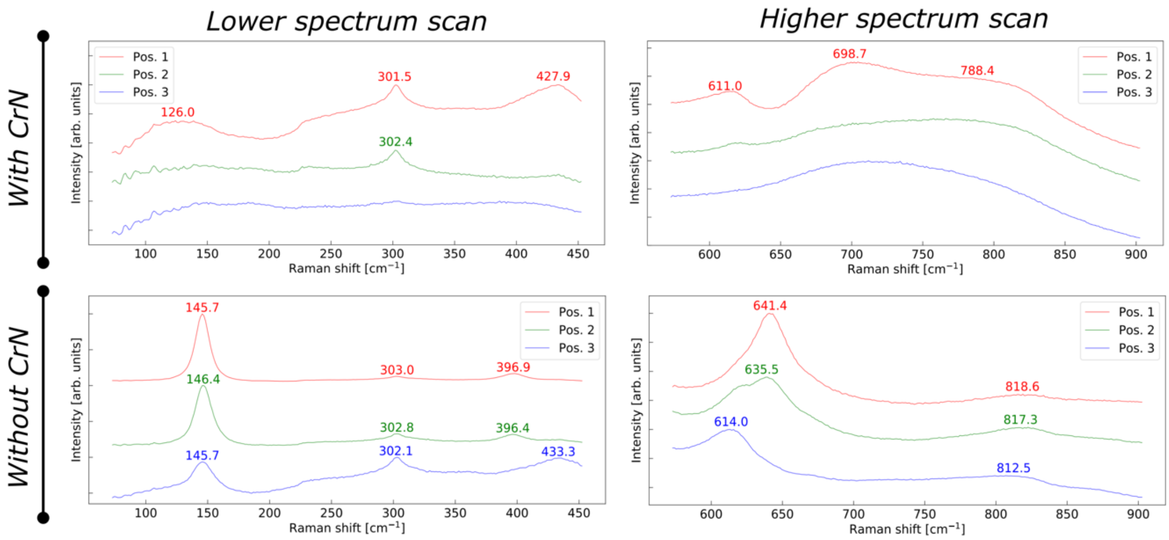

Figure 20: Raman spectroscopy results performed by former master student Herman Solstrand [76] at the three locations marked in the CCS film. Upper panels show the results with incorporation of the dopants, while the lower panel shows without incorporation of the dopants. See section 3.2 for a further description. Results adapted from Solstrand [76].

3.3 TEM Sample Preparation by FIB

Conventional cross-sectional FIB lamellae were prepared on the FEI Helios NanoLab DualBeam FIB G2 and G4 at NORFAB Nanolab. The latter is equipped with an EasyLift software and Omniprobe for in-situ transportation between the film and the TEM-grid. A road map of the locations where the lamellae were extracted from is presented in Figure 21. The figure is a plan view photograph of the CCS film, where the colored circles indicate the approximate areas were the lamellae have been extracted.

The horizontal series is parallel to a wafer center line, and holds an increasing doping concentration from left to right together with a decreasing kinetic energy away from the plume centers. Additionally, the amount of TiO_2 grown under N background pressure increases across the series. It is referred to as the series parallel to the wafer center line. The vertical series from the second plume center is extracted to isolate the deposition parameter to study the effect of decreasing kinetic energy. It will be referred to as the series perpendicular to the wafer center line. A characteristic profile of each lamella is presented in Table 2.

The preparation of the first plume center lamella is chosen as a representation for the overall procedure. Charging effects were present initially when working on the sample through beam deflection during single scans, distortion of the image and other related effects. A conductive layer was sputtered on the sample surface as a measure to overcome this. The Sputter coater for SEM sample preparation at NORFAB Nanolab was used to produce a thin layer of Au particles on the surface which reduced the charging. It consisted of a 20 nm thick layer of 30 nm wide Au islands. The layer is visualised in the indented image of Figure 21.

The following preparation was performed on the FEI Helios NanoLab DualBeam FIB G2.

1. **Protection layer by e- and ion beam deposition:** To protect the top features of the sample from ion beam irradiation, a thin layer of Pt was deposited by the electron beam prior to any use of the FIB. Commonly, the damage layer of a 30 kV ion beam source is 30 nm. The thickness thus needs to extend according to the accelerating voltage of the beam. The e-beam was operated at 3 kV with a beam current of 0.34 nm to deposit the layer. The dimensions of the layer were (x,y,z) = (15 μm, 5 μm, 0.2 μm). An ion-beam deposited layer with the same dimensions and location was then performed with accelerating voltage of 30 kV and 0.28 nA current. These are visualised in step (1) and (2) in Figure 22, respectively.

2. **Milling of trenches:** Trenches were then milled by the ion beam to extract the bulk material surrounding the area of interest. This was done in a two-step process. First, one mill away the bulk volume with a regular or cleaning cross section setting. The former raster over a horizontal

Table 2: Each lamella is given a name and color for identification for the presentation of the results. The nominal and measured position is presented, where the latter are obtained at the FIB G4.

Id	Location (x,y)		Experimental variables	
Color	Nominal (cm)	Measured (cm)	Dopant concentration	Kinetic energy
Blue	(-1.75, 0)	(-1.69, 0.05)	Lowest	Intermediate
Red	(-1.25, 0)	(-1.26, 0.03)	Lower	High
Yellow	(-0.75, 0)	(-0.73, 0.06)	Low	Intermediate
Cyan	(0, 0)	(0.07, 0.07)	Intermediate	Low
Pink	(0.75, 0)	(0.67, 0.09)	High	Intermediate
Purple	(1.25, 0)	(1.24, 0.02)	Higher	High
Green	(1.75, 0)	(1.80, 0.04)	Highest	Intermediate
Orange	(1.25, 0)	(1.24, 0.27)	Higher	High to intermediate
White	(1.25, 0)	(1.24, 0.54)	Higher	Intermediate

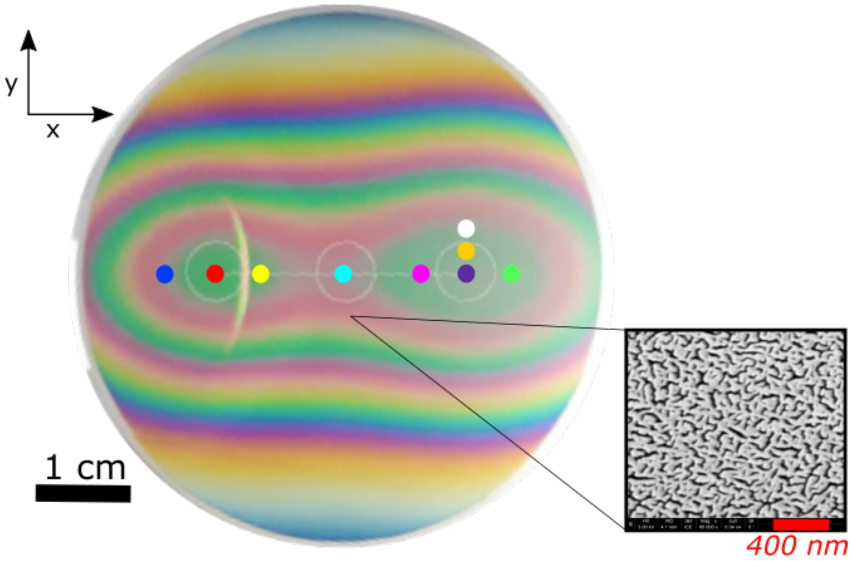

Figure 21: Plan view image of the CCS film with road map for the two series. Conventional cross-section FIB lamellae were extracted parallel and perpendicular to the wafer center line. The colored circles indicate the approximate locations where the lamellae have been extracted from. See Table 2 and the corresponding section for specifications. The indented image is a SEM image of the surface obtained at the FIB G2. It illustrate the gold islands forming the conducting layer to reduce charging effects.

surface area to mill layer by layer. The latter mill to the desired depth for one line, then proceed to the next one. The former is more time efficient than the other, but as this step is done to remove the bulk material, which one chooses is not expected to alter the quality of the final lamella, but rather a question of time efficiency. The trenches on either side were of dimensions (x,y,z)= (25 μm, 15 μm, 6 μm). A note here is that the depth of milling is material dependent, and thus the exact dimension is unknown. However, for a thin film study, one only desires a depth which exceeds the thin film. 6 μm is well sufficient for this. The bulk was milled away with 30 kV accelerating voltage and 9.3 nA current for the FIB. The second step performs a cleaning cross section at the closest area to the membrane. The scanning pattern removes a vertical layer towards the membrane. One can then easily stop as the beam reaches the protection layer by viewing the milling with the SEM. The dimension of this cut is dependent on how close the first step is performed to the protection layer. X and z dimensions are equivalent to step one, but y varies between 1-2 μm. The FIB was set to 30 kV and 2.8 nA. This step is visualized as (3) in Figure 22.

3. **Milling of J-Cut:** One then performs a final step before lift-out where one performs a J-cut. This step involves parallel milling of three regular rectangular cross sections. This is done by the ion beam milling at 0° tilt angle, which means that the ion beam is milling at a 52° angle. The dimensions here are arbitrary but a width of 1.5 μm of each pattern and sufficient depth for the milling to go through the membrane is necessary. One mills through one side and below, but leaves a small bridge at the other side to hold it in place until it is extracted. This step is visualized as (3) in Figure 22.

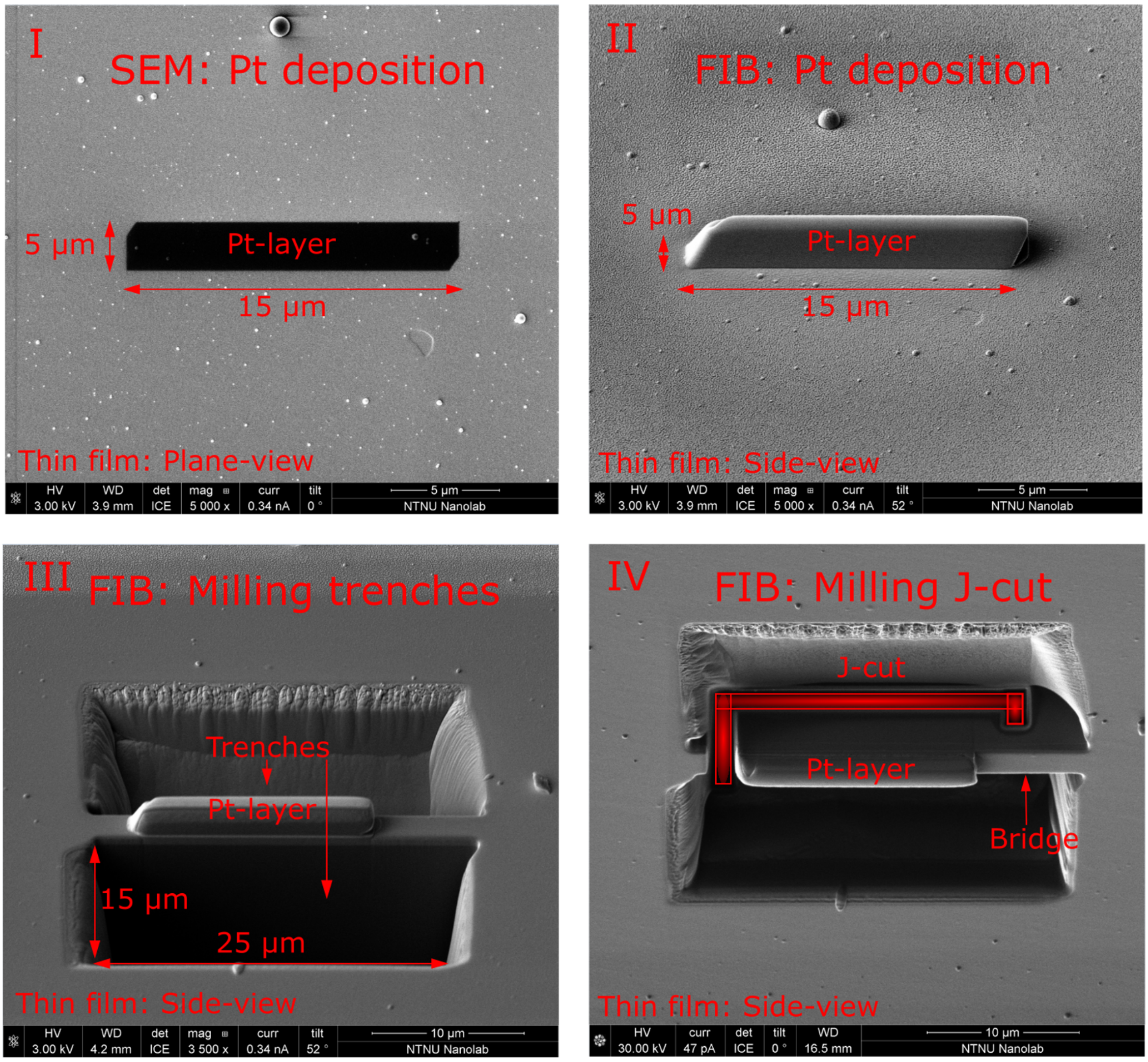

Figure 22: SEM and SIM images obtained at the FIB G2. Deposition of protection layer by the SEM (I) and FIB column (II) correspond to the first step at the FIB G2. The second step consisted of milling away bulk trenches (III). The third step consisted of milling a J-cut. See the detailed description of each step in section 3.3.

The following steps were performed on the FEI Helios NanoLab DualBeam FIB G4 where the aim was to thin the membrane down to a thickness profile of less than 150 nm in order to make transmission of the high electron beam possible, but also as the damaged layers from the ion beam is necessary to remove from the performed J-cut. The exact thickness has not been quantitatively measured on the different lamella.

1. **Establishing Connection to the Omniprobe:** The lift-out needle is inserted and driven to the membrane. Here, one utilizes the dual beam geometry to navigate in the x-y plane with the

SEM, and the z-direction with the SIM at 0° stage tilt. When there is a connection between the tip of the needle and the membrane, one deposits a Pt layer between the two. Once this is done, one mill away the bridge, and extract the membrane from the sample as seen in step (5) from Figure 23. The needle is then extracted, and inserted again after one has navigated to a TEM grid holder. The TEM grid contains multiple fingers. Here one navigates to the side-edge of one of them using the dual beam system in a similar manner as seen in step (6) of Figure 23. There are different methods for how one can place the membrane on the grid. Here, a flag post was chosen.

2. **Establishing the Connection to the TEM-Grid:** Once the side of the membrane touches the grid finger, one establishes a connection between the two. First, an area overlapping the membrane and the grid was milled away. The grid is made up of Cu-atoms, and their bonding provides a strong connection as the material redeposits rapidly. Due to the risk of transportation damage as the final lamella would be moved between different instruments, a thin Pt layer was deposited on both sides. This was done after the needle was removed, as one would need to rotate the stage for such a deposition.

3. **Removing the Needle:** Once the connection is established, one proceeds by milling away the connection between the membrane and the needle. This is done with the ion beam. An image visualizing the step is provided in step (7) of Figure 23. The needle is then extracted, and the membrane should stay in place if the prior step is done properly.

4. **Thinning the Bulk:** The first step includes the removal of the majority of the material. This is done at 1-2° of the perpendicular axis between the FIB and the top of the membrane. One performs a cleaning cross section in order to remove a vertical surface layer-by-layer towards the center of the sample. In a similar fashion to the cleaning of the trenches, one can view the milling with the SEM during operation such that one can stop at the desired thickness. This is done on both sides for accelerating voltage of 30 kV and 0.44 nA.

5. **Thinning the Damaged layer:** The bulk thinning may create a damaged layer on the lamella, and thus a second thinning process was performed with the same operating voltage and current.

6. **Polishing of the Side Edges**: The final process is done to polish the lamella by going to low accelerating voltages for the ion beam. The damaged layer is minuscule here, and it is safe to perform a rectangular regular cross section milling on the side surface. This was done first for 2 minutes at 8 kV and 0.26 nA current at angles +-3°, before the process was repeated for 1 minute on each side for 2 kV and 0.26 nA. A final top-view image of the lamella is presented in step (8) of Figure 23.

The description above gives the experimentally aimed sample preparation method. Images of the final lamella taken at the S(T)EM instrument at NORFAB Nanolab are included in Figure 24.

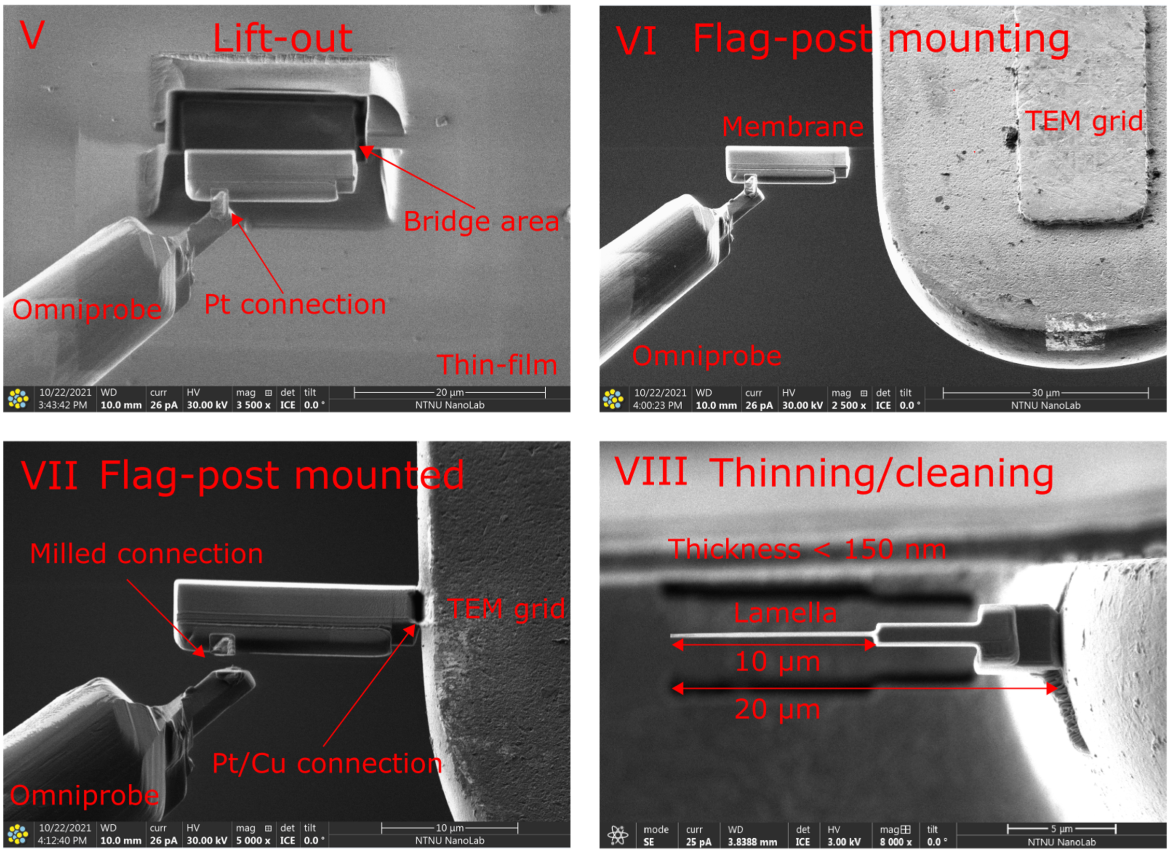

Figure 23: SEM and SIM images obtained at the FIB G4. Images show liftout (V), transportation to the TEM-grid (VI), flag-post mounting (VII), and finished thinned and polished lamella (VIII). See the detailed description of each step in section 3.3.

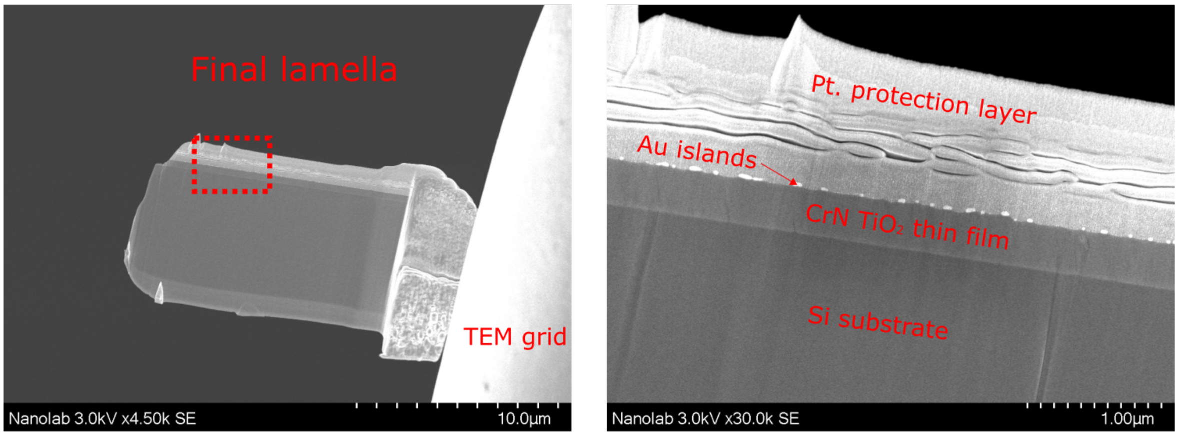

Figure 24: Sideview image of the final lamella with highlighted ROI (left), with zoomed image of this region shows the substrate, thin film, Au islands and protection layer (right).

3.4 Characterization by TEM

The lamella series was studied at the NORTEM lab facilities at NTNU. The conventional TEM techniques such as SAED, BF/DFTEM imaging and High-Resolution TEM (HRTEM) were performed at the JEOL JEM-2100 microscope. The SPED dataset was obtained at the JEOL JEM-2100F.

Conventional Techniques Across the Lamella Series: The JEOL - JEM 2100 TEM instrument is equipped with a LaB_6 filament source, a Gatan 2k Orius CCD camera and Gatan GMS 1.8, 32 bit software for image processing. A double tilt holder with a tilt range of +-30° was used for the experiment. Liquid nitrogen was used to cool down the vacuum chamber to reduce contamination. The operating voltage was 200 kV for all experiments. The optical column was aligned, and the stage was tilted to align the [110] zone axis of the Si (100) substrate parallel to the electron probe prior to the data acquiring. BFTEM and CDFTEM were obtained together with SAED at each lamella in the two series. The approximate size and location of the apertures are visualised in the figures in chapter 4. A DP of the interface and the substrate was obtained at the same location for supporting data and calibration. All TEM images were obtained at 100k magnification, and all DPs were obtained at a 80 *cm* camera length. HRTEM was obtained at 1M magnification. Figure 25 visualizes the different regions of the lamella together with the relative aperture size.

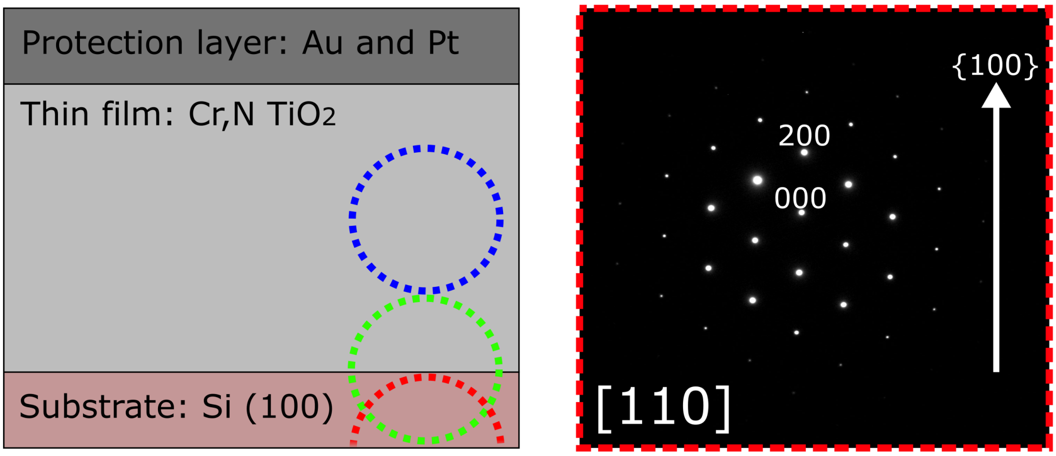

Figure 25: Schematic visualization of the lamella regions together with the relative aperture on the thin film (blue), interface (lime) and substrate (red). The [110] zone axis of the substrate was used as navigation for the setup.

Image Processing and Analysis of Conventional TEM Data: The conventional TEM analysis was performed in the following procedure. The DP of the substrate was uploaded to the Digital Micrograph GMS software [78]. The pixel-to-length scale was calibrated by measuring the distance,

R_{hkl}, to a known lattice spacing, d_{hkl}. This is equal to a constant due to the small angle approximation of the distance from the image to the image plane from the detector. This is named camera constant, CL, and presented in eq. (17). The DP of the substrate was used for this purpose.

$$d_{hkl} * R_{hkl} = CL \tag{17}$$

The DP from the film was then uploaded. The (000) reflection was identified, and the d-spacing for the distinct reflections were measured together with the distance between them. The zone axis can be identified by taking the dot-product of the potential Miller indices in the indexed pattern. The direction is perpendicular to the lattice planes, and is the normal of the plane of the vectors spanning to two different reflections. The zone axis, [UVW], is thus the dot product of the vectors to two chosen reflections, R_1 and R_2, which is presented in eq. (18).

$$[UVW] = \vec{R_1} \times \vec{R_2} \tag{18}$$

The Spot ID v1 tool in the Recipro software was utilized to find potential candidates based on the Space group and experimental d-spacings [79]. Kinematical DP with a unique solution across the different polymorphs was identified as the present structure. The images and figures were processed using ImageJ and Inkscape to tilt the images, adjust the brightness, add scale bars, and organize super figures to best visualize the results [80, 81].

SPED Experiment from the Wafer and Plume Centers: The SPED experiment was performed on the JEOL JEM-2100F instrument at NORTEM facilities. It is equipped with a Quantum Detectors Merlin direct electron detector, and Nanomegas scan generator. The experiment was performed at ROI at the wafer center together with the second plume center. The ROI was identified from the conventional TEM analysis. The system was aligned on the [110] zone axis of the substrate. The accelerating voltage of the electrons was 200 kV. The probe was prepared for NBD with a spot size 1 nm, alpha mode 5, and camera length 8.0 cm. Rocking angle and frequency were 1° and 100 Hz, respectively, for the precessing beam. A nominal spot size of 0.5 nm was utilized at the wafer center. The dimensions of the scan are listed below:

- Wafer Center: 896x384 pixels scanned over a 719 x 308 nm region. The exposure time for the DP was 10 ms.
- Second Plume Center: 256x512 pixels scanned over a 472 x 945 nm region. The exposure time for the DP was 20 ms.

Before indexation of the DPs and performing VBF-TEM and VDF-TEM imaging, the dataset was preprocessed using the Python-based libraries Hyperspy [82] and Pyxem [83]. This governed centering the direct beam, normalizing the intensities, and calibrating the pixel-to-length scale.

Details of SPED Practice set and PDF analysis: *An amorphous region in a multipurpose SPED dataset from a CPU sample was used as proof of principle for combining SPED, PDF and BSS algorithms. The author was informed that this region had two distinct layers of different amorphous* SiO_2 *phases, and the data analysis was performed accordingly. Two days prior to the thesis deadline, it turned out that this was the wrong chemical composition. The layers are experimentally verified to consist of* Si_3N_4*, and not* SiO_2*. The results and analysis were thus performed as if the amorphous region is* SiO_2 *and not* Si_3N_4*. Due to the limited time, the results section is left untouched, but the method will be discussed in the light of the new information.*

The multipurpose CPU practice dataset was obtained from a SPED experiment. The accelerating voltage of the electrons was 200 kV. The probe was prepared for NBD with a nominal spot size 1 nm, alpha mode 5, and camera length 22.95 cm. Rocking angle and frequency were 1° and 100 Hz, respectively, for the precessing beam. A subset of a ROI containing layered amorphous SiO_2 was preprocessed for PDF analysis. This considered centering the direct beam, normalizing the intensity, and performing an azimuthal integration with a masked center beam. The background was subtracted by the independent atom approximation introduced in section 2.3.1 in eq. 15. To optimize the fit between low- and high scattering angles, the background was set to fit between $s_{min} = 0.9$ Å^{-1} and $s_{max} = 2.9$ Å^{-1}. The signal was then damped by a stepwise Lorch function to prepare the beam stop for a fourier transform. Low scattering angles were damped by an error function to limit artifacts from the background subtraction in the masked region. This according to the Pair Distribution Function Analysis tutorial in the pyxem library [84]. A sine fourier transform was then performed to obtain the PDF. The dataset was then de-whitened by the Singular-Value Decomposition (SVD) algorithm of the Scikit Python-based library [85]. Its scree plot indicates three principle components, which were utilized as input in the ICA algorithm. The FastICA algorithm in the Scikit library was utilized for the decomposition [85]. The code for the performed analysis of the CPU practice set is included in the Appendix A.

4 Results and Discussion

The results from the TEM study are obtained for the continous compositional spread (CCS) film along the two series. The TEM results provide insight of the structural properties from the cross-sectional view. An overview of the position of the lamellae in the two series, and their properties, was introduced in Table 2 in section 3.3. The alignment procedure of the lamellae for the TEM characterization was presented in Figure 25 in section 3.4, and will be common for all images and diffraction patterns (DP)s. The substrate will thus be seen in the bottom, the CCS film in the middle, and the protection layers in the top of the images.

The results of the TEM study are divided into three parts. First, an overview of the microscopic properties across the CCS film is presented with comparative bright-field TEM (BFTEM) images and DPs - both for the series parallel and perpendicular to the wafer center line. The second section provides further results of the structural properties, focusing on phase identification, and orientation relation between the CCS film structure and the substrate. In addition to conventional TEM techniques used in the first part, dark-field TEM (DFTEM) and high-resolution TEM (HRTEM) images together with scanning precession electron diffraction (SPED) results will be presented in the second part. See figures in section 2.2.2 for a presentation of the techniques. The influence of the doping concentration and the deposition parameters on the growth modes will be discussed. The last section governs structural characterization of amorphous and nanocrystalline regions by the pair distribution function (PDF) of the SPED datasets.

4.1 Structural Trends Parallel and Perpendicular to the Wafer Center Line

The results from the two series, provide insight into the structural trends across the CCS film. There are seven and three lamellae included in the series parallel and perpendicular to the wafer center line, respectively. See Table 2 for details of the lamellae positions and properties. The first plume center is at position -1.25 cm, while the second is at 1.25 cm away from the wafer center in position 0.0 cm. The doping concentration and the thickness of the capping layer increase from position -1.75 cm to 1.75 cm, while the kinetic energy of the adatoms decreases radially away from the plume centers in position ± 1.25 cm. The kinetic energy parameter is thus at the lowest at the wafer center in position 0.0 cm. According to the deposition parameters presented in section 3.1, the doping concentration and thickness of the capping layer is expected to be relatively constant perpendicularly to the second plume center. The series perpendicular to the wafer center line thus functions as a method to isolate the variable of the composition and the capping layer to look at the influence of the position in relation to the plume center. The results from the perpendicular series thus supplement the results along the wafer center line to evaluate the influence of the doping concentration and the deposition parameters.

BFTEM Images and DPs Parallel to the Wafer Center Line

A BFTEM image and a DP were obtained for each cross-sectional lamella parallel to the wafer center line. The results are combined together in a comparative overview in Figure 26 to illustrate the trends across the series. In Figure 26 (a), a plan view photography of the central part of the wafer of the CCS film is included to illustrate where the lamellae are taken out according to the poistions in Table 2. The BFTEM images are included in Figure 26 (b-h), while the DPs are included in Figure 26 (i-o). The TEM results are color coded to the location where the lamellae have been taken out as marked in Figure 26.

The TEM results at the first plume in position -1.75 cm, -1.25 cm, and -0.75 cm show similar structural properties seen from the intensity variations in the BFTEM images in Figure 26 (b-d), and the distinct reflections in the DPs in Figure 26 (i-k). The distinct reflections indicate constructive interference from the scattering of periodic planes of atoms within the CCS film. The structure is thus crystalline at the first plume. Indexation of the DPs at the first plume shows a presence of predominantly rutile phase with its {100} or {110} planes parallel to the substrate. Detailed indexation is provided in section 4.2 and 4.3.

The TEM results at the wafer center in position 0.0 cm in Figure 26 is unique in its structural properties compared to the other lamellae in the series. The DP in Figure 26 (e) shows a mixture between distinct reflections and diffuse scattering, where the the diffuse scattering indicates the absence of any long-range order. The BFTEM image Figure 26 (l) shows two distinct regions with different intensity variations. The lamella was studied in greater detail, and the results are presented in section 4.4. The growth of inverse crystalline cones are present within an otherwise amorphous CCS film at the wafer center.

The TEM results between the wafer and second plume center in position 0.75 cm, are also unique across the lamellae in the series. The BFTEM image in Figure 26 (f) shows no intensity variations within the CCS film, and the corresponding DP in Figure 26 (m) shows fully diffuse scattered rings, which indicate a lack of long range order.

The TEM results at the second plume in position 1.25 cm and 1.75 cm in Figure 26 show similar structural properties by low intensity variations in the BFTEM images in Figure 26 (g) and (h), and a mixture of distinct reflections and diffuse scattered signal in the DPs in Figure 26 (n) and (o). Further analysis of the two positions show that nanocrystalline columns are present in an otherwise amorphous structure. See section 4.6 for the results.

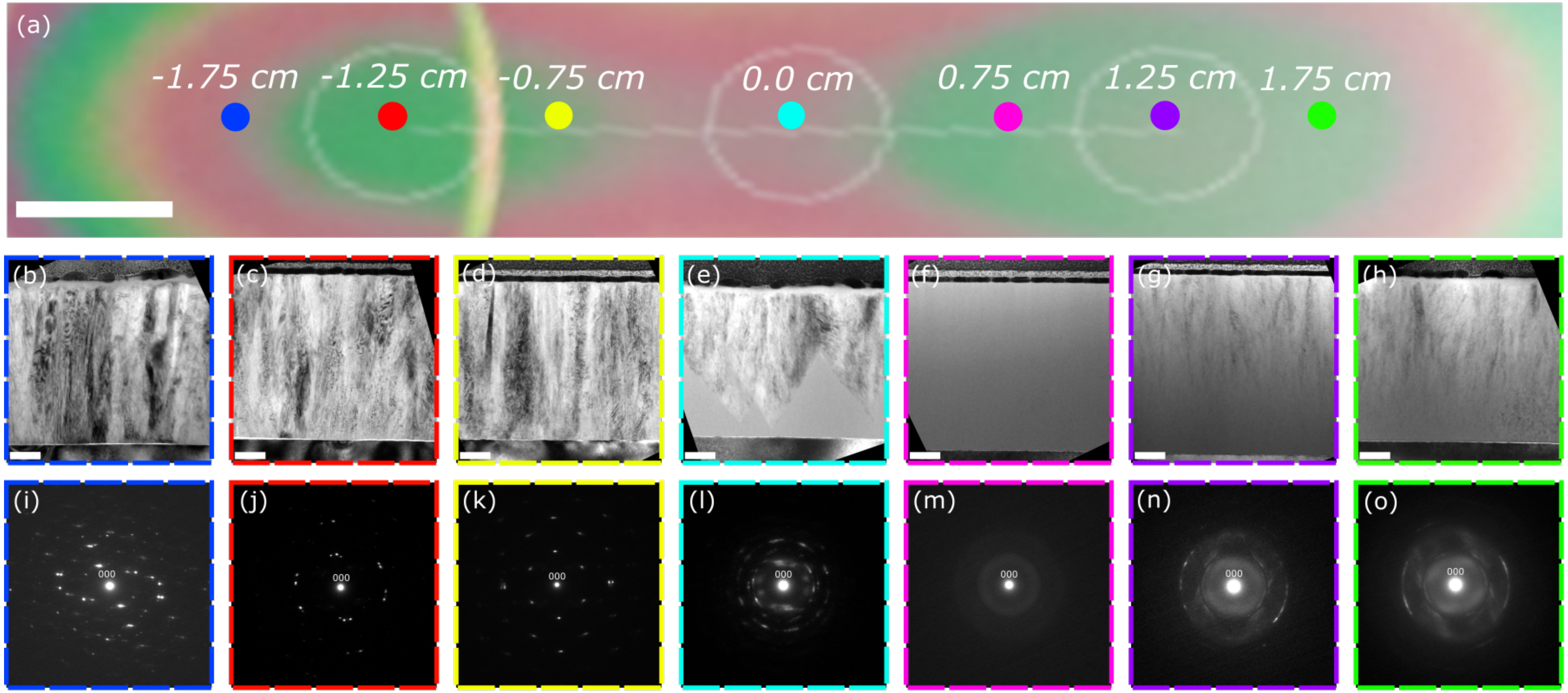

Figure 26: (a) Plan view photography of the CCS film with colored circles at the approximate location of the lamellae in the series parallel to the wafer center line. (b-h) BFTEM images of the cross-sectional lamellae showing the substrate at the bottom. (i-o) DPs from the cross-sectional area of the CCS film. Scale bar of the plan view photography and cross-sectional BFTEM image is 0.5 cm and 100 nm, respectively.

BFTEM and DFTEM Images and DPs Perpendicular to the Wafer Center Line

A BFTEM image and a DP were obtained for each cross-sectional lamella in the series perpendicular to the wafer center line. The results are combined together in a comparative overview in Figure 27 to illustrate the trends across the series. In Figure 27 (a), a plan view photography of the central part of the wafer with the CCS film is included to illustrate where the lamellae are taken out according to the positions in Table 2. The BFTEM image are included in Figure 27 (b-d), while the DPs are included in Figure 27 (e-g). Additionally, DFTEM images from the objective aperture marked by a dashed circle in the DPs are included in Figure 27 (h-j). The TEM results are color coded to the location where the lamellae have been taken out as marked in Figure 27.

The TEM results (in Figure 27 (b), (e) and (h)) from the lamella at position 0.50 cm perpendicular to the wafer line, is furthest away from the plume center in this series. The BFTEM image in Figure 27 (b) shows no intensity variations in the CCS film region. The corresponding DP from the CCS film in Figure 27 (e) shows only diffuse scattered signal, which indicate a lack of preferred orientation and long-range order in the structure. A DFTEM image was obtained from an arbitrary part of the DP for consistency, and the image is presented in Figure 27 (h). The location of the objective aperture is illustrated in Figure 27 (e). The image supports the conclusion that the structure is amorphous, but one or two crystalline grains might be present. These are seen in the top left part of the DFTEM image in Figure 27 (h).

The TEM results (in Figure 27 (c), (f) and (i)) from the lamella at position 0.25 cm perpendicular to the wafer line, is taken from an intermediate position from the plume center in this series. The BFTEM image in Figure 27 (c) shows sign of intensity variations in the top part of the CCS film region. The corresponding DP from the CCS film in Figure 27 (f) shows both diffuse scattering and two reflections in the lateral direction which is broadened azimuthally. An objective aperture was placed at one of the reflections as marked in the DP, and the corresponding DFTEM image is presented in Figure 27 (i). The crystalline regions appear as nanocrystalline columns which form in the upper part of the CCS film, and thus later during film growth as the thickness is increased.

The TEM results (in Figure 27 (d), (g) and (j)) from the lamellae at the wafer center in position 1.25 cm, represents the closest position to the plume center in this series. The BFTEM image and DP presented in Figure 27 (d) and (g), respectivly, are equivalent to the results presented in Figure 26 (g) and (n) from the series parallel to the wafer center line. A DFTEM image obtained from the objective aperture illustrated in the DP in Figure 27 (g), is presented in Figure 27 (j). The electron scatter of nanocrystalline regions with column shape. The columns appear in the upper part of the CCS film, but lower than observed in position 0.25 cm in Figure 27 (i).

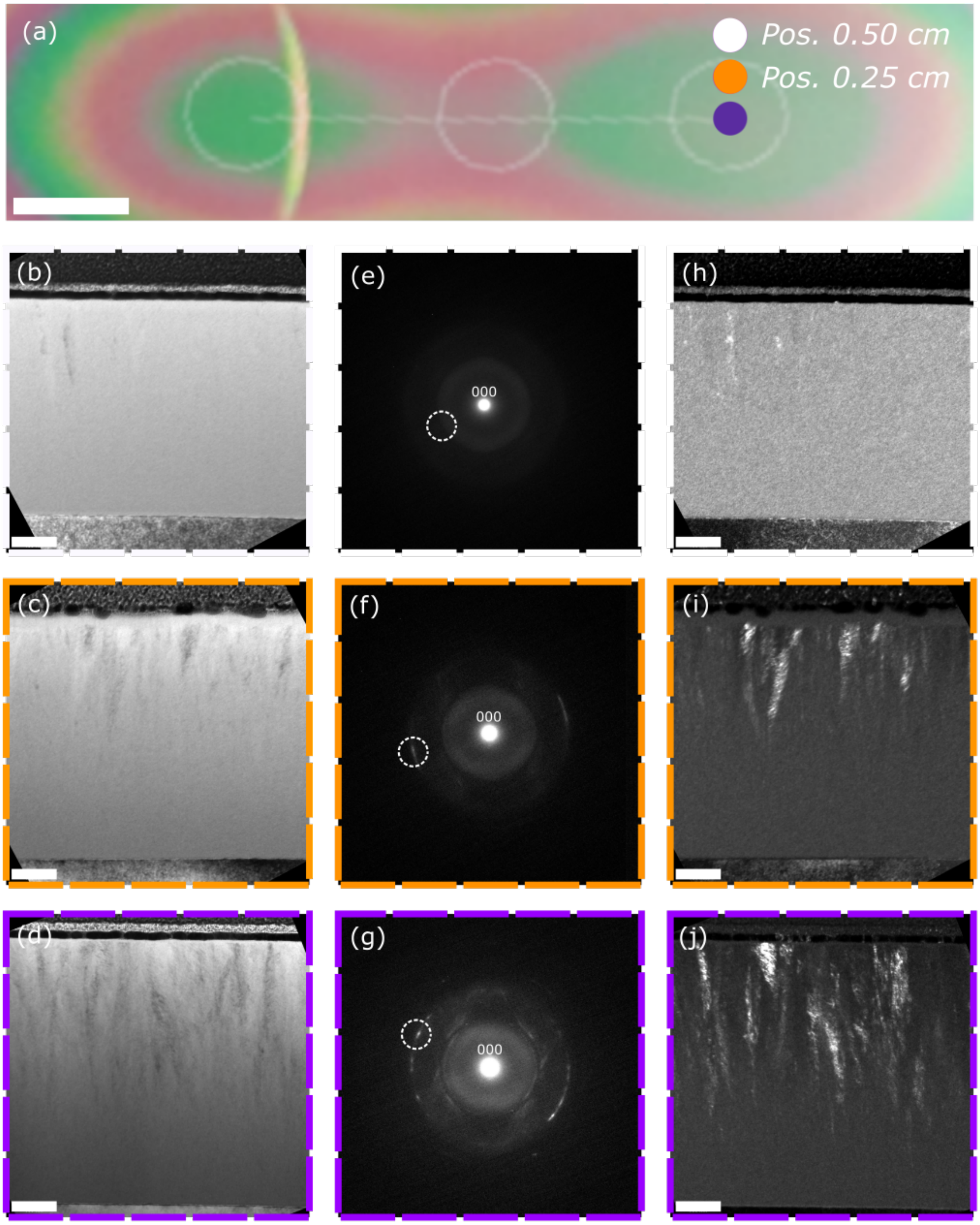

Figure 27: (a) Plan view photography of the CCS film with colored circles for the approximate location of the lamellae in the series perpendicular to the wafer center line. (b-d) BFTEM images of the cross-sectional lamellae showing the substrate at the bottom. (e-g) DPs from the CCS film region. Dashed circle marks the objective aperture used for the (h-j) DFTEM images. The scale bar of the plan view photography and cross-sectional BFTEM image are 0.5 cm and 100 nm, respectively.

Structural Properties Across the CCS Film

As seen in Figure 26, the structural properties across the series parallel to the wafer line of the CCS film vary from polycrystalline structure to an amorphous structure before nanocrystalline columns grow after an initial amorphous region. The results support the finding of Solstrand [76] and Michaelsen [77] for their characterization of an equivalent CCS film. They both observed a transition from a crystalline to an amorphous structure along the wafer center line in the CCS film with structural properties similar to that of rutile. The findings of this thesis provide additional results by revealing local variations within the disordered regions at the wafer center in position 0.0 cm, and around the second plume at position 1.25 cm. One can thus confirm the speculative statement of Solstrand that the structure might be nanocrystalline at the second plume center.

From Figure 26, the film growth results in crystalline columns at the first plume in position -1.75 cm, -1.25 cm and -0.75 cm. According to the zone model presented in section 2.4.2, the crystalline columns are characteristic growth where surface diffusion is dominant as in zone II [47]. At position 0.0 cm and 0.75 cm, the structure is amorphous, which is a characteristic feature for quenched growth as in zone I [47]. It thus appears as one of the deposition parameters increases the activation energy for crystal growth by prohibiting surface diffusion, or by making the structure disordered. As one transitions from a zone with crystal growth where surface diffusion is dominant, as in zone II, to one with an amorphous structure where it is negligible, as in zone I, it appears as one of the deposition parameters are altering the growth conditions across the series.

Across the CCS film, the doping concentration and the thickness of the TiO_2 capping layer increases from one plume center to the other. The characterization performed by Solstrand [76] on the reference sample without the CrN doping, showed that the structure became predominantly amorphous across the film when the thickness of the capping layer was increased. Similar studies reported a loss of crystallinity when TiO_2 was grown under N process gas compared to O, where the loss of crystallinity is expected to be due to increase of O defects in the lattice [70, 72]. The reduced density of O on the surface during growth, may thus produce challenges for growth of crystalline grains, and as the thickness of the capping layer is increased across the CCS film, this affect can potentially be more dominant.

The incorporation of the Cr and N is also expected to introduce O defects into the structure [17]. As the doping concentration is increased this may contribute to the transition to an amorphous structure along the centre line as well. Additionally, Nematollahi et al. [74] proposed Cr atoms to function as nucleation sites for crystal growth as they could function as point barriers in the surface landscape during growth by PLD. The Cr content in the CCS film is expected to be greater than the nominals in their work, which was between 2-5%. They observed a decrease in grain size as a function of Cr content. The high Cr content may increase the nucleation rate, and the film studied in this thesis may thus be nanocrystalline rather than amorphous due to smaller grain sizes.

In Figure 27, the findings from the series perpendicular to the wafer center line show that the growth of the nanocrystalline regions is sensitive to the position in relation to the plume center. Chu et al. [46] observed a gradual decrease of the kinetic energy away from the plume center of a Ti ablated plume where the decrease was more dramatic at lower laser fluence (3 J/cm^2), and at higher process gas pressures (10^{-6} torr). According to the zone models introduced in 2.4.2, sufficient energy to activate surface diffusion processes can change the structure from amorphous to nanocrystalline columns, and a transition from zone I to zone T or II. The decrease in kinetic energy provided to the adatoms as a function of position in relation to plume center is expected to contribute to the variation in growth modes across the series. In Figure 27, the nanocrystalline columns disappear only 0.5 cm away from the plume center.

As seen by the results in Figure 27, the position in relation to the plume center is important. At position 0.0 cm all the material is deposited away from the plume centers, which may explain why growth from surface diffusion is reduced as the kinetic energy provided to the adatoms is less. In section 3.1, the number of pulses from the TiO_2 target is less than that of the CrN target, which indicate that more materials is deposited in each pulse from the TiO_2 target. There are thus a greater number of adatoms at the surface from deposition of the TiO_2 target, than from the pulses from the CrN target. When surface diffusion is activated, this is a benefit as the nucleation rate and chance of adatoms finding each other is high. When surface diffusion is negligible, this can quench the growth where the atoms deposit where they land. The few number of atoms in the CrN plume may thus facilitate for an amorphous structure.

Additionally, the film growth at the second plume in position 0.75 cm, 1.25 cm and 1.75 cm utilize the flank of the TiO_2 plumes deposited at the first plume center. The importance of the position in relation to the plume center was illustrated in Figure 27. The initial deposition may thus be amorphous or of poorer crystalline quality, and can contribute to the increase of the activation energy for growth of crystal grains. Conversely, the film growth at first plume in position -1.75 cm, -1.25 cm and -0.75 cm, utilize the flank of the plumes deposited at the second plume center, which can alter the growth conditions. Especially, the number of atoms from the CrN plume is low, resulting in a low number of atoms being deposited at a time.

The local variation of the nanocrystalline region across the series in Figure 27 further explains why Raman Spectroscopy and XRD were not able to pick up these features as the crystalline signal was most likely dominated by signal from the amorphous regions. These findings thus highlights why characterization by TEM is effective if one seeks to understand the local structural properties in greater details in CCS films.

To summarize, the structure of the CCS film varies continuously across the wafer, where different zone models for film growth is applicable description at different locations. The doping concentration, the thickness of the capping layer, the position in relation to the plume center, and the choice of method for the c-PLD can all potentially contribute to the change in growth modes as the CCS film structure goes from a crystalline to an amorphous from the first plume to the second plume center. At the first plume, zone II where surface diffusion is dominant provide an applicable description, while at the wafer center and past it, zone I for quenched growth is a better description. The following section will study the different lamellae in greater details to better understand the change in growth modes across the CCS film.

4.2 Column Growth at the First Plume

An overview of the lamella series was presented in the previous section to evaluate the trend of the characteristic features across the CCS film. In this section the CCS film structure at position -1.25 cm and -0.75 cm is studied in greater details with a special focus on phase identification and the orientation of the structure. Across the two lamellae, regions with strong diffraction signal were identified, which indicate that the crystalline regions from the selected area were aligned on a zone axis with strong constructive interference. The regions are referred to as regions of interest (ROI)s, and were studied in greater detail to obtain further insight into the structure, and the CCS film growth.

Example of Indexation of DPs for Phase Identification

The results of the section will show that the crystalline regions differed within the CCS film structure, and that the DPs were assigned to different zone axes of predominantly the rutile structure. An example is provided for the indexation of the first DP, but the presentation of theoretical and experimental d-spacings will be included in the Appendix C for the remaining of the DPs to avoid repetition. The indexation of the DPs were performed as described in section 3.4 by the use of the Spot ID v1 tool in the Recipro software [79].

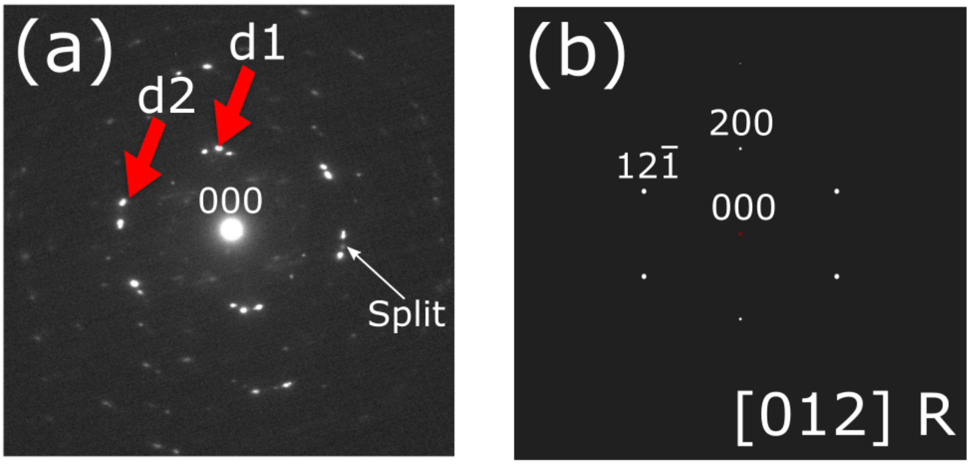

Figure 28: (a) DP from a selected area of a cross-sectional image of the CCS film. Red arrows indicate reflections with measured d-spacings. (b) Simulated DP of the <012> zone axis of the rutile structure. A split is identified for the DP as marked in (a).

Figre 28 (a) show a DP from a ROI at the first plume center in position -1.25 cm. The reflections is a result of constructive interference from scattering of periodic atomic planes within the diffracting volume. The d-spacing in the tetragonal lattices was introduced in eq. (3), and correspond to the interplanar spacing between neighbouring atomic planes in the structure. The orientation of the reflections in reciprocal space is orthogonal to the direction of the periodic planes in direct space. As the rutile and anatase structures differ, indexation of the DPs can thus reveal which structure is present, and at which orientation.

The red arrows in Figure 28 (a) illustrate the reflections with measured d-spacings, and their experimental values together with the closest theoretical candidates for rutile and anatase, are presented in Table 3. The Recipro software were utilized to find zone axis candidates from rutile and anatase, and they are listed in Table 3 as well. The <012> orientated rutile structure was the only candidate which match the d-spacing of the atomic planes, and their orientation in relation to each other. $d1$ and $d2$ can thus be assigned to the $(2\bar{1}1)$ and (020) rutile planes, respectively, when viewed down the [012] zone axis. In Figure 28 (a), a split in the reflections is identified, and indicate two crystalline regions on equivalent axes, but with an angular difference in perpendicular to the probe direcrtion.

Table 3: Theoretical and experimental d-spacing for indexation in Figure 28. Rutile [012] was identified as the phase and orientation present. The closes d-spacing of rutile and anatase is presented together with the zone axis candidates obtained from the Spot ID v1 tool in the Recipro software [79].

Indexation of DP		
Experimental DP	Rutile	Anatase
d1 = 2.286 Å	$d_{200,020}$ = 2.297 Å	$d_{110,112,021,201}$ = 2.332 Å
d2 = 1.684 Å	$d_{211,121}$ = 1.687 Å	$d_{012,102,121,211}$ = 1.666 Å
Recipro candidates	[012]	No candidate found

The presentation of the conventional TEM results for the current and following sections, are included in overview figures, and will among other things include an indexed DP together with a DP with indications of the reflections used for indexation and simulated DP obtained from Recipro [79]. Tables similar to Table 3 will be included in Appendix C.

Phase Identification at the First Plume Center (Position -1.25 cm)

Conventional TEM techniques were performed at the first plume center in position -1.25 cm, and the results are presented in Figure 29. In Figure 29 (a), the BFTEM image from the cross-sectional view of the substrate, CCS film and protection layer is presented. The DP of the CCS film in Figure 29 (b) was indexed in accordance with the indicated reflections in Figure 29 (c). The presence of predominantly the rutile structure orientated on the <012> zone axes was identified within the diffracting volume of the electron probe. A DP from the Si substrate is included in Figure 29 (d) for orientation reference in reciprocal space. The substrate is aligned on the <110> zone axis, such that the {002} reflections are parallel to the substrate surface. Simulated DP of the <012> rutile zone axis was included in Figure 29 (e) to show the agreement between experimental and theoretical DPs. From the comparison between the two DPs, one see that there is a split in the reflections in the DP from the CCS film. The split indicates two crystalline regions which are slightly disorientated, but on equivalent zone axes. In Figure 29 (b), one additionally see that the orientation of the (200) rutile planes is close to aligned with the (002) of the substrate. A DFTEM image from the ($\bar{4}$00) reflection presented in Figure 29 (f) shows tendencies of column growth with the stacking of {200} planes parallel to the substrate. The tendencies of column growth is highlighted in Figure 29 (g).

The split of the reflections in the DP from the CCS film in Figure 29 (b), indicates two crystalline regions which are slightly disorientated, but on equivalent zone axes. A merged DFTEM image of the (12$\bar{1}$) and ($\bar{1}\bar{2}$1) reflections is presented in Figure 30 (a). The approximate size and location of the objective apertures are shown in Figure 29 (c), and color coded to the signal in the DFTEM image of Figure 30. Figure 30 (b) contains highlighted regions which visualizes the columnary growth. There are intensity variations with the columns, which indicate that the regions scatter differently. Such variations can be a result of local regions orientated on a different zone axis, an amorphous region, an interface between grains or voids in the structure. One is not able to distinguish between them based on these results.

Six regions containing moiré fringes are highlighted and magnified in Figure 30 (c). These are slightly disorientated grains orientated in the probe direction. The fringes are interference effects from electrons scattering of the neighbouring disorientated planes. The misalignment indicated by the moiré effects show that the column growth is not directly vertical

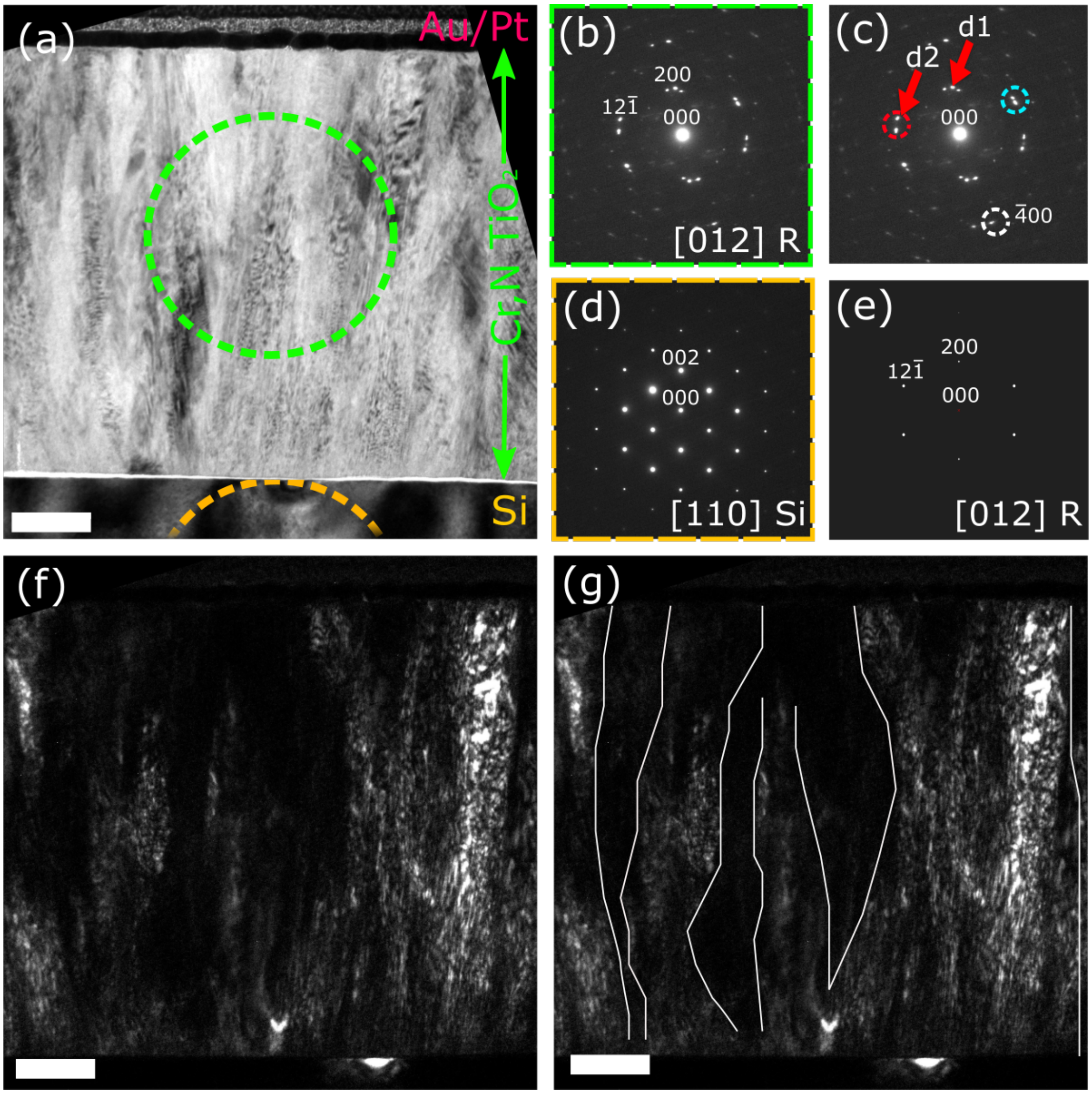

Figure 29: (a) BFTEM image from the cross-sectional view of the substrate, CCS film and protection layer at position -1.25 cm. (b/c) Indexed DP from the CCS film according to reflections highlighted by the red arrows. (d) The DP of the substrate shows orientation reference in reciprocal space. (e) Simulated DP of the <012> orientated rutile structure [79]. (f) DFTEM image of the ($\bar{4}00$) with (g) highlighted columns. The objective aperture is shown in (c). The red and blue apertures correspond to the merged DFTEM image in the following figure. Scale bars are 100 nm.

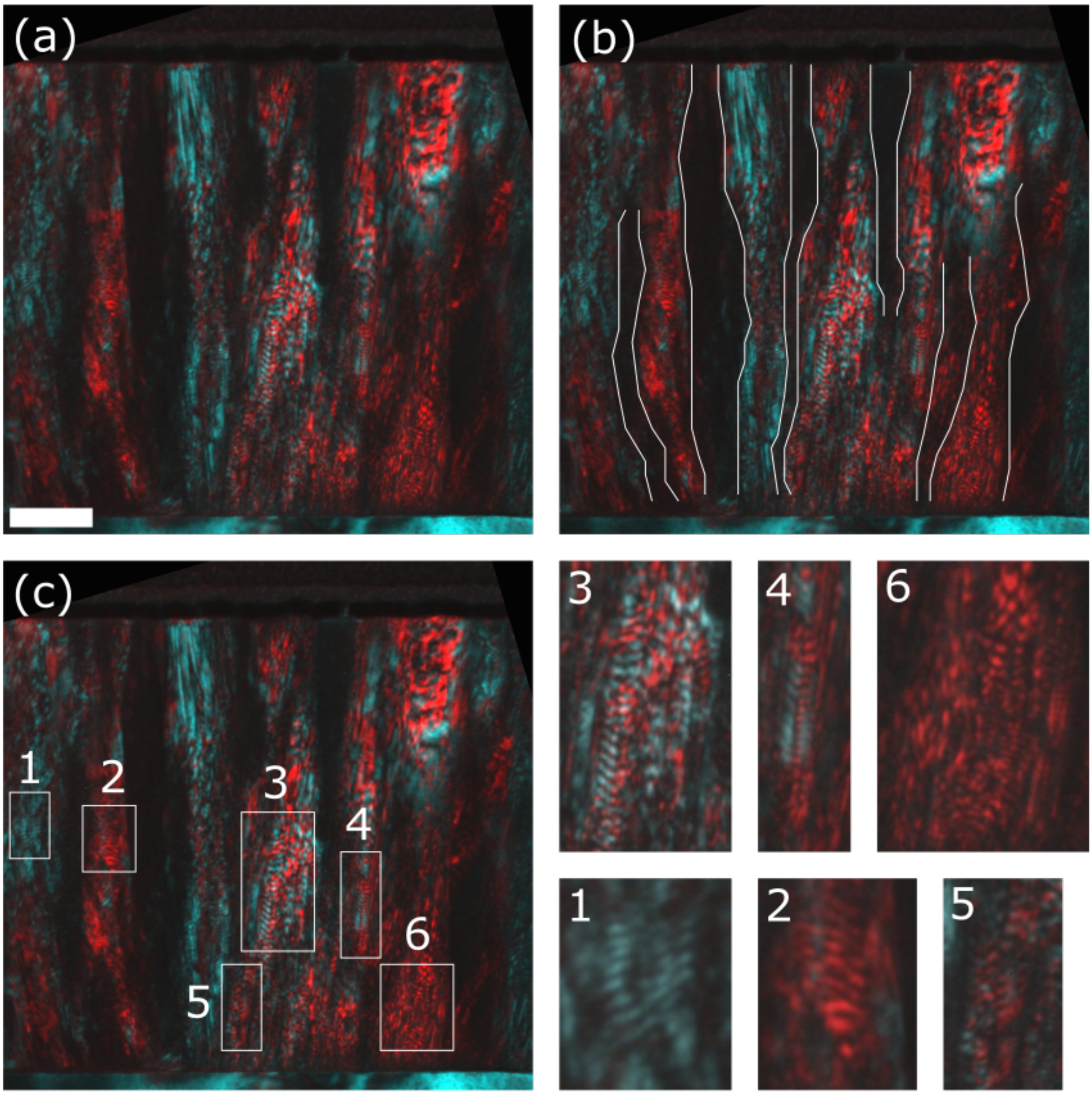

Figure 30: (a) A merged DFTEM image from the $(12\bar{1})$ and $(\bar{1}\bar{2}1)$ reflections from the DP of the CCS film at position 1.25 cm with (b) highlighted columnary growth. Moiré effects are present within the columns, and are (c) highlighted and magnified in the DFTEM image. Scale bar is 100 nm.

A HRTEM image from the substrate-film interface is presented in Figure 31. The Si (100) substrate is aligned on the <110> zone axis, which is seen in Figure 31. An amorphous layer of SiO_2 is present at the interface. The substrate was not polished prior to the deposition, and the oxide layer is thus expected to be a consequence of oxidation at the surface. Additionally, there are some roughness on the surface from the wafer cut seen by the height difference across the image.

Within the CCS film, the structure stacks crystalline planes parallel to the substrate. The d-spacing is assigned to the {100} rutile planes as the fourier transform of the crystalline region is identified as the [001] zone axis of the rutile structure. Experimental and theoretical d-spacings are included in Table C2 in the Appendix C. (100) and (010) planes of the rutile structure belong to the {100} family of planes in tetragonal structures due to the symmetry of the structure presented in section 2.1.1. The results thus support growth of a preferred {100} orientation parallel to the substrate at position -1.25 cm. Additionally, the HRTEM results show that the preferred orientation occurs in the early stages of film growth.

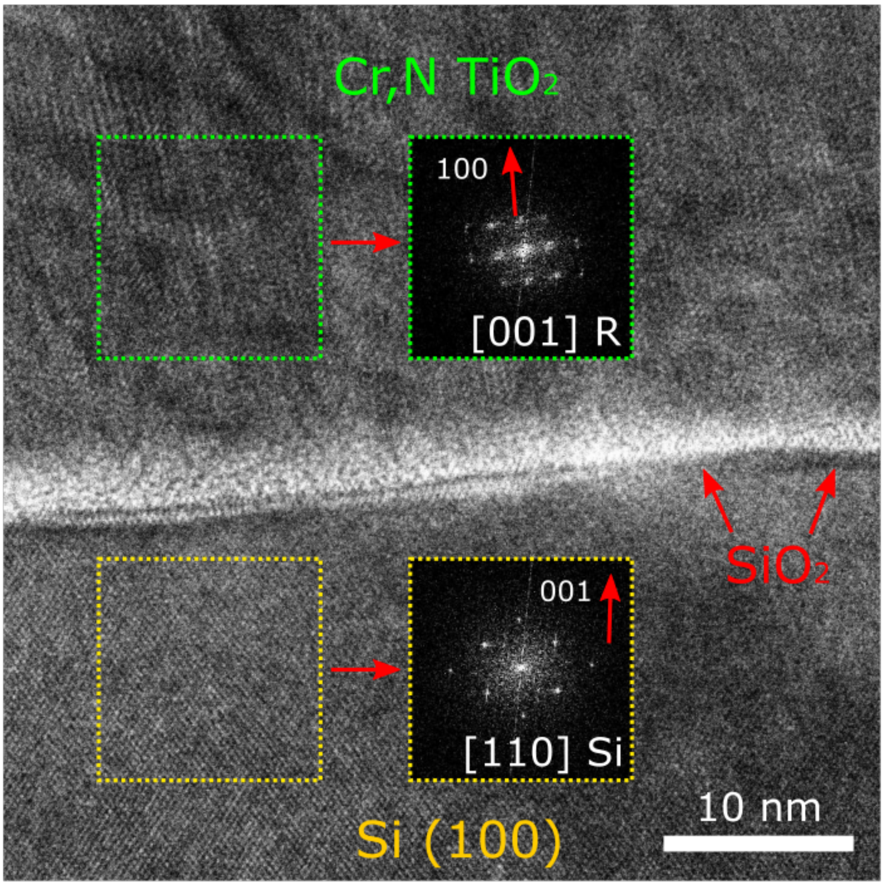

Figure 31: A HRTEM image of the substrate-film interface at the lamella at position -1.25 cm. The inserted images are fourier transforms from the color coded boxed regions.

Phase Identification between the First Plume and Wafer Center (Position -0.75 cm)

Conventional TEM techniques were performed at the intermediate step between the first plume and the wafer center in position -0.75 cm. Three different regions at the lamella provided strong signal from the diffracting volume, and was further studied to obtain insight in the CCS film growth through identification of the phase and orientation present. The SAED patterns, and the BF- and DFTEM images from the three different ROI are presented in Figure 32, 33, and 34, respectively. They are referred to as the first, second and third ROI in the order which they are presented.

The conventional TEM results from the first ROI is presented here. The BFTEM image of the cross-sectional view of the substrate, CCS film and protection layer is presented in Figure 32 (a). The DP of the CCS film in Figure 32 (b) was indexed in according to the indicated reflections in Figure 32 (c). The presence of predominantly the rutile structure orientated on the <101> zone axes was identified within the diffracting volume. The theoretical and experimental d-spacings are included in Table C3 in Appendix C. The DP of the substrate is included in Figure 32 (e) to visualize how the (020) planes are orientated parallel to the substrate. The DFTEM image of the $(0\bar{4}0)$ reflection in Figure 32 (f) shows columnary growth similarly to the results of the previous section with intensity variations within. Noticeable, parts of the protection layer have vanished at this location as a result of the thinning and polishing step during sample preparation. However, ion implantation scales roughly one nm/kV. The operating voltage at these steps were in the range 2 and 30 kV. Only the top part would thus potentially contain ion implantation and altered structural properties.

The conventional TEM results from the second ROI is presented here. The BFTEM image of the cross-sectional view of the substrate, CCS film and protection layer is presented in Figure 33 (a). The DP of the CCS film in Figure 33 (b) was indexed according to the indicated reflections in Figure 33 (c). The presence of predominantly the rutile structure orientated on the <100> zone axes was identified within the diffracting volume. The theoretical and experimental d-spacings are included in Table C4 in Appendix C. The DP of the substrate is included in Figure 33 (e) to visualize how the (020) planes are orientated parallel to the substrate similarly to the findings at the first ROI in Figure 32. The DFTEM image of the $(0\bar{4}0)$ reflection in Figure 32 (f) shows columnary growth made up of smaller crystallites as seen in the magnified image in 32 (g). Both the results of the first and second ROI at the lamellae show a preference for the {100} rutile planes parallel to the substrate.

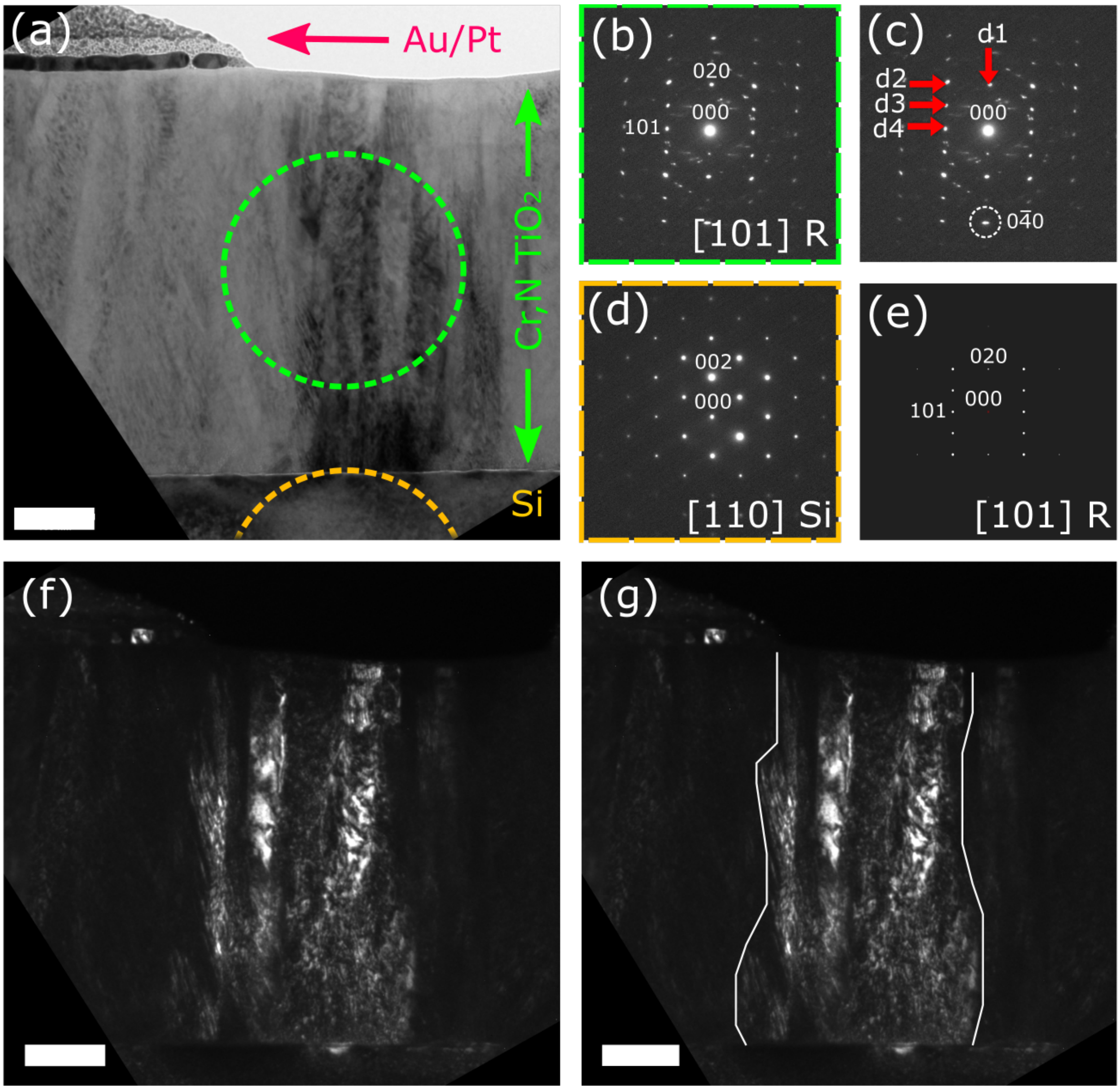

Figure 32: (a) BFTEM image from the cross-sectional view of the substrate, CCS film and protection layer of the first ROI at position -0.75 cm. (b/c) Indexed DP from the CCS film according to the reflections highlighted by the red arrows. (d) The DP of the substrate shows orientation reference in reciprocal space. (e) Simulated DP of the <101> orientated rutile structure [79]. (f) DFTEM image of the (0$\bar{4}$0) with (g) highlighted columns. The objective aperture is shown in (c). Scale bars are 100 nm.

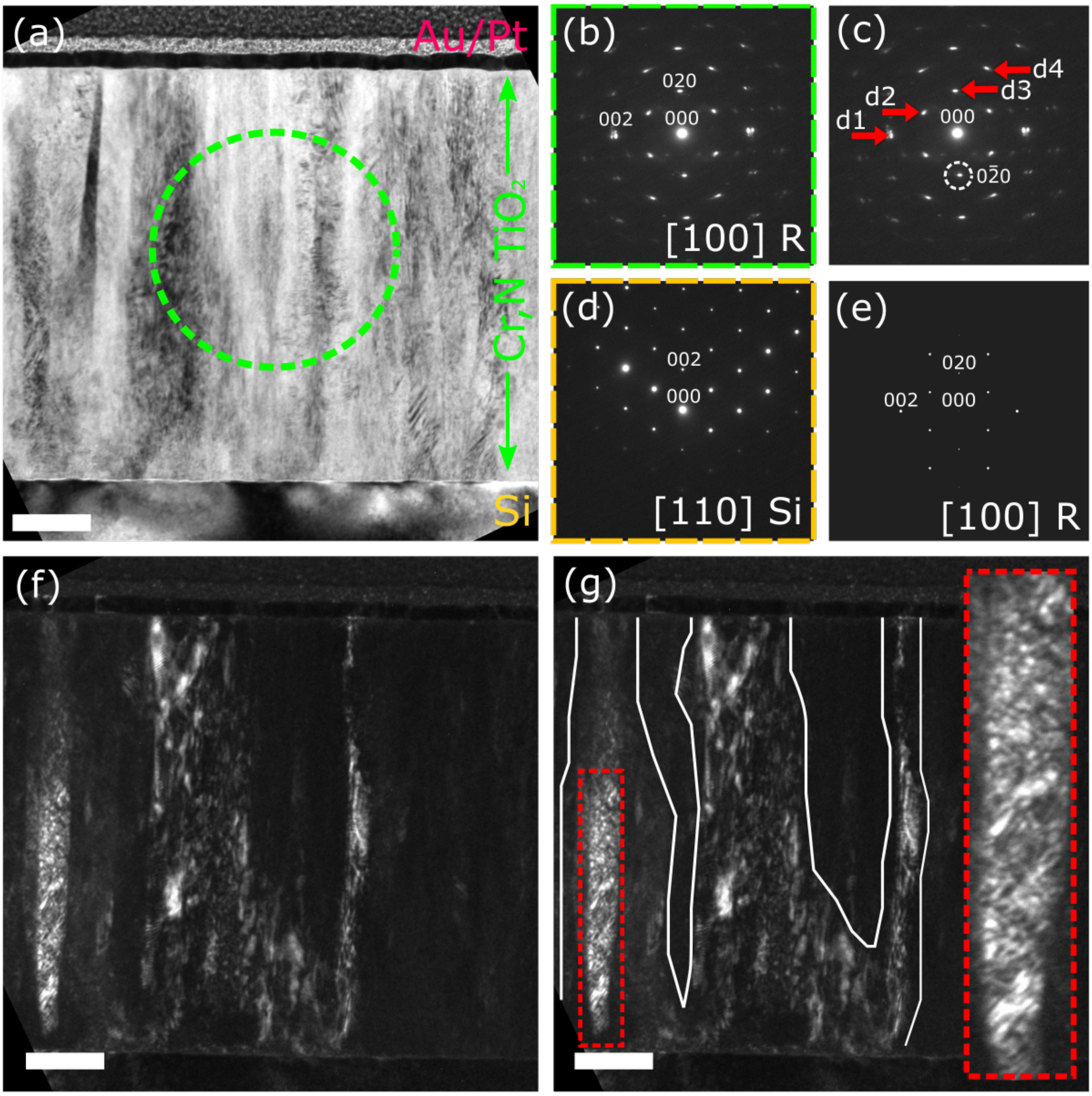

Figure 33: (a) BFTEM image from the cross-sectional view of the substrate, CCS film and protection layer of the second ROI at position -0.75 cm. (b/c) Indexed DP from the CCS film according to the reflections highlighted by the red arrows (c). (d) The DP of the substrate shows orientation reference in reciprocal space. (e) Simulated DP of the <100> orientated rutile structure [79]. (f) DFTEM image of the (0$\bar{2}$0) with (g) highlighted columns and a magnified image showing smaller crystalline grains within the columns. The objective aperture is shown in (c). Scale bars are 100 nm.

A third ROI was located at the lamella taken out at position -0.75 cm, and the results are presented in Figure 34. The BFTEM image of the cross-sectional view of the substrate, CCS film and protection layer is presented in Figure 34 (a). The DP from the CCS film is presented in Figure 34 (b), and the d-spacings are measured according to the red arrows highlighted in Figure 34 (c). Diffraction results in one strong systematic row which the d-spacing for the first reflection corresponds to the {110} planes of the rutile structure. The systematic row is close to aligned parallel to the substrate surface, which indicate the orientation of the {110} rutile planes within the diffracting volume. The results thus show a preference for the {110} rutile planes parallel to the substrate may develop. The experimental and tabulated d-spacings are included in Table C8 in the Appendix.

A DFTEM image from the {110} reflection is presented in Figure 34 (d). As highlighted in Figure 34 (e), the scattered region shows a clear crystalline column, which width extends a couple hundred nm. The column is built up by smaller crystalline grains as seen by the highlighted region in Figure 34 (e) which is magnified in (f). The region in between the bright regions in the DFTEM image can be amorphous or nanocrystalline with different orientations of very small crystallites. A second region is highlighted in Figure 34 (e), and is magnified in (g). The magnified image shows that the column is a result of two neighbouring regions coalescing during the later stages of growth.

A DFTEM image from the $(2\bar{2}0)$ reflection is presented in Figure 35 (a) with highlighted ROIs in (b). There are networks of structures seen by the three top red highlighted regions within the column. The origin of these is unknown, but the structure contains d-spacing equivalent of the $(2\bar{2}0)$ of the rutile structure. The bottom highlighted region shows that the dark region between the initial growth in Figure 34 (h) is a crystalline region that scatter into the $(2\bar{2}0)$ reflection.

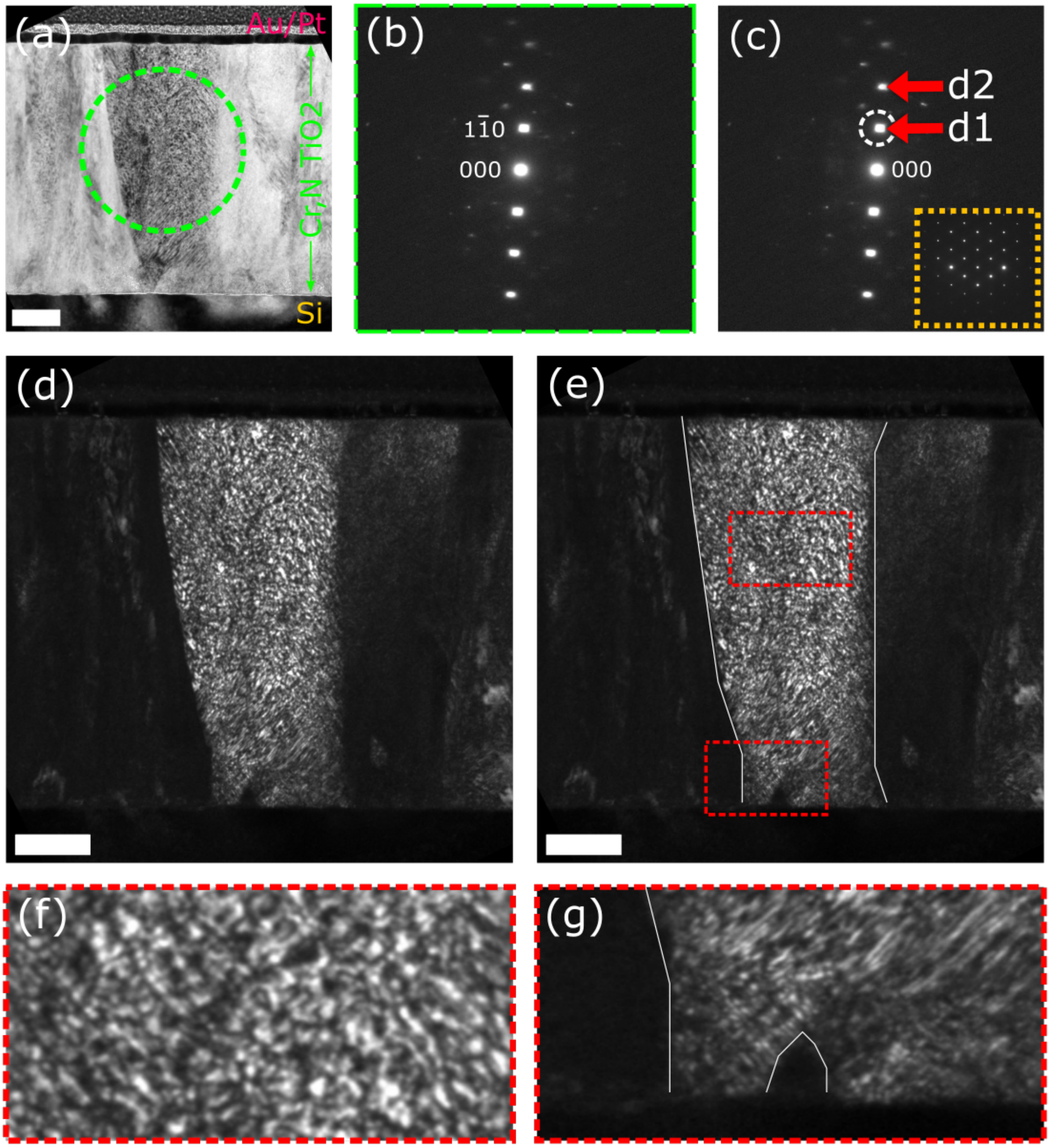

Figure 34: (a) BFTEM image from the cross-sectional view of the substrate, CCS film and protection layer of the third ROI at position -0.75 cm. (b/c) Indexed DP from the CCS film according to the reflections highlighted by the red arrows. The DP of the substrate is inserted for orientation reference in reciprocal space. (d) DFTEM image from the $(1\bar{1}0)$ reflection with (e) highlighted column, and magnified areas of (f) smaller crystalline grains within the column, and (g) hwo the column is a result of neighbouring regions coalescing during growth. Scale bars are 100 nm.

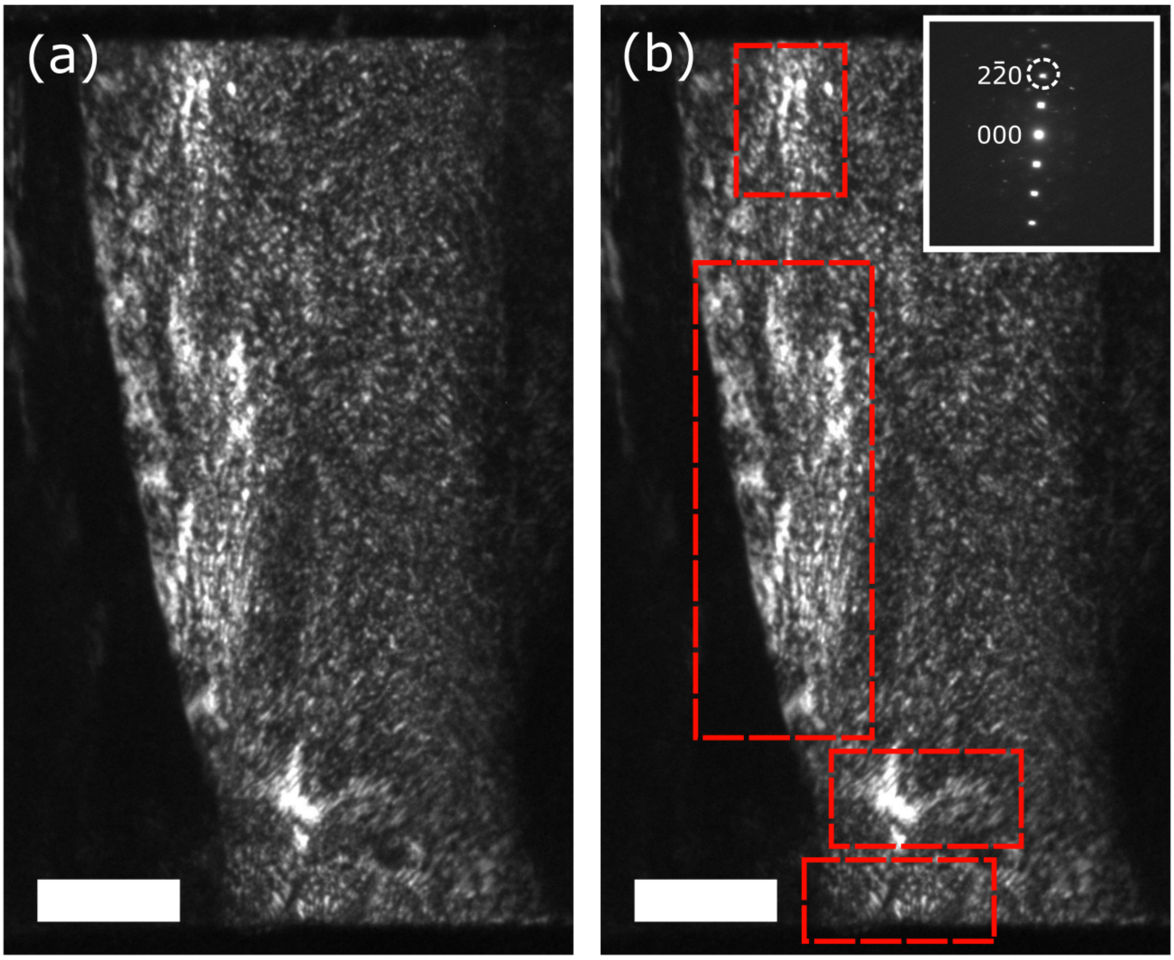

Figure 35: (a) DFTEM image from the ($2\bar{2}0$) reflection shows a crystalline column of smaller grain. (b) Four highlighted ROIs are marked with red rectangles with inserted DP from the CCS film. See result section for further details. Scale bars are 100 nm.

A HRTEM image was obtained from the substrate-film interface at the lamella taken out from position -0.75 cm, and is presented in Figure 36. The orientation of the substrate is aligned on the <110> zone axis. The fourier transform of the substrate shows how the normal of the {100} planes are orientated parallel to the substrate-film interface. The fourier transform from the CCS film shows distinct periodicity close to the direction parallel to the substrate surface. The spacing between the two main reflections matches the d-spacing of the {110} spacing planes. The d-spacing is presented in Table C6 in the Appendix.

The amorphous SiO_2 layer at the substrate-film interface varies in thickness across the HRTEM image in Figure 36. The crystalline region found here is located above the thinnest part of the layer. The variation in roughness from the thickness variation may provide local variations of the growth conditions at the initial stages.

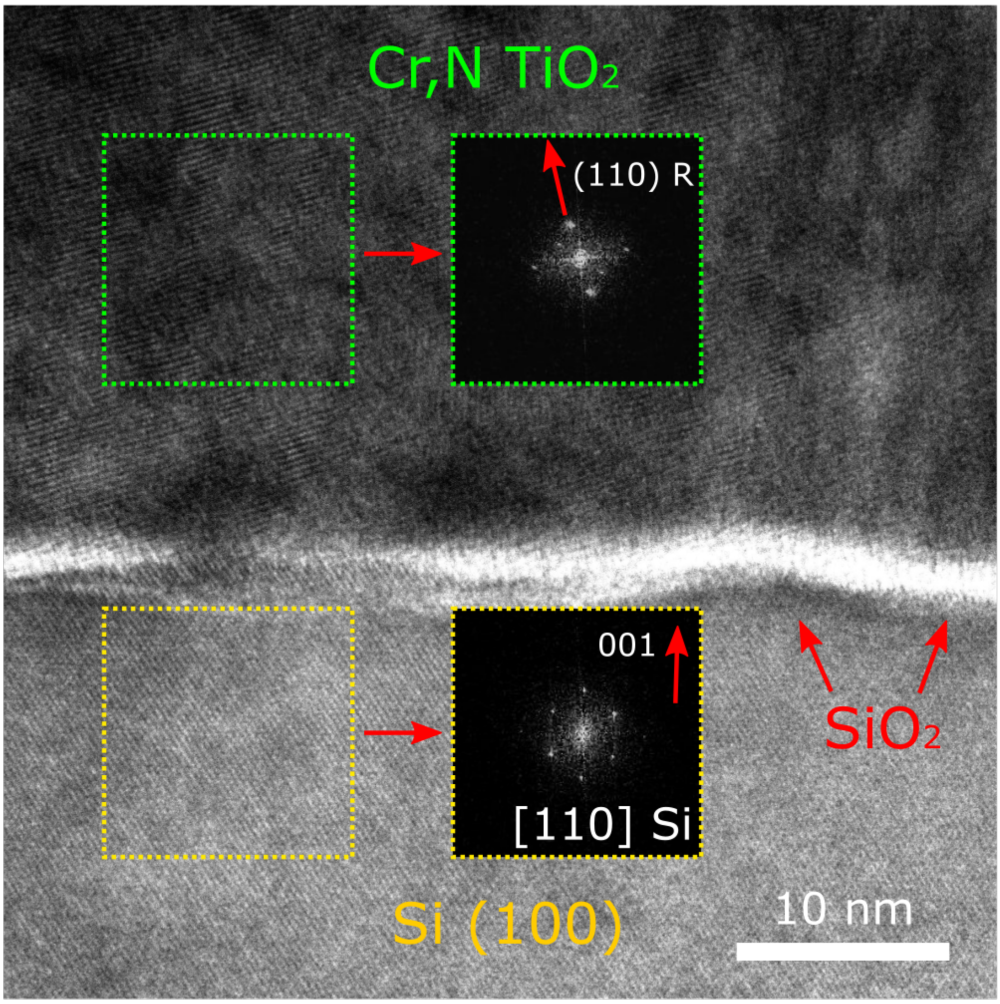

Figure 36: A HRTEM image of the substrate-film interface at the lamella at position -0.75 cm. The inserted images are fourier transforms from the color coded boxed regions. See results section for further description.

The Origin of the Preferred Phase and Orientation

The phase identification of the crystalline region at the first plume in position -1.25 cm and -0.75 cm show the presence of predominantly the rutile structure in the diffracting volume. In Figure 32, 33 and 34, a preference for the stacking of the {200} and {110} rutile planes parallel to the substrate was identified. Michaelsen [77] characterized an equivalent CCS film at the first plume, and observed a predominantly preferred {200} and {110} planes parallel to the substrate. The results from the two characterization techniques thus agrees. The XRD results are obtained from a larger area than the TEM, and thus provides statistics for the findings of this thesis. The TEM results show columnary growth made up of smaller crystallites. In Figure 29, 32 and 33, different zone axes are identified for the rutile structure, but with equivalent planes stacked parallel to the substrate. There does not appear do be an in-plane dependence in relation to the substrate for the growth of the rutile structure as the lamellae were aligned on the [110] zone axis of the substrate for each experiment.

The HRTEM result in Figure 31 further shows that the preferred stacking occurs initially, and is not an affect of evolutionary selection. In the HRTEM images in Figure 31 and 36, the presence of an amorphous SiO_2 layer at the substrate surface is identified. The energy landscape of the surface is thus expected to be isotropic for the initially deposited atoms. Additionally, the thickness variations and roughness in the substrate-film interface present in both HRTEM images, may result in local growth conditions for the film growth.

As discussed in section 4.1, the zone model for the first plume can be described by zone II where surface diffusion is dominant. According to van der Drift [53], the preferred orientation on an amorphous surface is commonly observed to be the densest one, and on a rough surface, he also states that the horizontal growth rate can become more important than the vertical. As presented in Table 1, the {110} and {100} facets of the rutile phase contain the two lowest surface free energies of the structure. They are 0.74 and 0.76 J/m^2, respectively [57], and are expected to be stable surfaces which do not grow fast. Higher energy facets such as the {101} and {001}, have surface energies of 1.11 J/m^2 and 1.51 J/m^2, respectively. The {101} and {001} planes are orientated perpendicularly to the substrate surface in Figure 32 and 33, respectively. The preferential orientation may be a result of initial growth of reactive surfaces laterally, resulting in a stable facet orientated vertically, and thus parallel to the substrate, from the early stages of growth. Column growth vertically is then more likely to proceed once an anisotropic crystalline surface has formed. In Figure 30, the column growth are seen to not be perfectly vertically by the presence of Moiré fringes and altercation of orientation of the columns in Figure 30. The tilting effects could be a result of oxygen defects within the layers, relaxation of strain between neighbouring regions, an amorphous layer within the column, or interaction at the interfaces. One cannot conclude strongly about this from the results.

Rutile is identified as the dominant phase in the CCS film studied in this thesis, while anatase was identified by Solstrand [76] on a similar film without deposition from the CrN target. The incorporation of Cr and N atoms is thus expected to influence the favorization of rutile over anatase. Nematollahi et al. [74] proposed the Cr atoms to function as nucleation sites for crystal growth as they could function as point barriers in the surface landscape. After atoms have formed an islands or cluster, they are in a quasi-kinematical conditions trying to minimize the surface free energy in consideration of the time and energy available. Anatase contains a lower surface free energy than rutile, and may thus be preferential in the early stages when nanocrystalline regions are forming [58, 17]. Cr is documented to increase O defects in the structure, and can together with the N process gas facilitate for a rearrangement of the atoms to favor the rutile structure at the initial stages [17]. Such a reconstructive surface process was observed by Ali et al. [73] for incorporation of Nd in TiO_2 by PLD facilitating for growth of rutile over anatase. However, a theoretical study of Cr, N TiO_2 nanoparticles similar to Ali et al. [73] is not supporting this statement. The preferred phase and orientation can also be a result of such a reconstructive surface in the early stages of growth.

To summarize, the regions studied at the first plume in the CCS film show the presence of predominantly the rutile structure of column growth with $\{110\}$ and $\{100\}$ planes stacked parallel to the substrate. $\{110\}$ and $\{100\}$ facets have low surface free energies in the rutile structure, and are thus expected to grow slow. Higher energy facets are orientated perpendicular to the substrate. The lateral growth rate perpendicular to the substrate may contribute to the preferred orientation.

4.3 The Precence of Anatase Locally in the CCS Film

The second ROI presented in section 4.2 at position -0.75 cm was studied further as a secondary crystalline pattern appears to be present in the DP from the diffracting volume in the CCS film. The DP in Figure 37 is equivalent of the DP in Figure 33 (b/c). In Figure 37, there are a split in the reflections parallel and perpendicular to the substrate as marked by the set of arrows. Parallel to the substrate, the d-spacing of the weaker reflection is 2.447 Å, while the stronger reflection is 2.310 Å, which means that the crystal planes are separated by a further distance. In the perpendicular direction, the weaker reflection is separated by 1.364 Å, which is at a shorter distance compared to the electrons scattering of the planes to the strong reflection at 1.479 Å. Additionally, there are a set of weaker reflections marked by dashed circles in Figure 37, which indicates the presence of another structure in the diffracting volume.

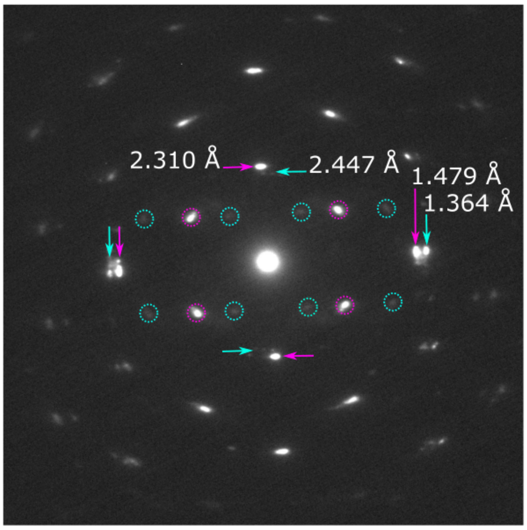

Figure 37: DP from the second ROI from the lamella between the first plume and wafer center in position -0.75 cm. A split between neighbouring planes are present in the lateral and vertical direction as indicated by the arrows.

Conventional TEM results are presented in Figure 38 to study this region in greater detail. The BFTEM image of the cross-sectional view of the CCS film in Figure 38 (a) is equivalent to the image in Figure 33 (b/c). In Figure 38 (b), the DP from the CCS film is presented with marked reflections that have been indexed to the <100> orientated rutile structure. The indexation was done according to the method presented in section 3.4, and a table of theoretical and experimental d-spacings are included in Table C4. The <100> orientated rutile structure was the only potential candidate presented by the Recipro software, and the simulated DP is included in Figure 38 (c).

The weaker reflections assigned to the other structure was marked in the DP of the CCS film in Figure 38 (d). The only potential candidate found for the DP was the $<11\bar{1}>$ anatase structure. The theoretical and experimental d-spacings are included in Table C7 of the Appendix C. The simulated DP is included in Figure 38 (e). In Figure 37, the d-spacings of 2.310 Å and 2. 447 Å is indexed to the {020} rutile and {112} anatase planes, respectively, while the d-spacings of 1.479 Å and 1.364 Å is indexed as the (002) rutile and $(2\bar{2}0)$ anatase planes. An orientation relationship between the two structures may be present in the diffracting volume as one view the rutile and anatase structure down the <100> and the $<11\bar{1}>$, respectively. At the two orientations, the (002) rutile and $(2\bar{2}0)$ anatase planes are parallel to each other and the substrate, and the {020} rutile and {112} anatase planes are parallel to each other and perpendicular to the substrate within the diffracting volume. The potential orientation relation can be expressed as either ($<11\bar{1}>_A \, || <100>_R$, $\{112\}_A || \{020\}_R$) or ($<11\bar{1}>_A \, || <100>_R$, $\{220\}_A || \{002\}_R$).

To study the regions of the different structures, an objective aperture was placed around the $(00\bar{2})$ rutile and $(\bar{2}20)$ anatase reflection as visualised in Figure 38 (b) and (d), respectively, to make a DFTEM image from the different phases. A merged DFTEM image from the two reflections are presented in Figure 38 (f), and the signal is color coded to the objective apertures and phase. Rutile and anatase are assigned to the color magenta and cyan, respectively. In Figure 38 (g), the DFTEM image show regions of strong intermixing of the two signals together with three marked regions with dominant signal from the anatase phase.

Similar features were found at the lamella past the first plume center in position -1.75 cm. Splits occurs between the same reflections, and close to the lateral direction compared to the substrate. Additionally, a single crystalline column assigned to the anatase phase was identified within the cones at the wafer center. The results are included in Figure A1 of the Appendix A.

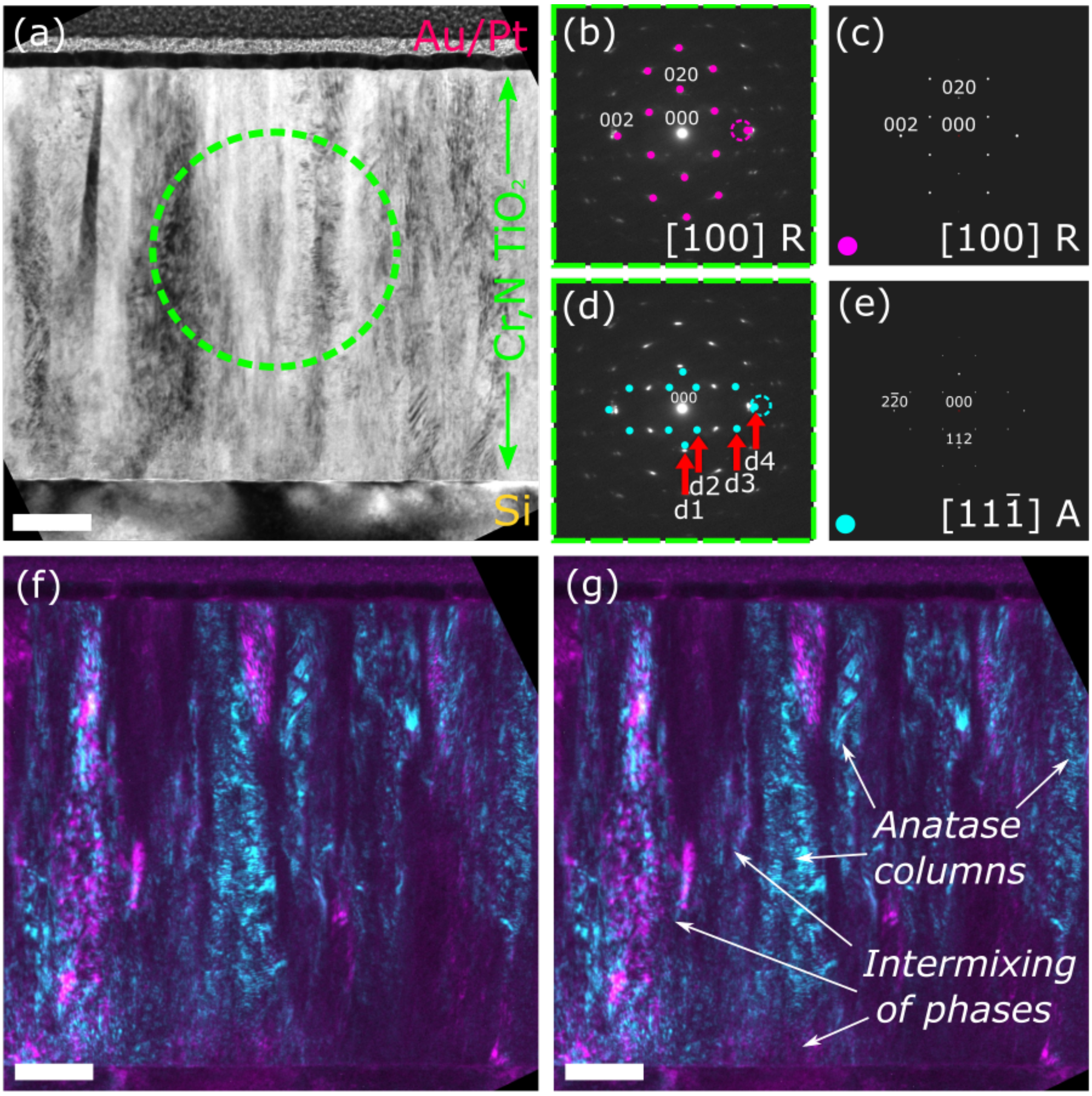

Figure 38: (a) BFTEM image from the cross-sectional view of the substrate, CCS film and protection layer at the second ROI at position -0.75 cm. (b) Indexed part of the DP from the CCS film assigned to the <100> rutile structure with (c) simulated DP at the orientation. (d) Indexed part of the DP from the CCS film assigned to the $<11\bar{1}>$ anatase structure with (e) simulated DP at the orientation. (f) A merged DFTEM image from the $(00\bar{2})$ and $(\bar{2}20)$ reflections of rutile and anatase, respectively, with (g) highlihgted regions of intermixed and anatase-dominantn signal. Scale bars are 100 nm.

The Origin of the Presence of Anatase Locally in the Film

In Figure 38, anatase was found locally within the film - both in intermixed regions but also as anatase dominanted columns. For the c-PLD, the growth conditions are altered as the process gas is cycled together with the change in deposition rate from the different target at each location in the series. Solstrand [76] observed anatase without deposition from the CrN target, and rutile with deposition. The preferential phase thus appears to be sensitive to the deposition parameters. According to the literature presented in section 3.2, both anatase and rutile could be obtained on a Si (100) substrate by altering substrate temperature and the process gas [65, 66, 67]. The substrate of the CCS film is kept at 550 °C, which is approaching the anatase-to-rutile phase transformation at $\sim$ 600 °C [61], however, the transition is observed to be pushed to higher temperatures for crystallites on the order of 5 nm [60]. Such crystallites are seen within the columns identified in section 4.2. The lower surface free energy of anatase structure also makes it likely to exists locally within the CCS film for such crystallites [17].

The indexation of the DP in Figure 38 indicates a potential orientation relations between the structures in the diffracting volume, expressed as either ($<11\bar{1}>_A$ $||<100>_R$, $\{112\}_A||\{020\}_R$) or ($<11\bar{1}>_A$ $||<100>_R$, $\{220\}_A||\{002\}_R$). The relation between parallel stacking of the {112} anatase and {020} rutile planes are commonly observed between anatase and rutile [17]. An important notion is that growth in PLD is far from equilibrium, and the atoms from each plume reconstruct bonds to the surface as bulk diffusion is not expected to be dominant. Growth conditions which facilitate for one structure over the other, may alternate as the deposition parameters are altered. The fact that the {112} anatase and {020} rutile planes are similar in nature, and orientated parallel to the substrate, can potentially facilitate for alternating growth as adatoms sticking to these surface would find similarities between the two structures. As the deposition parameters are altered, then this could potentially alter the growth of anatase and rutile.

The other orientation relation presence is that the {220} anatase and {002} rutile planes are stacked perpendicularly to the substrate. No documentation has been found in the literature observing this orientation relationship at this zone axis. Their d-spacings are 1.338 Å and 1.479 Å for the {220} anatase and {002} rutile planes, respectively [79]. As seen in Table 1, a common feature for the two planes are that they both hold the highest surface free energy of the two phases. They are thus expected to be highly reactive when surface diffusion is dominant. The relation between the two planes may thus be due to large growth rate in the lateral direction.

A magnified image of the dominant anatase column is presented in Figure 39 (a) with orientation of the {220} and {112} anatase planes marked in the DP from the region in (b). The column growth develops as seen in Figure 39 (c) from a region with intermixed signal in (d). The red arrows indicate regions where the anatase phase is dominant, and where the shape of the crystallites appears to be elongated in the lateral direction parallel to the orientation of the {220} planes. The {220} reflections are also stronger in intensity than the other reflections present at the $<11\bar{1}>$ anatase zone axis. The growth in the lateral direction, and the shape of the crystallites, can thus potentially be an influence for the development of anatase columns from an intermixed region.

To summarize, the indexation of the DP presented in Figure 38 indicate the presence of the anatase structure locally in the CCS film. The {220} planes of the anatase structure is orientated perpendicular to the substrate in the diffracting volume. The {220} facet has the highest surface free energy in the anatase structure. Lateral growth rate may be an important factor for the presence of the anatase structure in the CCS film.

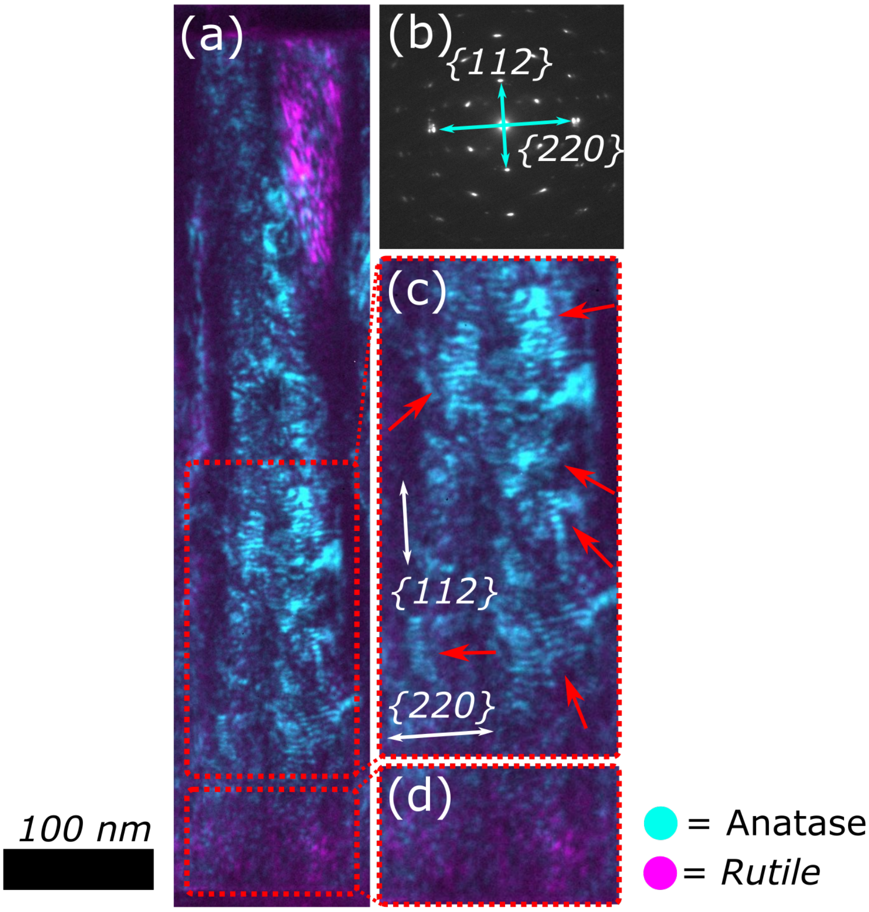

Figure 39: (a) Magnified DFTEM image of a dominant anatase (cyan) column obtained from the {220} reflection at position -0.75 cm. Signal from the {002} rutile phase (magenta) is also included in the image. (b) The {112} and {220} anatase planes are visualised in the corresponding DP. (c) A magnified image of the region with dominant anatase signal, and another (d) image with a clear intermixing of the signal close to the substrate. The red arrows indicate the presence of lateral shaped crystallites in the anatase regions. See section for further discussion of the results.

4.4 Growth of Inverse Crystalline Cones at the Wafer Center

Conventional TEM together with SPED was performed at the wafer center in position 0.0 cm. The CCS film is predominantly amorphous, but the lamella has intersected regions with the presence of inverse crystalline cones as seen in Figure 40. Such cones have been documented in different thin film deposition methods for quenched growth in zone 1 [50, 51]. The growth of such cones was introduced in section 2.4.2. The cone is a result of initial nucleation of a crystalline region, which grows laterally as a function of film thickness. If multiple such cones are developed close to each other, they can coalesce later in the growth process. The nucleation center is marked with a red circle in Figure 40 (b), while the white lines indicate the interface between amorphous and crystalline regions together with the blue dashed circles that indicate the approximate location where the cones coalesce.

The shape of the bottom part of the cones indicates if the TEM lamella contains the origin of the cone or not. The intersection of the edge of a cone would result in a parabola, while that which include the origin would result in a steep triangular shape, as illustrated in Figure 40 (e) and (f), respectively. A second region which does not contain the origin was found and is presented in Figure 40 (c) and (d). The DPs marked in Figure 40 (d), show a clear distinction between the amorphous and crystalline parts, and the corresponding DPs show a clear difference between the diffuse scattering in the amorphous, and the distinct reflections in the crystalline regions. The crystalline DP was indexed as the <$\bar{1}$11> rutile structure, and the theoretical and experimental d-spacings are included in Table C9 of the Appendix C.

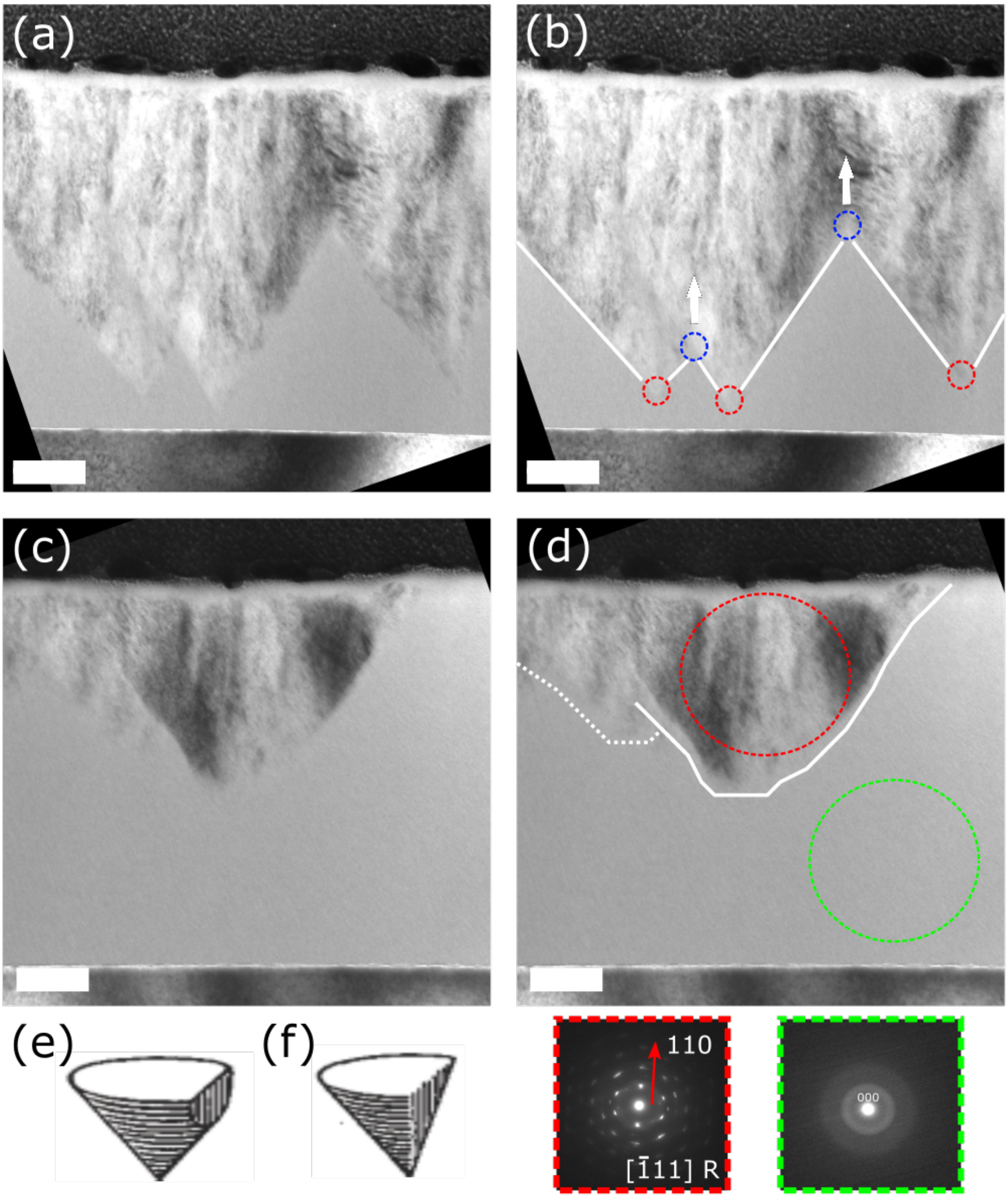

Figure 40: (a-d) BFTEM images from the cross-sectional view of the substrate, CCS film and protection layer at the wafer center. (a-b) The lamella intersect reveal a triangular shape of the crystalline cone with nucleation center (red), amorphous-crystalline interface (white), and the location where the cones coalesce (blue) highlighted. (c-d) Another ROI show a parabolic shape of the crystalline cone with DPs from the crystalline (red) and amorphous (green) region included. An illustration for the cross-section of a cone (e) without and (f) with the nucleation center included. Image (e) and (f) is adapted from Miller [86]. Scale bars are 100 nm.

Orientation Relationships within the Cones

The SPED dataset raster over a larger region with a nanosized probe and collects a DP at each step. The dataset thus holds information about local variation across the scanned region, and the results from the SPED experiment is included in Figure 41. To study and visualize the evolution of the cones, the SPED dataset was cropped into seven subsets where the average DPs are presented in Figure 41 (a). They are numbered to the regions marked in the top part of Figure 41 (b). The average DP show the general structural properties, and functions as a method to study how the structure develops in the different regions of the CCS film in the presence of a cone. The c-PLD build up the structure layer-by-layer, and cropping the dataset this way, lets one evaluate how the growth changes in the different layers.

The DPs within each subset were summed up to obtain an average DP, which then show a general trend and evolution through the seven steps. The resulting seven DPs are included in Figure 41 (a). The structural development starts from a few initial crystal planes (1). Initial growth appears asymmetric in the lateral direction (2) before the crystalline regions becomes fully polycrystalline (3/4). A strong systematic row then develops (5/6/7), which is identified as the $\{110\}$ rutile planes orientated parallel to the substrate seen from the DPs from six pixels of interest in Figure 41 (c). The DPs are color coded to the location of their pixel in the top image of Figure 41 (b). They visualise the presence of a preferred stacking of $\{110\}$ rutile planes parallel to the substrate. The structure is aligned on the $[\bar{1}11]$ zone axis in three of the locations. The substrate DP is included for orientation reference in reciprocal space. The SAED pattern from conventional TEM analysis in Figure 40 (d) was also indexed on the $[\bar{1}11]$ zone axis. VBF- and VDF-TEM images are presented in Figure 41 (b) middle and bottom part, respectively. The inserted DP in the VDF-TEM image in Figure 41 (b) show the location of the virtual annular aperture. The aperture is located at the scattering angle for the first strong reflection, and integrate azimuthally the electrons scattering to this angle. The corresponding VDF-TEM image shows development of columnary growth within the cones.

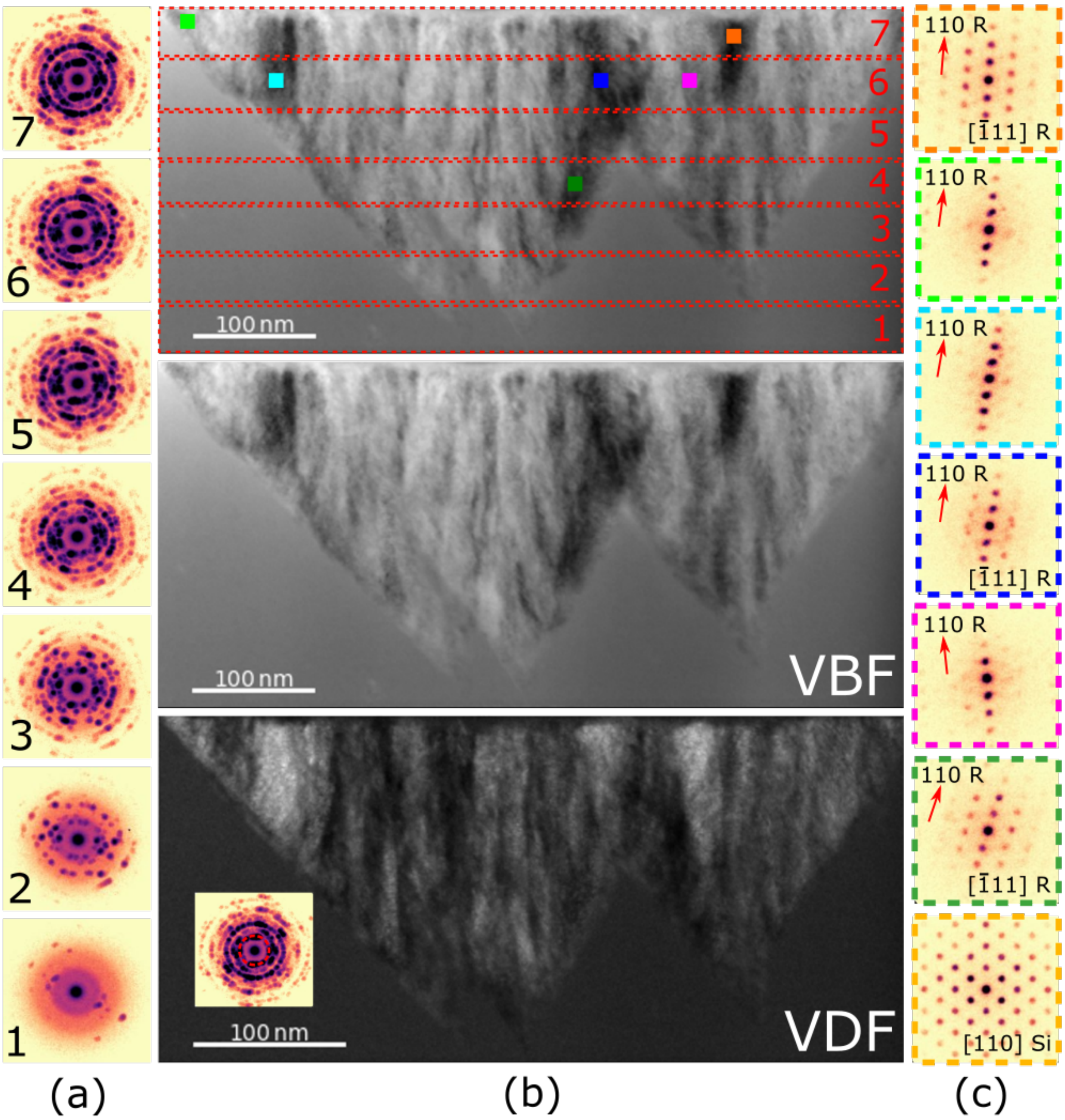

Figure 41: Results from the SPED experiment performed at the wafer center in position 0.0 cm. The lamella has intersected an inverse crystalline cone within an otherwise amorphous film. (a) Evolution of the growth of the crystalline region is visualised by the average DP from seven steps in the scanned region as visualised in the top part of the VBF-TEM image in (b). VBF- and VDF-TEM images are included in the middle and bottom part of (b), respectively. The VDF-TEM image show development of crystalline columns within the cones. (c) Six pixels which show systematic row of {110} rutile planes parallel to the substrate are included.

Initial Planes at the Nucleation Center

The nucleation centers for the cones were further studied to gain insight into the early stages of growth of the columns. In Figure 42, the DPs surrounding the three different nucleation sites of the cones were summed to study the initial atomic planes present within the crystalline regions. In Figure 42, the DPs are average DPs from the squared regions marked in the bottom of the VBF-TEM image. The d-spacings of the different reflections present are highlighted in the image, and presented in Table 4.

The reflections are located at different scattering angles, indicating that the interplanar spacings are different at the three locations. From the left, the first DP has two dominant planes, $d1 = 2.303$ Å and $d1' = 2.175$ Å. The second has one systematic row which planes are evenly spaced by d2 = 2.372 Å while the third site is spaced by d3 = 1.633 Å. All three sites contain planes initially in the vertical direction with a small tilt angle. The closest candidates are summed up in Table 4. Both anatase and rutile are potential candidates for the structure at the nucleation sites.

Table 4: Experimental d-spacings of the reflections in the summed DPs in Figure 42. The closest theoretical d-spacing are presented for rutile and anatase. Theoretical values taken from Recipro [79].

Indexation of DP1		
d-spacing	Anatase	Rutile
d1 = 2.303 Å	$d_{110,112,021,201} = 2.332$ Å	$d_{200,020} = 2.297$ Å
d1' = 2.175 Å	$d_{110,112,021,201} = 2.332$ Å	$d_{111} = 2.187$ Å
d2 = 2.372 Å	$d_{004} = 2.337$ Å	$d_{200,020} = 2.297$ Å
d3 = 1.633 Å	$d_{012,102,121,211} = 1.666$ Å	$d_{220} = 1.624$ Å

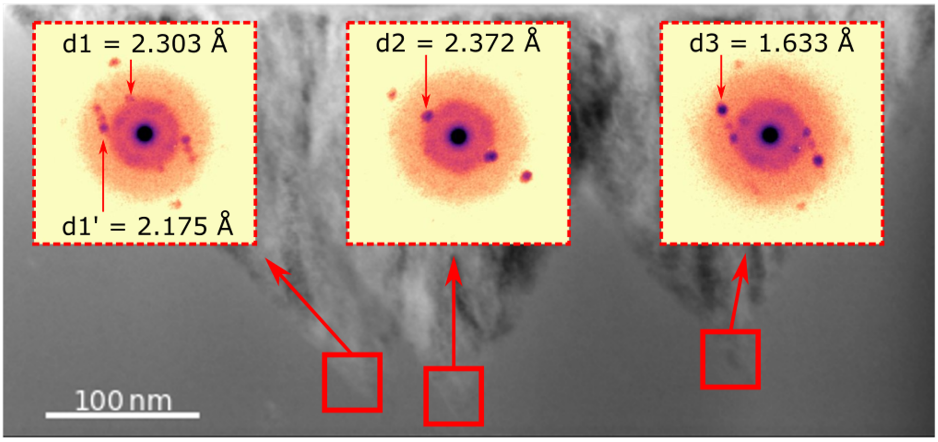

Figure 42: Summed DPs at the nucleation center of the cones were obtained to study the early stages of growth of the cones. See corresponding section for further description.

SAED and DFTEM was performed at the same cones present in the SPED results in Figure 41. The conventional TEM results can be revisited in the light of the SPED results. Figure 43 presents a DFTEM image from the merged signal of the reflections within the objective apertures marked in the inserted DP. The top reflection (cyan) was chosen to evaluate the presence of the preferred {110} planes parallel to the substrate. The encapsulated reflection has a d-spacing of 1.667 Å which corresponds to the {110} planes of the rutile structure. Columnary growth are present in the conventional DFTEM image in Figure 43 as in the VDF-TEM image in Figure 41, where the large column in the top left of the two images is the clearest common feature. The second aperture was placed in the lateral direction to encapsulate two reflections. The signal (magenta) primarily occupies other regions than the signal from the {110} reflection in Figure 40. All nucleation centers appear to be dominated by the signal from the objective aperture placed in the lateral direction.

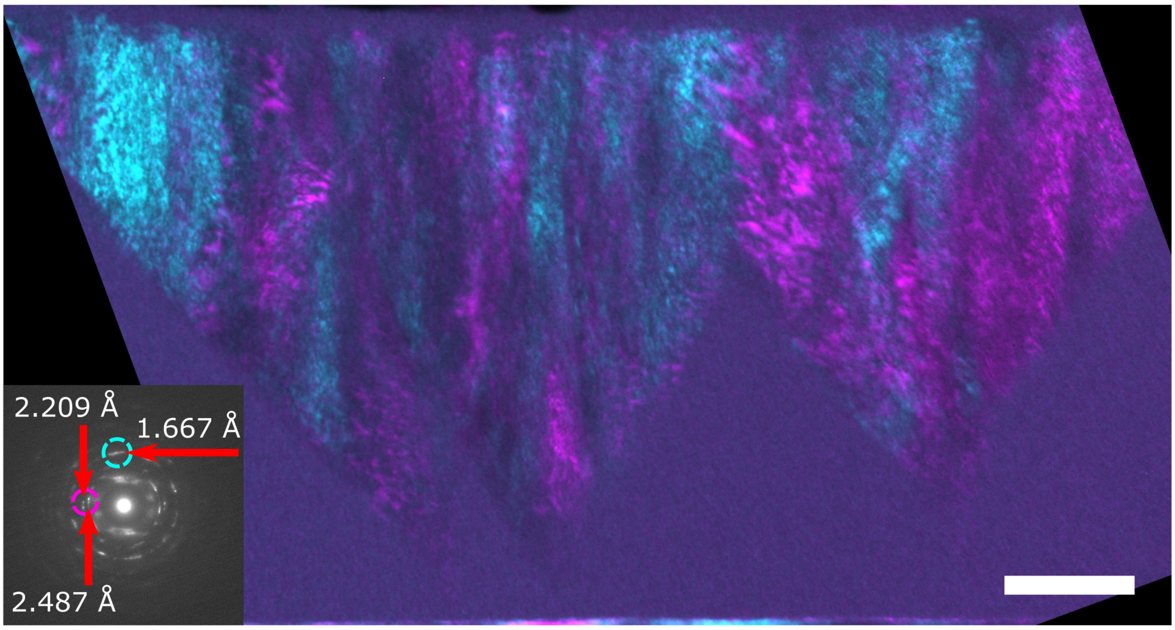

Figure 43: DFTEM image from the lamellae at the wafer center in position 0.0 cm with the corresponding SAED pattern inserted. The color of the objective aperture is coded to the color of the signal in the DFTEM image. The crystalline features within the inverse cones show similar results as from the SPED analysis. See section for further description. Scale bar is 100 nm.

Growth Modes in the Inverse Cones

The presence of inverse crystalline cones within an amorphous region is a characteristic feature for zone I in the model presented in section 2.4.2 [47, 50]. Here, quench growth with negligible surface diffusion is dominant, and leads to an amorphous structure. If nucleation of a nanoparticle occurs, then a competition between the amorphous and crystalline regions develop as a result of altered surface mobility that results in the inverse crystalline cones [51].

The growth of the inverse crystalline cones is an example visualizing the importance of the energy landscape for the adatoms. For the results at the wafer center in Figure 41, the doping concentration and the deposition parameters are equivalent for the deposition which leads to both the amorphous and crystalline regions. In the VDF-TEM image in Figure 41 (b), columnary growth develops when the atoms are deposited on the crystalline regions of the inverse cones, while the structural properties remains amorphous in the amorphous regions. Local variations of the surfaces can thus have great influence on the structural properties after film growth.

From the results presented in Figure 42, the evolution of these cones appears to start with initial growth in the lateral direction. At the three different nucleation centers, the d-spacing of the planes vary as seen in Table 4. Both anatase and rutile have planes which d-spacings are good candidates for the different crystalline regions present. Based on these results there do not appear to be any preferable initial d-spacing, and one cannot further conclude with certainty what is the predominant phase presence.

As growth continuous, the seven step evolution presented in Figure 41 shows how the structure becomes polycrystalline with a few columns with the {110} rutile planes orientated parallel to the substrate when the substrate is aligned on the [110] zone axis. The {110} facet holds the lowest surface free energy of the low-indexed facets of the rutile structure as seen in Table 1 in section 2.4.2. Surfaces with higher energies are thus orientated in the lateral direction in these columns. The large column orientated with the {110} planes vertically in the top left part of Figure 43, initially grows from the interface. At the interface, the competition between the amorphous and crystalline region takes place, while within the cone, the competition is between neighbouring columns. The interface may play a role in the development of the stacking of {110} parallel to the substrate.

To summarize, the cones at the wafer center show the importance of the energy landscape, and how variations in the local growth conditions can have a great influence on the final film structure. Additionally, the crystalline growth is faster than the amorphous within this region, but nucleation of an initial crystalline region is a rare event.

4.5 Quenched Growth Past Wafer Center

Conventional TEM was performed at the intermediate step between the wafer and second plume center in position 0.75 cm. In Figure 44 (a), the BFTEM image shows no intensity variations in the CCS film. The corresponding DP in Figure 44 (b) from the selected aperture marked in the BFTEM image, shows diffuse scattered signal from the diffracting volume. The combination of the two results indicates an amorphous structure at this location in the CCS film. An objective aperture was placed at an arbitrary position in the diffuse scattered region to obtain a DFTEM image for consistency with the rest of the results of the thesis. In Figure 44 (c), the DFTEM image is presented and further support the statement that the structure is amorphous as there are no sign of crystalline regions.

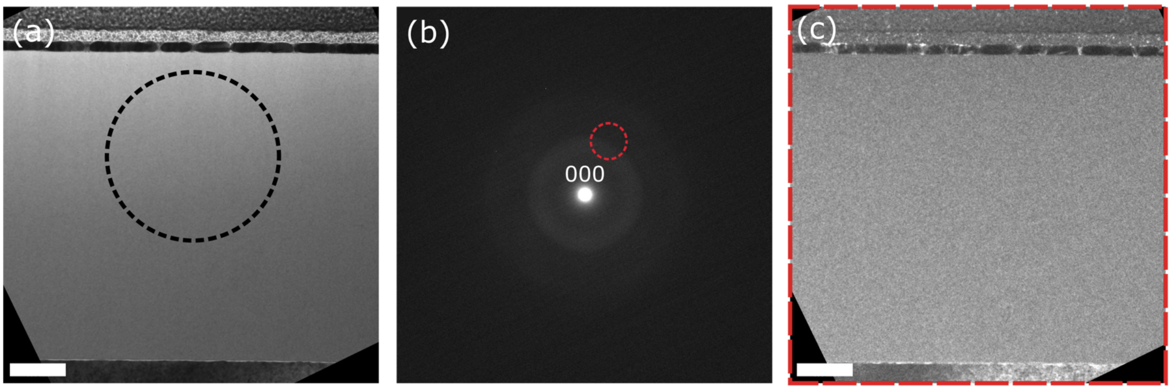

Figure 44: (a) BFTEM image of the cross-sectional view of the substrate, CCS film and protection layer from the lamella in position 0.75 cm. The approximate size and location of the selected area aperture are visualised by the dashed dark circle for the corresponding (b) DP. The red dashed circle indicates the approximate size and location of the objective aperture used to obtain the (c) DFTEM image. Scale bars are 100 nm.

Growth Modes in the Quenched Growth

The conventional TEM results presented in Figure 44 show an amorphous film with no sign of crystalline regions. The characteristic feature for zone I in the model presented in section 2.4.2 is an amorphous structure. The growth in this zone is quenched as surface diffusion is negligible, which means that the atoms more-or-less deposits where they land. The growth modes at position 0.75 cm can thus be described by the processes in zone 1 of the presented model. One of the deposition parameters thus appears to prohibit surface diffusion, or destabilize the structure. The influence of the doping concentration and the different deposition parameters was discussed in section 4.1.

4.6 Nanocrystalline Columns at Second Plume

As shown in Figure 27 in section 4.1, nanocrystalline columns develop after an initial amorphous region at the second plume center in position 1.25 cm. The nanocrystalline columns appear to be sensitive to the thickness of the CCS film, and the position in relation to the second plume center. In addition to conventional TEM techniques, a SPED experiment was performed at the second plume center. The use of the nanosized probe in the SPED experiment provide DP from a smaller region which lets one study the columns in greater detail. Additionally, a SPED experiment scans over an area such that one can study a number of the columns.

In Figure 45 (a), the DP of the CCS film shows both distinct reflections and diffuse scattered regions, indicating the presence of crystalline and amorphous structures, respectively. The pattern has a few distinct reflections in the lateral direction located at an equivalent scattering angle, but which vary azimuthally. In Figure 45 (b), a DFTEM image is presented from the objective aperture marked in Figure 45 (a). The scattered region shows that nanocrystalline columns appear in the upper part of the CCS film, and the angular spread in the DP indicate a mosaic spread of the columns. Further DFTEM images at this location is included in Figure A2 of the Appendix A.

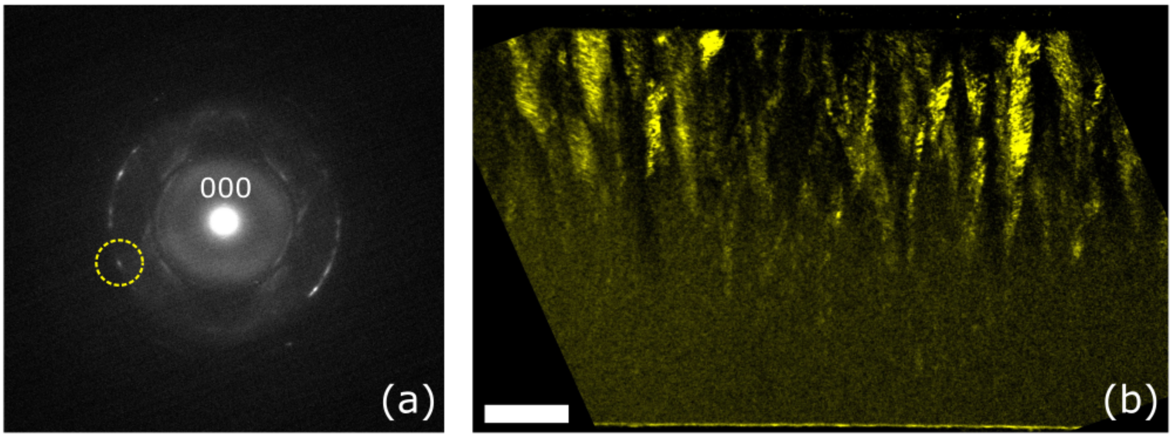

Figure 45: Conventional TEM results from the second plume center position 1.25 cm. (a) SAED pattern from the CCS film with highlighted objective aperture for the corresponding (b) DFTEM image. Scale bar is 100 nm.

Phase Identification of the Nanocrystalline Columns

Results from the SPED dataset of the CCS film is presented in Figure 46. The DPs for the whole set were summed together in Figure 46 (a), and the virtual annular apertures are shown and color coded to the corresponding VADF-TEM images in 46 (b) and (c). Similarly to the cones at the wafer center in section 4.4, the dataset was cropped into seven subsets to show the evolution of the average structure as the CCS film thickness increases. The different sets are shown by the dashed lines in the VADF-TEM images. The region at the bottom is assigned to DP 1, and the top to DP 7. The DPs in each subset was summed up, and is presented in Figure 46 (d), where the DP of the substrate is included for orientation reference in recirpocal space.

The film growth across the seven subsets reveals that the structure develops from an amorphous region at the bottom, to a polycrystalline at the top. The structure is amorphous in (1) as seen by the absence of any reflections in the DP in Figure 46 (d). A set of strong reflections develops in the lateral direction as seen in (2) in addition to non-uniformity within the diffuse scattered region. The features indicate that larger ordered regions are forming, and they become stronger as more material have been deposited in step (3) and (4). There are additionally a further spread of the reflections azimuthally, which indicate tilt variations of the crystalline regions. Stronger reflections then appear at lowering scattering angles (5/6/7).

The VADF-TEM images in Figure 46 (b) and (c) are color coded to the annular aperture shown in Figure 46 (a). In Figure 46 (b), the annular aperture is placed at an equivalent scattering angle to the strong reflections in the lateral direction seen in Figure 46 (d). The annular aperture also include the same scattering angle where the objective aperture was placed in Figure 45 (a). In Figure 46 (b), the nanocrystalline columns are present, and appear to form earlier during film growth than indicated in Figure 45.

DPs from single pixels with the strongest signal are included, where the red lines indicate the area where they are taken from. In the bottom part of the CCS film, the two lowest DPs in Figure 46 (b), show distinct reflections in the lateral direction. The d-spacing for the crystalline planes within the diffracting volumes are 1.430 and 1.446 Å. The reflections are absent in the first step (1) in Figure 46 (d), but appear in the second. As more material is deposited and the CCS film thickness increases, they develop into larger columns with further features present in their DPs as seen in Figure 46 (b). DP1 and DP2 marked in Figure 46 (b) are obtained from columns which develop from the initial set of planes in the lateral direction. They are further presented in Figure 47 (a) and (b), respectively. The DP1 can be indexed to be <221> zone axis for anatase and <135> zone axis for rutile, while DP2 can be indexed as <001> zone axis for anatase and <123> zone axis for rutile. Their simulated DP are presented in Figure 47 (b-c) and (e-f) for anatase and rutile, respecitvely. The experimentally measured and theoretical d-spacings are presented in Table 5. The phase present is further discussed in the following section.

In Figure 46 (c), the VADF-TEM from the lower scattering angle also show columnary growth, but the columns develop later as the CCS film thickness increases. Multiple DPs from these columns are identified as the rutile <101> with the {100} equivalent planes orientated close to the vertical direction. One can thus conclude that rutile is present at this location.

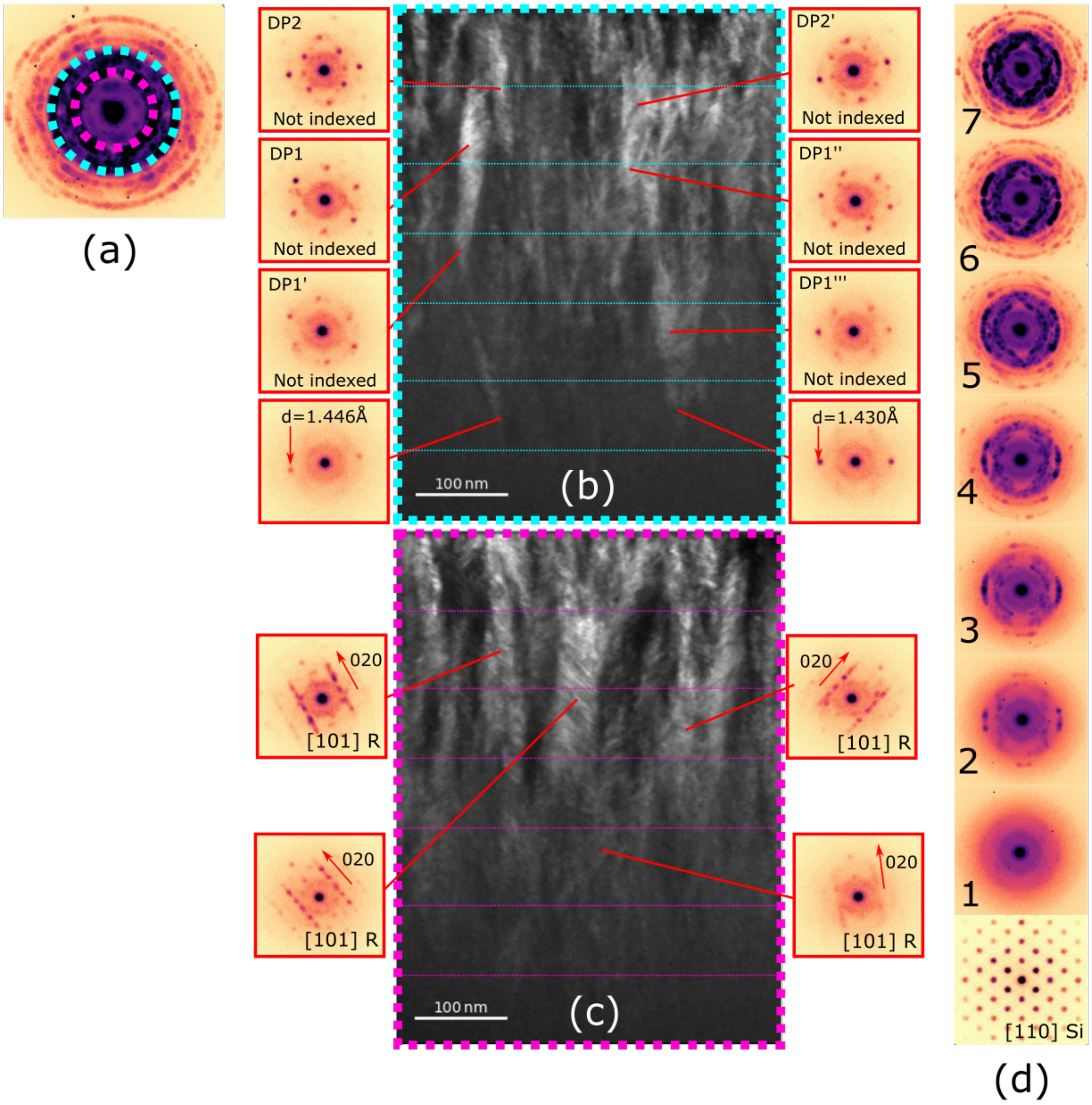

Figure 46: SPED results from the second plume center in position 1.25 cm. (a) Summed DP from the CCS film with virtual apertures shown and color coded to the (b/c) VADF-TEM images. The scattered regions reveal the presence of columnary growth where DPs from pixels with the strongest signal are included. The set was cropped into seven parts, and (d) the summed DP for each region is shown together with the substrate for orientation reference in reciprocal space. The different regions are indicated by dashed line in the VADF-TEM images.

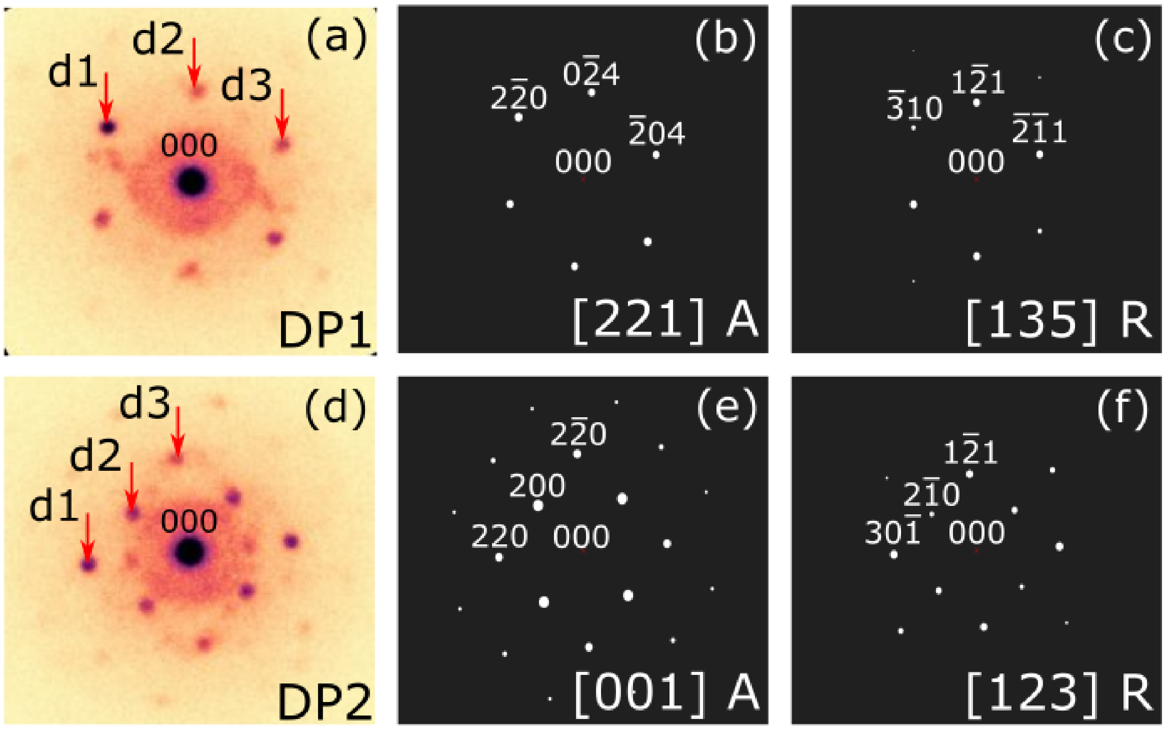

Figure 47: Two (a/d) DPs from the SPED dataset at position 1.25 cm are attempted indexed. Both anatase and rutile contains potential candidates for the phase present. Simulated DPs are presented in (b) and (c), and in (e) and (f) for anatase and rutile, respectively [79]. See section for further details.

Table 5: Experimental and theoretical d-spacings for the potential candidates of the anatase and rutile structures of the nanocrystalline columns at the second plume center.

Indexation of DP1

DP	Anatase [221]	Δ	Rutile [135]	Δ
d1 = 1.426 Å	d_{220} = 1.338 Å	-0.088 Å	d_{310} = 1.456 Å	+0.030 Å
d2 = 1.484 Å	d_{024} = 1.481 Å	-0.003 Å	d_{121} = 1.687 Å	+0.203 Å
d3 = 1.515 Å	d_{204} = 1.481 Å	+0.034 Å	d_{211} = 1.687 Å	+0.172 Å

Indexation of DP2

DP	Anatase [001]	Δ	Rutile [123]	Δ
d1 = 1.430 Å	d_{220} = 1.338 Å	-0.092 Å	d_{301} = 1.360 Å	-0.070 Å
d2 = 1.990 Å	d_{200} = 1.892 Å	-0.098 Å	d_{210} = 2.054 Å	+0.064 Å
d3 = 1.437 Å	d_{220} = 1.338 Å	-0.099 Å	d_{121} = 1.687 Å	+0.250 Å

Nanocrystalline Features Past Plume Center

As seen in Figure 26 (h) and (o) in section 4.1, the nanocrystalline features are also present past the second plume center in position 1.75 cm. Conventional TEM was performed at this location, and the results are presented in Figure 48. In Figure 48 (a), the BFTEM image shows the cross-sectional view of the substrate, CCS film and the protection layer. The corresponding DP from the CCS film in Figure 48 (b) show a mixture of distinct reflections and diffuse scattered regions similar to the DP at the second plume center in Figure 45 (a). The strong reflections in the lateral direction are highlighted in Figure 48 (c). The electrons scatter of crystalline planes which are spaced by 1.458 Å, and in the perpendicular direction in relation to the substrate surface. In Figure 48 (d), the DP from the substrate shows orientation reference in reciprocal space. In the light of the results in Figure 46 (c), similarities to the rutile <101> orientated structure can be identified in the DP in Figure 48 (b) as shown by the dots in Figure 48 (e). In Figure 48 (e), the d-spacing to the second reflection parallel to the substrate is 1.176 Å, which can potentially be assigned to the {400} planes in the rutile structure.

In Figure 48, a merged DFTEM image from the two objective apertures shown in Figure 48 (c) and (e), is presented. The growth of nanocrystalline columns can be identified in the DFTEM image after an initial region of amorphous or nanocrystalline grains. Three regions are highlighted in Figure 48 (g). The first region (I) contains structural properties which is either amorphous or nanocrystalline. A few nanocrystalline columns start to grow in the second region (II) where signal is strongest from the reflection in Figure 48 (c). The third region (II) consists of nanocrystalline columns which are densely packed compared to the previous region. The change in growth mode as a function of the thickness of the CCS film will be discussed in the following section.

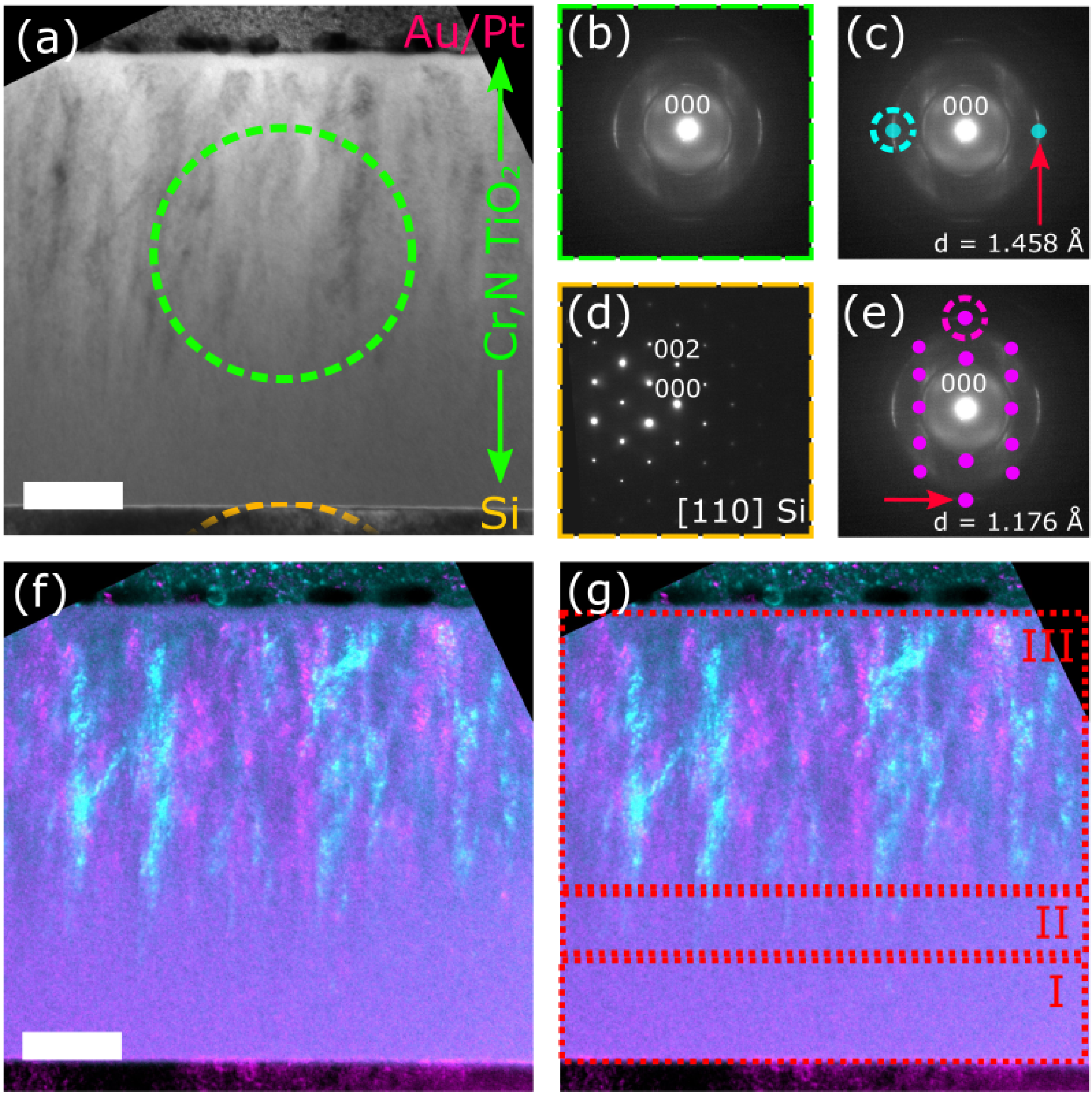

Figure 48: (a) BFTEM image from the cross-sectional view of the substrate, CCS film and protection layer at position 1.75 cm. (b) DP from the CCS film shows (c) distinct reflection in the lateral direction which is broadened azimuthally. (d) The DP of the substrate shows orientation reference in reciprocal space. (e) Similar features to the <101> rutile zone axis can be identified in the DP. (f) DFTEM image of the two objective apertures marked in (c) and (e) with (g) highlighted regions of different growth. See section 4.6 for further description. Scale bars are 100 nm.

Growth Modes and Structural Properties at the Second Plume Center

The results in Figure 48 and 46 from the second plume center (position 1.25 cm) and past it (position 1.75 cm), respectively, show a mixture between amorphous and nanocrystalline structural properties. The three separate regions highlighted in Figure 48 (g) visualise how the growth conditions vary as a function of the CCS film thickness. The amorphous structure in region I, and the nanocrystalline columns in region III, are characteristic features for zone I and zone T in the model presented in section 2.4.2, respectively. The surface diffusion is negligible in zone I, and starts to dominate in zone T. The growth conditions thus appear to vary as the thickness of the CCS film increases.

At the two positions, the doping concentration and the other deposition parameters are equivalent during deposition. There thus appears to be another variable which changes the growth conditions. In region II marked in Figure 48 (g), a few nanocrystalline columns have developed. The surface mobility would be altered for the following adatoms sticking to these surfaces, and thus the surface diffusion distance. The increased surface mobility is a potential explanation for why the growth conditions changes as a function of the film thickness. The results from the inverse crystalline cones at the wafer center in section 4.4, also illustrate how deposition on amorphous and crystalline areas can result in different structural development. The results of section 4.4 also visualize how crystalline regions overturn amorphous as the thickness increases.

The result of the perpendicular series in Figure 27 also indicates a thickness dependence. The column grow later in the growth process at the intermediate location compared to the second plume center in Figure 27 (f) and (i), respectively. The CCS film studied in this thesis is ∼600 nm thick. One might speculate how the film structure would appear if one would grow a 800 nm or 1 μm thick film as the columns would continue to compete. Conversely, if one would grow a thinner CCS film, for example below ∼ 250 nm, then the nanocrystalline columns would be absent even at the second plume center in position 1.25 cm.

The results from the SPED experiment in Figure 46 provided further insight into the phases present in the nanocrystalline regions. In Figure 46 (c), a few columns is identified as the rutile <101> orientated with the {020} planes stacked at different tilt angles parallel to the substrate. The rutile phase is thus present at the second plume center (position 1.25 cm). However, it appears to be dominant in the later stages of growth as seen in Figure 46 (c).

In Figure 46 (b), another structure is identified, and it has not been indexed due to potential candidates of both the anatase and rutile structure based on the measured d-spacings presented in Table 5, and symmetry of the DPs in Figure 47. The common feature between the two rutile candidates <135> and <123> in Figure 47 (c) and (f), respectively, is that their {121} planes are orientated parallel to the substrate. In Figure 46 (b), the columns appear to develop from a set of crystal planes orientated perpendicularly to the substrate. $d1$ in both D1 and D2 in Figure 47 (a) and (d), correspond to the reflection for these planes. $d1$ is assigned to the $(\bar{3}10)$ and $(30\bar{1})$ reflection at the <135> and <123> zone axis, respectively. The two candidates thus differ for the indexation of this reflection.

The anatase candidates for the not-indexed structure are the <221> and <001> orientations for DP1 and DP2, respectively. Their simulated DP are presented in Figure 47 (b) and (e), respectively. The common feature for the two candidates is that $d1$ is indexed to same set of planes. The {220} planes is assigned to $d1$ in both structures. From the results presented in section 4.3, the anatase structure was found locally within the CCS film with the {220} planes orientated perpendicular to the substrate. As presented in Table 1, the anatase facet corresponding to these planes holds the highest surface free energy, and is thus highly reactive. Previous results presented in section 4.2 and 4.4, show the importance of high growth rates in the lateral direction. The anatase candidate support this trend for growth in the CCS film. Additionally, the anatase phase holds a lower surface free energy than rutile and can thus be preferential on the nanoscale [17], where the kinetic energy transition from amorphous TiO_2 is lower for the formation of anatase than rutile at the nanoscale [60].

The non-indexed structure thus holds candidates which can be assigned to both the rutile and the anatase phase. Based on the analysis, one cannot identify with great certainty which of the candidates are present. However, based on the results at other locations within the film and properties of TiO_2 found in other work, anatase appears as the most likely candidate.

4.7 Electron PDF Method to Study Amorphous and Nanocrystalline Regions

The amorphous and nanocrystalline regions at the second plume center in position 1.25 cm motivated use of electron PDF to study these regions in greater detail. Specifically close to the nucleation centers, it would have been interesting to study any structural variations between the amorphous and nanocrystalline regions to better understand the growth modes.

PDF Method on Amorphous SiO_2 Layers

An amorphous region in a multipurpose SPED dataset from a CPU sample was used as proof of principle for combining SPED, PDF and BSS algorithms. The author was informed that this region had two distinct layers of different amorphous SiO_2 *phases, and the data analysis was performed accordingly. Two days prior to the thesis deadline, it turned out that this was the wrong chemical composition. The layers are experimentally verified to consist of* Si_3N_4*, and not* SiO_2*. The results and analysis were thus performed as if the amorphous region is* SiO_2 *and not* Si_3N_4*. Due to the limited time, the results section is left untouched, but the method will be discussed in the light of the new information.*

To obtain a proof of principle, the electron PDF method was tested on a multi-purpose SPED dataset of a CPU. The SPED dataset was obtained by Emil Frang Christiansen at the Department of Physics, NTNU. Figure 49 presents a VBF-TEM image of the CPU, where the amorphous SiO_2 layer is highlighted by the red arrows. A ROI marked with a dashed green rectangle, was cropped and used for further analysis. The region from the CPU will now be analyzed more in details, utilizing the methods in machine learning together with PDF as described in section 2.2.2 and 2.3, respectively.

Two different amorphous phases are present within the layer as seen by the intensity difference of the VADF-TEM images at different scattering angles in Figure 50 (a) and (b). The virtual annular aperture is visualised for the two images in Figure 50 (c) and (d), respectively, and the DP here is the summed signal from the layers marked in Figure 50 (a) and (b). The average PDF and DP from the bottom and top layer are presented in Figure 50 (e) and (f), respectively. Both the DPs and PDFs differ in their appearance, and indicate structural variations between the two amorphous SiO_2 layers.

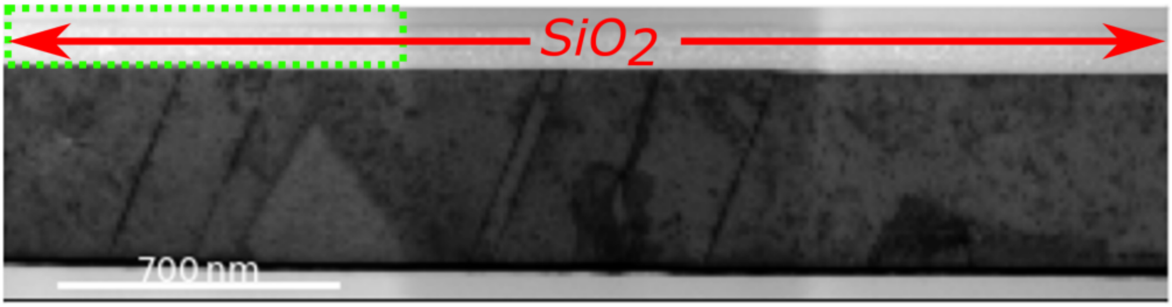

Figure 49: VBF-TEM image of the CPU sample. The amorphous SiO_2 is highlighted in the top part of the image. The green dashed rectangle marks the region which was further analyzed. See section for a further presentation of the results.

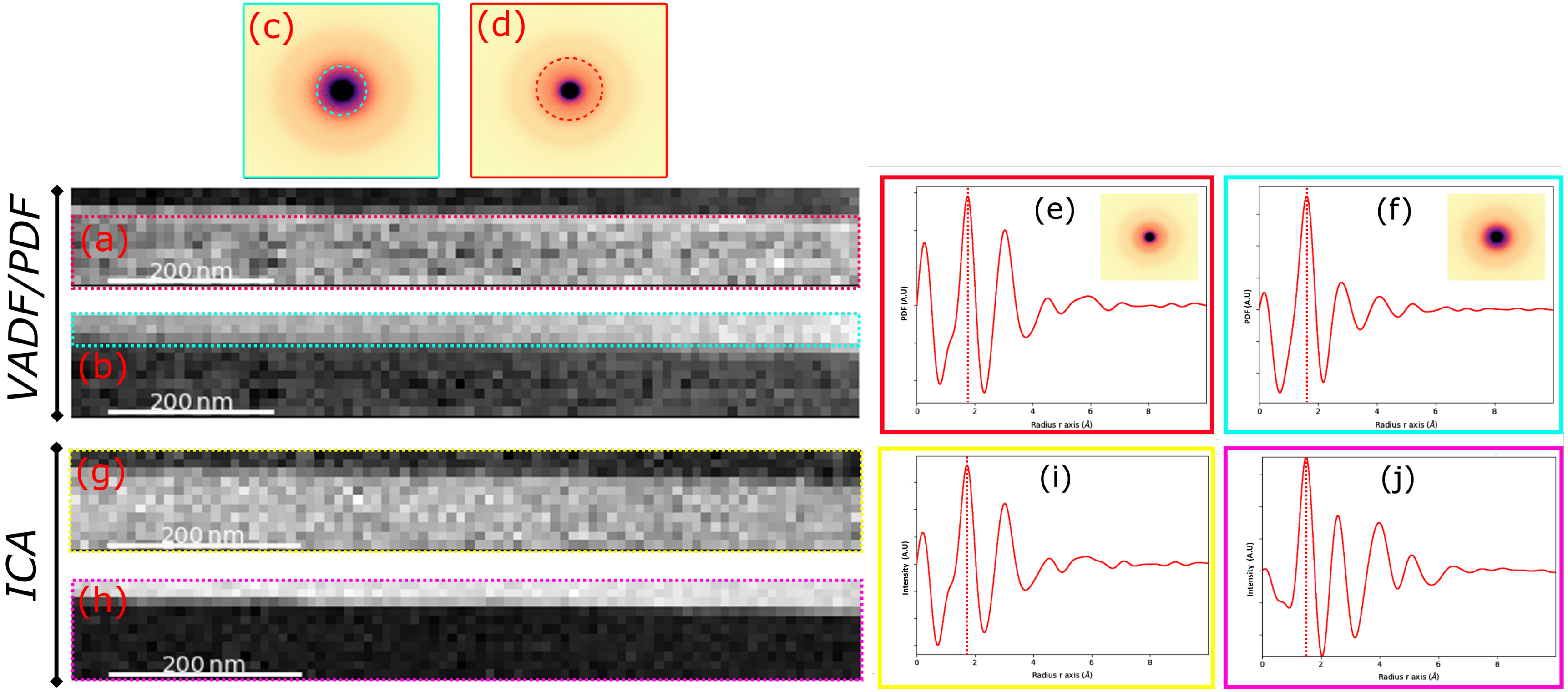

Figure 50: The (a) bottom and (b) top part of the amorphous SiO_2 layer show intensity variations in the VADF-TEM images at different scattering angles as marked in (c) and (d), respectively. The average PDFs and DPs in (e) and (f) are color coded to the bottom and top layer. The (g/h) loading map and the (i/j) components from the ICA decomposition appear equivalent to the VADF-TEM and PDF counterparts. The red dashed line marks the position of the first pair distance in the PDFs and ICA components. See section 4.7 for further presentation.

The cropped dataset was then de-whitened by the use of the SVD algorithm, and the corresponding scree plot is presented in Figure 51. The plot visualizes the variance in the set as a function of index number on a logarithmic scale. It is used as an indicator for the number of physical components present in the set by assuming that noise decreases exponentially with component index [26]. Noise and uncorrelated components thus follow a linear trend in this plot, and the number of components above the linear trend indicates the number of physical components. The location of the elbow indicates the presence of three principal components, which are uncorrelated and not dominated by noise. The third component shows a variance on the order of 10^{-3} in the set, and is thus expected not to be a dominant feature. The two first components are therefore analyzed further while the third component is included in the Appendix.

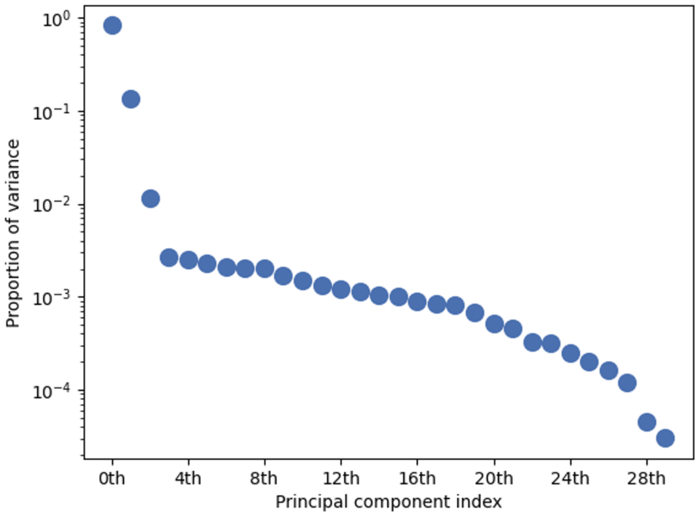

Figure 51: Scree plot showing proportion of variance as a function of component index on a logarithmic scale from the SVD whitening of the CPU practice set.

The loading map of the first and second component is presented in Figure 50 (g) and (h), respectively. The distribution of the components appears similar to the VADF-TEM images of the bottom and top layer in Figure 50 (a) and (b), respectively. The first and second components of the ICA decomposition are presented in Figure 50 (i) and (j), respectively, and appear similar to the average PDFs of the bottom and top layer in Figure 50 (e) and (f), respectively. The agreement between the components and their loading maps with the experiments with physical meaning, indicates that the ICA algorithm is providing physical results.

The different polyamorphous structures of SiO_2 was introduced in section 2.3, and SiO_2 commonly either structure in disordered chains of tetrahedrals (SiO_4) or octahedrals (SiO_6) where this is assigned to cristobalite- and coesite-like or stishovite-like structures, respectively [69]. The first bond distance in these structures correspond to the first Si-O pair distance. The bond distance vary in a tetaherdral arranged structure between 1.55 to 1.61 Å, depending on which of the phases are presence [42]. For an octahedral arrangement, the first Si-O bond length shifts to 1.77 Å in a stishovite-like arrangement [42]. The value are presented in Table 6.

The Si-O bond distance correspond to the first pair distance in the average PDF from the two layers. The distance was measured to be 1.60 ± 0.02 Å and 1.75 ± 0.02 Å for the PDF of the bottom and top layer seen in Figure 50 (f) and (g), respectively. There thus appear to be a shift in the first Si-O pair distance between the two layers.

The agreement in appearance between the ICA components and loading maps with the VADF-TEM images and average PDFs, respectively, indicates that the components resembles PDFs, and contain similar physical information about the structure. The position of the peaks thus provides insight into pair distances in the structure. The position of the first peak in the first and second component was measured to be 1.59 Å and 1.75 Å, respectively. The loading map of these components thus indicate where in the set these features are presence.

Table 6: Theoretical Si-O bond lengths for a tetragonal and octahedral arrangement in amorphous SiO_2 structures are presented. Theoretical values taken from Volceanov [42] where the values for tetragonal arrangement correspond to cristobalite- and coestie-like amorphous SiO_2 structure while octahedral for a stishovite-like. The location of the first peak in the experimental average PDFs and the ICA components are presented.

Pair Distance [Å]						
	Theoretical		Experimental		ICA comp.	
Atom Pair	Tetrahedral	Octahedal	Avg. bottom	Avg. top	1st	2nd
Si-O	1.55-1.61 Å	1.77 Å	1.60 ± 0.02 Å	1.75 ± 0.02 Å	1.59 Å	1.75 Å

A difference between the structures in the two layers is thus assigned to the shift in the first Si-O pair distance from 1.60 ± 0.02 Å to 1.75 ± 0.02 Å in the experimental average PDFs. The shift is in good agreement with a shift from a tetrahedral (SiO_4) arrangement to an octahedral (SiO_6) arrangement of O atoms based on the theoretical values presented in Table 6. The ICA decomposition is successful in detecting this variation between the components and their distribution in the dataset.

Evaluation of the Electron PDF Method

As the chemical composition in the layer marked as SiO_2 in Figure 49 was in fact Si_3N_4, the interpretation and parts of the analysis is done without the correct information. However, there are still valuable findings and lessons worth documenting for developing the method. The change in chemical composition is expected to influence the results in two ways: subtraction of the background by the independent atom approximation, and interpretation of the results by matching peaks to pair distances.

In Figure 52 (e) and (f), the background subtraction resulted in interpretable average PDFs even though the chemical composition was technically wrong. The Si_3N_4 would result in similar average atomic form factors to SiO_2. N has a lower atomic number than O, and electrons would thus scatter less of these atoms, which would alter the shape of the average atomic form factor. However, Si_3N_4 has a relative higher Si content than SiO_2 as the ratio between Si and N could also be written as $SiN_{1.25}$. The similarities between the average atomic form factor may explain why the background substraction provided interpretable PDFs.

The background has thus been subtracted without physical meaning, but yielded interpreatable results for the decomposition algorithm. The VADF-TEM images in Figure 50 reveal the presence of two different amorphous phases within the Si_3N_4 layer. The agreement between the loading maps in Figure 50 (g) and (h) to the VADF-TEM images in Figure 50 (a) and (b), respectively, show that the decomposition by the ICA algorithm are able to separate out the two independent sources in the dataset with the preprocessing steps performed. An important finding from the results of the decomposition of the CPU sample is thus that the ICA algorithm is suitable for decomposition of a PDF-SPED datacube. The ICA algorithm has also been successful in similar work when studying amorphous materials [26]. However, a note is that improper background subtraction can lead to artifacts in the PDF showing up as ripples due to the fourier transform of the total scattered signal. Figure A3 included in the Appendix A show artifacts in single pixels within the layers compared to the average PDF of the layers.

The presence of Si_3N_4 within the layer makes the interpretation of the results wrong as the first peak does not correspond to the first Si-O pair distance, but rather the first Si-N distance. O and N are neighbours in the periodic table, and are thus similar in nature. For simulated bond pair distances in $SiN_{1.33}$ [87], the first Si-N pair distance is found to be 1.73 Å, which is similar to the Si-O bond length of 1.77 Å in an octahedral arranged SiO_2 structure [42]. The similarities between the two compositions are expected to contribute to the fact that the difference went unnoticed.

The second plume center in the CCS film was studied by a SPED experiment, and the results were presented in Figure 46. Figure 52 (a) is a magnified image of the bottom two subsets of Figure 46 (b), while Figure 52 (b) is the bottom two subsets of Figure 46 (b). The results presented in Figure 52 reveal that the bottom region is far more complex than random disorder. The intensity variations in the VADF-TEM images reveal that there are clusters of nanocrystalline regions that scatter to different scattering angles. The inserted DPs from two regions of strong scattering are included.

The results from the analysis of the Si_3N_4 layers also reveal the importance of a chemical map when interpreting the physical meaning of the PDFs. In the CCS film, the TiO_2 structure is doped with Cr and N atoms which are similar to Ti and O, respectively. In Figure 52, the amorphous phases are more intermixed than in the CPU practice set. A chemical map would thus provided further information to relate the atomic pair distances to potential clusters of different composition on the nanoscale. A chemical map with good resolution is thus considered necessary based on the findings of this thesis to obtain physical meaningful information when combining PDF, SPED and BSS algorithms.

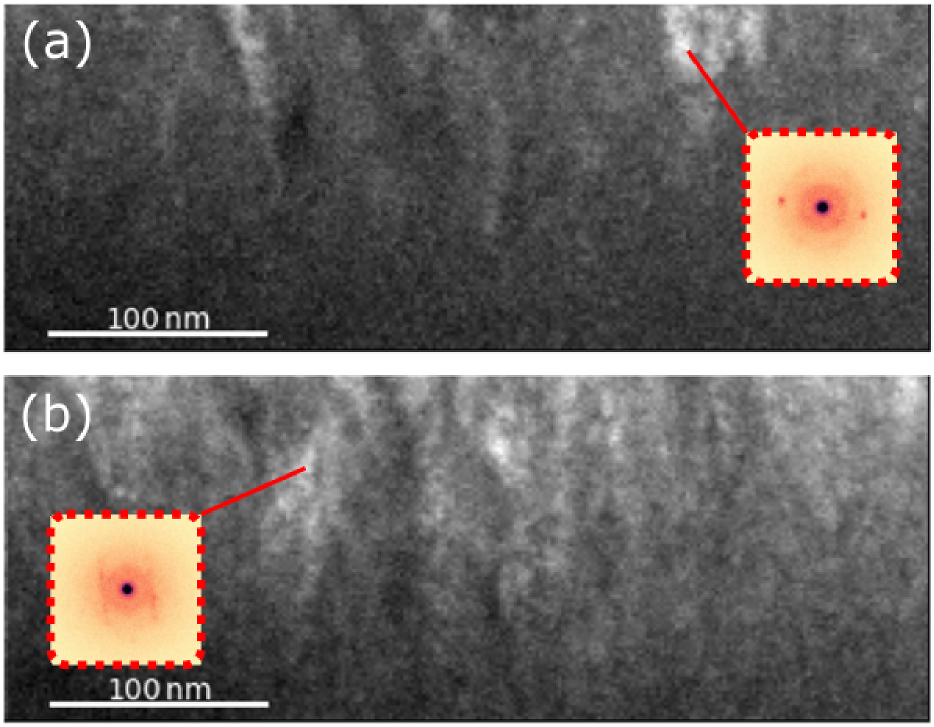

Figure 52: (a/b) VADF-TEM images from the SPED obtained from the second plume center position 1.25 cm with inserted DP from regions of strong scattering. See section for a presentation of the results.

5 Conclusion

The thesis work has consisted of a TEM study of two series of cross-sectional lamellae prepared by FIB from a Cr,N codoped TiO_2 CCS film grown by c-PLD. The structural properties varies continuously across the CCS film, and one can conclude that the TEM is an effective technique to detect results of local variations of the growth conditions.

From the series parallel to the wafer center line, one can make the following conclusions: as the structure first goes from polycrystalline to amorphous towards the wafer center, the energy barrier for crystal growth increases. The thickness of the capping layer, the Cr and N content and utilization of the flank of the plumes are candidates which are expected to contribute to this trend. For the polycrystalline regions around the first plume center (in position -1.75 cm, -1.25 cm and -0.75 cm), surface diffusion is the dominant process according to the zone model presented in this thesis. The rutile phase is dominant, even though anatase is found locally. The results show that facets with lower surface free energies, such as the {100} and {110} rutile planes, are stacked parallel to the substrate while higher energy surfaces are orientated in the perpendicular direction. HRTEM results show that the stacking occur close to the substrate, and one can conclude that the preferred orientation occurs initially and is not a result of evolutionary selection.

At the wafer center and past it (in position 0.0 cmand 0.75 cm), the growth mode is quenched where the structure is amorphous with growth of inverse crystalline cones. Within the cones, columnary growth is present. A few columns which develop at the interface prefer the {110} rutile planes parallel to the substrate. One can conclude that the energy landscape is important for the growth in the later stages by the presence of the crystalline cones.

At the second plume center (in position 1.25 cm and 1.75 cm) and from the perpendicular series, one can conclude that the growth of the nanocrystalline columns are sensitive to the position in relation to the plume center and the thickness of the CCS film. One can further conclude that rutile is present in addition to a structure which is not identified. The latter grow initially in the lateral direction, and appears to be important for the change of growth conditions as a function of CCS film thickness.

The methodology of TEM and PDF analysis has been evaluated and tested to study the amorphous and nanocrystalline regions at the second plume center (in position 1.25 cm). Method by combining PDF, SPED and BSS algorithm shows potential in detecting atomic scale variations, but further work is necessary before it can be used at the second plume center.

6 Future Work

The number of deposition parameters in PLD is large, and there are thus a great number of routes for future work to better understand the growth mechanisms. A similar TEM study could be performed on CCS film grown with other deposition parameters to compare the results to the findings of this thesis. The Solar Cell Physics group has grown an identical CCS film on a LAO substrate. A similar study could be performed to study the influence of substrate choice by comparing the structure and growth modes to the results at the different locations of the CCS film studied in this thesis. Additionally, it is common procedure to anneal the film after deposition by PLD to assure crystal growth. A similar study could be performed on a film after annealing to understand the growth modes when the melting temperature is reached. Further details on these growth modes could potentially be obtained by performing an *in situ* experiment where the melting temperature is reached while studying the film in the TEM. Within this thesis work, the importance of film thickness and position in relation to the plume center have been important findings. These parameters could be explored in future work as well.

The thesis work has not obtained a chemical map which locate the dopants. An EDS or EELS experiment could provide this information. It is important to know whether the dopants cluster together or are uniformly distributed - both to understand the growth modes and for the workings of the IB material for solar cell applications. Future work on these sample is thus highly recommended to perform such an experiments.

Chemical maps would also be recommended for future method development for combining TEM and PDF. As the background subtraction is based on independent atom approximation, the concentration of the atoms is important. Improper background subtraction can result in artifacts in the PDF which can easily be misinterpreted as new pair distances. The chemical map would also provide insight into clusters of the different species, which is important for interpretation of the final PDF when the signal is intermixed [26]. Future work to evaluate the methodology is highly recommended to obtain an EDS or EELS scan as well. One could also perform a systematic study of different experimental parameters on the final PDF to find an optimized setup. The CPU practice set is well suited for such a study. Such a study was requested in the review article by Souza Junior et al. [32].

References

1. Goetzberger A, Luther J and Willeke G. Solar cells: past, present and future. Solar Energy Materials Solar Cells 2002; 74(1-4). DOI: 10.1016/S0927-0248(02)00042-9
2. Vossier A, Gualdi F, Dollet A, Ares R and Aimez V. Approaching the Shockley-Queisser limit: General assessment of the main limiting mechanisms in photovoltaic cells. Journal of Applied Physics 2015; 117(1). DOI: 10.1063/1.4905277
3. Conibeer G. Third-generation photovolatics. Materials today 2007; 7411. DOI: 10.1016/S1369-7021(07)70278-X
4. Yamaguchi M, Dimroth F, Geisz JF and Ekins-Daukes NJ. Multi-junction solar cells paving the way for super high-efficiency. Journal of Applied Physics 2021; 129. DOI: 10.1063/5.0048653
5. Raza E and Ahmad Z. Review on two-terminal and four terminal crystalline-silicon/perovskite tandem solar cells; progress, challenges and future perspectives. Energy Reports 2022; 8:5820–51. DOI: 10.1016/j.egyr.2022.04.028
6. Yang TCJ, Fiala P, Jeangros Q and Ballif C. High-Bandgap Perovskite Materials for Multijunction Solar Cells. Joule 2018; 2. DOI: 10.1016/j.joule.2018.05.008
7. Ramiro I and Martí A. Intermediate band solar cells: Present and future. Progress in Photovoltaics 2021; 29(7). DOI: 10.1002/pip.3351
8. Zhang J, Tse K, Wong M, Zhang Y and Zhu J. A brief review of co-doping. Frontiers of Physics 2016; 11(6). DOI: 10.1007/s11467-016-0577-2
9. Zhu W, Qiu X, Iancu V, Chen XQ, Pan H, Wang W, Dimitrijevic NM, Rajh T, Meyer HM, Paranthaman MP, Stocks GM, Weitering HH, Gu B, Eres G and Zhang Z. Band Gap Narrowing of Titanium Oxide Semiconductors by Noncompensated Anion-Cation Codoping for Enhanced Visible-Light Photoactivity. Phys. Rev. Lett. 2009 Nov; 103(22):226401. DOI: 10.1103/PhysRevLett.103.226401
10. Hassnain Jaffari G, Tahir A, Zafar Ali N, Ali A and Quashi US. Effect of Cr-N codoping on structural phase transition, Raman modes and optical properties of TiO_2 nanoparticles. Journal of Applied Physics 2017; 123(16). DOI: 10.1063/1.5003448
11. Wu F, Lan H, Zhang Z and Cui P. Quantum efficiency of intermediate-band solar cells based on non-compensated n-p codoped TiO2. The Journal of Chemical Physics, Volume 137 2012; 137(10). DOI: 10.1063/1.4750981
12. Kittel C. Introduction to Solid State Physics. John Wiledy Sons, Inc, 2005. Chap. 1
13. Hofmann P. Solid State Physics: An Introduction. Wiley-VCH Verlag GMBH Co, 2015. Chap. 1-2

14. Mascarenhas YP. Crystallography before the Discovery of X-Ray Diffraction. Revista Brasileira de Ensino de Física 2020; 42. DOI: 10.1590/1806-9126-RBEF-2019-0336

15. Dauter Z and Jaskolski M. How to read (and understand) Volume A of International Tables for Crystallography: an introduction for nonspecialists. Journal of Applied Crystallography 2010; 43:1150–71. DOI: /10.1107/S0021889810026956

16. Putnis A. Introduction to mineral sciences. University of Cambridge Press, 1992. Chap. 1:15

17. Hanaor DAH and Sorrell CC. Review of the anatase to rutile phase transformation. Journal of Material Science 2011; 46:855–74. DOI: 10.1007/s10853-010-5113-0

18. Mo SD and Ching W. Electronic and optical properties of three phases of titianium dioxide: Rutile, anatase and brookite. Physical Review B 1995; 51. DOI: 10.1103/PhysRevB.51.13023

19. Momma K. VESTA: A Three-Dimensional Visualization System for Electronic and Structural Analysis. Journal of Applied Crystallography 2008; 41. DOI: 10.1107/S0021889808012016

20. Tilley RJD. Understanding Solids: The Science of Materials. John Wiledy Sons, Ltd., Publication, 2013. Chap. 5

21. R. LP and Banfield JF. Formation of rutile nuclei at anatase 112 twin interfaces and the phase transformation in nanocrystalline titania. American Mineralogist 1999; 84:871–6. DOI: 10.2138/am-1999-5-622

22. Song M, Lu Z and Li D. Phase Transformations among TiO2 Polymorphs. Nanoscale 2018; 00. DOI: 10.1039/D0NR06226J

23. Williams DB and Carter CB. Transmission Electron Microscopy: A Textbook for Materials Science. Wiley-VCH Verlag GMBH Co, 2009

24. Fultz B and Howe J. Transmission Electron Microscopy and Diffractometry of Materials. Springer-Verlag Berlin Heidelberg, 2013

25. Hyvärinen A. Independent component analysis: recent advances. Philosophical Transactions of the Royal Society A 2013; 371(1984). DOI: 10.1098/rsta.2011.0534

26. Mu X, Chen L, Mikut R, Hahn H and Kübel C. Unveiling local atomic bonding and packing of amorphous nanophases via independent component analysis facilitated pair distribution function. Acta Materialia 2021; 212. DOI: 10.1016/j.actamat.2021.116932

27. Yao N and Epstein AK. Surface nanofabrication using focused ion beam. Microscopy: Science, Technology, Applications and Education 2010

28. Williams H. SEM for conductive and non-conductive specimens. Physics Education 2021; 56. DOI: 10.1088/1361-6552/ac1503

29. Weber T and Simonov A. The three-dimensional pair distribution function analysis of disordered single crystals: basic concepts. Zeitschrift Für Kristallographie Crystalline - Materilas. 2012; 227(5). DOI: 10.1524/zkri.2012.1504

30. Cockayne DJ and McKenzie DR. Electron Diffraction Analysis of Polycrystalline and Amorphous Thin Films. Acta Crystallographica 1988; A44:870–8. DOI: 10.1107/S0108767388004957

31. Gorelik TE, Neder R, Terban MW, Lee Z, Mu X, Jacob T and Kaiser U. Towards quantitative treatment of electron pair distribution function. Acta Crystallographica B. 2019; B75:532–49. DOI: /10.1107/S205252061900670X

32. Souza Junior JB, Schleder GR, Bettini J, Noguira IC, Fazzio A and Leite ER. Pair Distribution Function Obtained from Electron Diffraction: An Advanced Real-Space Structural Characterization Tool. Matter 2021; 4. DOI: /10.1016/j.matt.2020.10.025

33. Keen D and Goodwin AL. The crystallography of correlated disorder. Nature 2015; 521. DOI: 10.1038/nature14453

34. Ivanisenko Y, Kübel C, Nandam SH, Wang C, Mu X, Adjaoud O, Albe K and Hahn H. Structure and Properties of Nanoglasses. Advanced Engineering Materials 2018; 20. DOI: 10.1002/adem.201800404

35. Young C and Goodwin AL. Applications of pair distribution function methods to contemporary problems in materials chemistry. Journal of Materials Chemistry 2011; 21. DOI: 10.1039/C0JM04415F

36. Billinge S and Levin I. The Problems with Determining Atomic Structure at the Nanoscale. Science 2007; 316(5824). DOI: 10.1126/science.1135080

37. Zhu H, Huang Y, Ren J, Zhang B, Ke Y, Jen AKY, Zhang Q, Wang XL and Liu Q. Bridging Structural Inhomogeneity to Functionality: Pair Distribution Function Methods for Functional Materials Development. Advanced Science Review 2021; 8. DOI: 10.1002/advs.202003534

38. Hoque MM, Vergara S, Das PP, Ugarte D, Santiago U, Kumara C, Whetten RL, Dass A and Ponce A. Structural Analysis of Ligand-Protected Smaller Metallic Nanocrystals by Atomic Pair Distribution Function under Precession Electron Diffraction. The Journal of Physical Chemistry 2019; 123. DOI: 10.1021/acs.jpcc.9b02901

39. Correa LM, Moreira M and Rodriguez V. adn Ugarte D. Quantitative Structural Analysis of AuAg Nanoparticles Using a Pair Distribution Function Based on Precession Electron Diffraction: Implications for Catalysis. ACS Applied Nano Materials 2021; 4. DOI: 10.1021/acsanm.1c02978

40. Mu X, Neelamraju S, Koch CT, Totò N, Schön JC, Fisher D, Jansen M and Aken PA van. Evolution of order in amorphous-to-crystalline phase transformation of MgF2. Journal of Applied Crystallography 2013; 46. DOI: 10.1107/S0021889813011345

41. Polyakova IG. Glass: Selected Properties and Crystallization. De Gruyter, 2014. DOI: 10.1515/9783110298581.197

42. Volceanov A. Basicity or Ionicity - A New Approach for Understanding Glass Properties. Advanced Materials Research 2008. DOI: 10.4028/www.scientific.net/AMR.39-40.129

43. Sun S, Song P, Cui J and Liang S. Amorphous TiO2 nanostructures: synthesis, fundamental properties and photocatalytic applications. Catalysis Science Technology 2019; 9. DOI: 10.1039/c9cy01020c

44. Mihailescu IN and Caricato AP. Pulsed Laser Ablation: Advances and Applications in Nanoparticles and Nanostructuring Thin Film. Pan Stanford Publishing Pte. Ltd., 2018

45. Greer JA. History and current status of commercial pulsed laser deposition equipment. Journal of Physics D: Applied Physics 2014; 47. DOI: 10.1088/0022-3727/47/3/034005

46. S. CS and Grigoropoulos CP. Determination of Kinetic Energy Distribution in a Laser-Ablated Titanium Plume by Emission and Laser-Induced Fluorescence Spectroscopy. Journal of Heat Transfer 2000; 122. DOI: 10.1115/1.1318214

47. Kaiser N. Review of the fundamentals of thin-film growth. Applied Optics 2002; 41. DOI: 10.1364/AO.41.003053

48. Magnfält D. Fundamental processes in thin film growth: The origin of compressive stresss and the dynamics of the early growth stages. PhD thesis. Linköpig University, 2014

49. Zhang Z and Lagally MG. Atomistic Processes in the Early Stages of Thin-Film Growth. Science 1997; 276(5311):377–83. DOI: 10.1126/science.276.5311.377

50. Smith DL. Thin-Film Deposition: Principles Deposition. McGraw-Hill, Inc, 1995. Chap. 5

51. Borroto A, García-Wong AC, Bruyère S, Migot S, Pilloud D, Pierson JF, Mücklich F and Horwat D. Composition-driven transition from amorphous to crystalline films enables bottom-up design of functional surfaces. Applied Surface Science 2021; 538. DOI: 10.1016/j.apsusc.2020.148133

52. Lackner JM, Waldhauser W, Alamanou A, Teickert C, Schmied F. Major L and Major B. Mechanisms for self-assembling topography formation in low-temperature vacuum deposition of inorganic coatings on polymer surfaces. Technical Sciences 2010; 58. DOI: 10.2478/v10175-010-0026-2

53. Drift A van der. Evolutionary selection, a principle governing growth orientation in vapour-deposited layers. Philips Research Reports, Volume 22 1967; 22:267–88

54. Huang H. An atomistic simulator for thin film deposition in three dimensions. Journal of Applied Physics, Volume 84 1998. DOI: 10.1063/1.368539

55. Navrotsky A. Energetics of nanoparticle oxides: interplay between surface energy and polymorphism. Geochemical Transactions Review 2003; 4. DOI: 10.1039/b308711e

56. Fan L, Gao X, Lee D, Guo EJ, Lee S, Snijders PC and Ward TZ. Kinetically Controlled Fabrication of Single-Crystalline TiO_2 Nanobrush Architectures with High Energy 001 Facets. Advanced Science News 2017; 4(8). DOI: 10.1002/advs.201700045

57. Jiang F, Yang L, Zhou D, He G, Zhou J, Wang F and Chen ZG. First-principles atomistic Wulff constructions for an equilibirum rutile $TiO2$ shape modeling. Applied Surface Science 2018; 436:989–94. DOI: 10.1016/j.apsusc.2017.12.050

58. Liu G, Yang H, Pan J, Yang YQ, Lu GQ and Cheng HM. Titanium Dioxide Crystals with Tailored Facets. Chemical Reviews 2014; 114. DOI: 10.1021/cr400621z

59. Lysne H, Brakstad T, Kildemo M and Reenas TW. Improved modeling and simulation of PLD and combinatorial PLD. Department of Physics, Norwegian University of Science and Technology 2022. (Unpublished work)

60. Khatim O, Amamra M, Chhor K, Bell AMT, Novikov D, Vrel D and Kanaev A. Amorphous-anatase phase transition in single immobilized $\mathrm{TiO_2}$ nanoparticles. Chemical Physical Letters 2013; 558. DOI: 10.1016/j.cplett.2012.12.019

61. Nie X, Zhuo S, Maeng G and Sohlberg K. Doping of $\mathrm{TiO_2}$ Polymorphs for Altered Optical and Photocatalytic Properties. International Journal of Photoenergy 2009; 2009. DOI: 10.1155/2009/294042

62. Balakrishnan G, Manavalan S, Venkatesh Babu R and Song J. Effect of substrate temperature on microstructure and properties of nanocrystalline titania thin films prepared by pulsed laser deposition. NANOSYSTEMS: PHYSICS, CHEMISTRY, MATHEMATICS 2016; 7. DOI: 10.17586/2220-8054-2016-7-4-621-623

63. György E, Socol G, Axente E, Mihailescu IN, Ducu C and Ciuca S. Anatase phase TiO2 thin films obtained by pulsed laser deposition for gas sensing applications. Applied Surface Science 2005; 247(1-4). DOI: 10.1016/j.apsusc.2005.01.074

64. György E, Pérez del Pino A, Sauthier G, Figueras A, Alsina F and Pascual J. Structural, morphological and local electric properties of TiO2 thin films grown by pulsed laser deposition. Journal of Physics D: Applied Physics 2007; 40(17). DOI: 10.1088/0022-3727/40/17/035

65. Long H, Yang G, Chen A, Li Y and Lu P. Growth and characteristics of laser deposited anatase and rutile TiO2 films on Si substrates. Thin Solid Films 2008; 517(2). DOI: 10.1016/j.tsf.2008.08.179

66. Sanz M, Walczak M, Oujja M, Cuesta A and Castillejo M. Nanosecond pulsed laser deposition of TiO_2: nanostructure and morphology of deposits and plasma diagnosis. Thin Solid Films 2009; 517. DOI: 10.1016/j.tsf.2009.04.026

67. Walczak M, Papdopoulou EL, Sanz M, Manousaki M, Marco JF and Castillejo M. Structural and Morphological Characterization of TiO2 Nanostructured Films Grown by Nanosecond Pulsed Laser Deposition. Applied Surface Science 2009; 255. DOI: 10.1016/j.apsusc.2008.07.098

68. Wijnands T, Houwman EP, Koster G and Huijben M. Numerical modeling of the plasma plume propagation and oxidation during pulsed laser deposition of complex oxide thin films. Physical Review Materials 2020; 4. DOI: 10.1103/PhysRevMaterials.4.103803

69. Walczak M, Oujja M and Marco JF. Pulsed laser deposition of TiO_2: diagnostic of the plume and characterization of nanostructured deposits. Applied Physics A 2008; 93. DOI: 10.1007/s00339-008-4704-y

70. Zhao L. Visible-light photocatalytic activity of nitrogen-doped TiO_2 thin film prepared by pulsed laser deposition. Applied Surface Science, Volume 254 2008. DOI: 10.1016/j.apsusc.2008.01.069

71. Albu DF, Lungu J and Popescu-Pelin G. Thin Film Fabrication by Pulsed Laser Deposition from TiO2 Targets in O2, N2, He, or Ar for Dye-Sensitized Solar Cells. Coatings 2022; 12(293). DOI: 10.3390/coatings12030293

72. Socol G, Gnatyuk Y, Stefan N, Smirnova N, Djokic V, Sutan C, Malinovschi V, Strnculescu A, Korduban O and Mihailescu IN. Photocatalytic activity of pulsed laser deposited TiO2 thin films in N2, O2 and CH4. Thin Solid Films 2010; 518. DOI: 10.1016/j.tsf.2009.12.051

73. Ali A, Yassitepe E and Karim A. Phase Transformations in the Pulsed Laser Deposition Grown TiO2 Thin Films as a Consequence of O2 Partial Pressure and Nd Doping. The Journal of Physical Chemistry 2015; 119. DOI: 10.1021/acs.jpcc.5b01046

74. Nematollahi M, Yang X and Seim E. Compositional and structural properties of pulsed laser-deposited ZnS:Cr films. Applied Physics A 2006; 122. DOI: 10.1007/s00339-016-9594-9

75. Bauer W, Perram GP and Haugan T. Comparison of plume dynamics for laser ablated metals: Al and Ti. Journal of Applied Physics 2017; 123. DOI: 10.1063/1.5011028

76. Solstrand H. Characterization of TiO2 based thin films using Raman Spectroscopy. MA thesis. Norwegian University of Science and Technology, 2021

77. Michaelsen MG. Pulsed Laser Deposited TiO2: X-Ray Diffraction and Raman Spectroscopy Studies. MA thesis. Norwegian University of Science and Technology, 2022

78. Schaffer B. Digital Micrograph. 2016 Sep :167–96. DOI: 10.1007/978-3-319-26651-0_6

79. Seto Y. ReciPro: free and open-source multipurpose crystallographic software integrating a crystal model database and viewer, diffraction and microscopy simulators, and diffraction data analysis tools. Journal of Applied Crystallography 2022; 55. DOI: 10.1107/S1600576722000139

80. Schneider CA. NIH Image to ImageJ: 25 years of image analysis. Nature Methods 2012; 9. DOI: 10.1038/nmeth.2089

81. Inkscape Project. Inkscape. Version 0.92.5. 2020 Apr 16. Available from: https://inkscape.org

82. hyperspy/hyperspy. Version 1.7.0. 2021. DOI: 10.5281/zenodo.592838

83. pyxem/pyxem. Version 0.14.1. 2021. DOI: 10.5281/zenodo.2649351

84. Johnstone DN, Francis C and Crout P. pyxem/demos/08 Pair Distribution Function Analysis. Version 0.14.1. 2021. DOI: 10.5281/zenodo.2649351

85. Pedregosa F, Varoquaux G, Gramfort A, Michel V, Thirion B, Grisel O, Blondel M, Prettenhofer P, Weiss R, Dubourg V et al. Scikit-learn: Machine learning in Python. Journal of machine learning research 2011; 12:2825–30

86. Miller J. Solid geometry definitions. Dihedral, polyhedral angle. Prismatic, cylindrical, pyramidal, conical surface. Polyhedron, prism, parallelepiped, cylinder, pyramid, prismatoid. Frustum. Conic section. Circle, axis, pole of a sphere. Zone. Polar triangle. Spherical polygon, triangle, sector. Available from: https://solitaryroad.com/c080.html [Accessed on: 2022 May 17]

87. Brito Mota F de, Justo JF and Fazzio A. Structural properties of amorphous silicon nitride. Physical Review B 1998; 58(13). DOI: 10.1103/PhysRevB.58.8323

A Appendix - Supporting Results

Supporting results which has not been included in the results chapter are provided here.

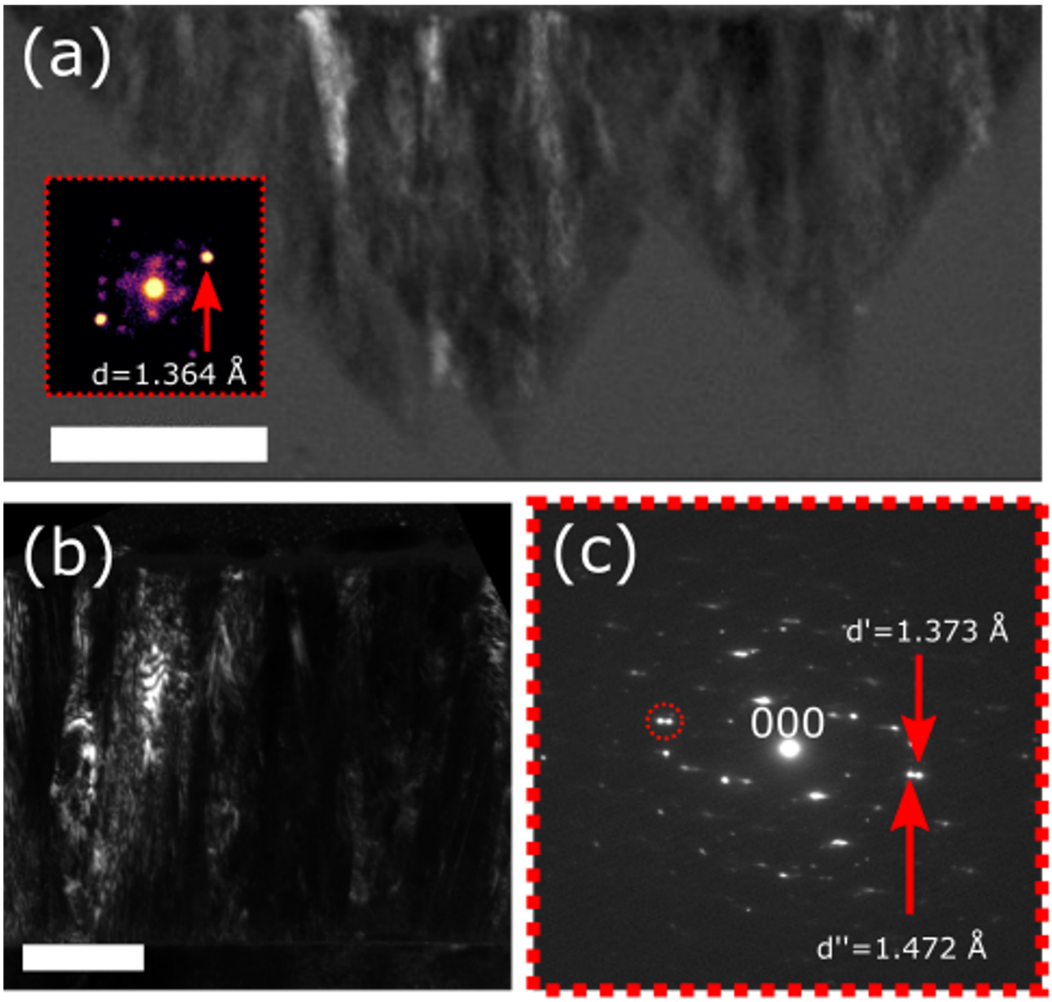

Figure A1: The following is results from position -0.75 cm and wafer center in position 0.0 cm from conventional TEM and SPED experiment, respectively. VDF-TEM image (a) obtained from an annular aperture at the reflection highlighted in the inserted DP. The DP is from the column present in the image. Anatase is expected to be the phase present here. Conventional DFTEM (b) and SAED pattern (c) show similar split as seen where anatase is found locally in the film. Scale bars are 100 nm.

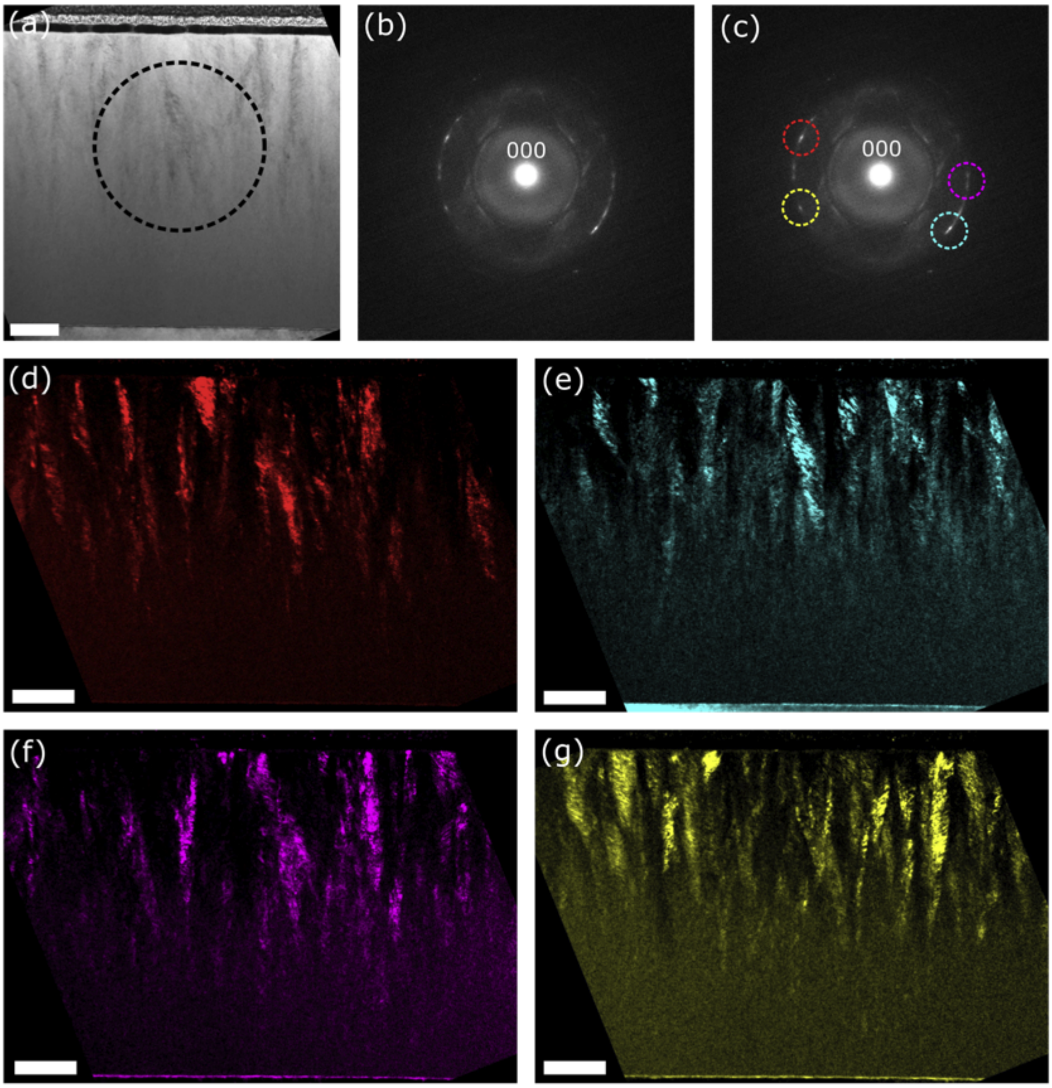

Figure A2: Conventional TEM results from the second plume center (pos.1.25 cm). BFTEM image (a) and corresponding DP (b) from the dashed region was studied with DFTEM imaging. The approximate size and location of the objective aperture is visualized (c), and colorcoded to the corresponding DFTEM images (d-g). Scale bars are 100 nm.

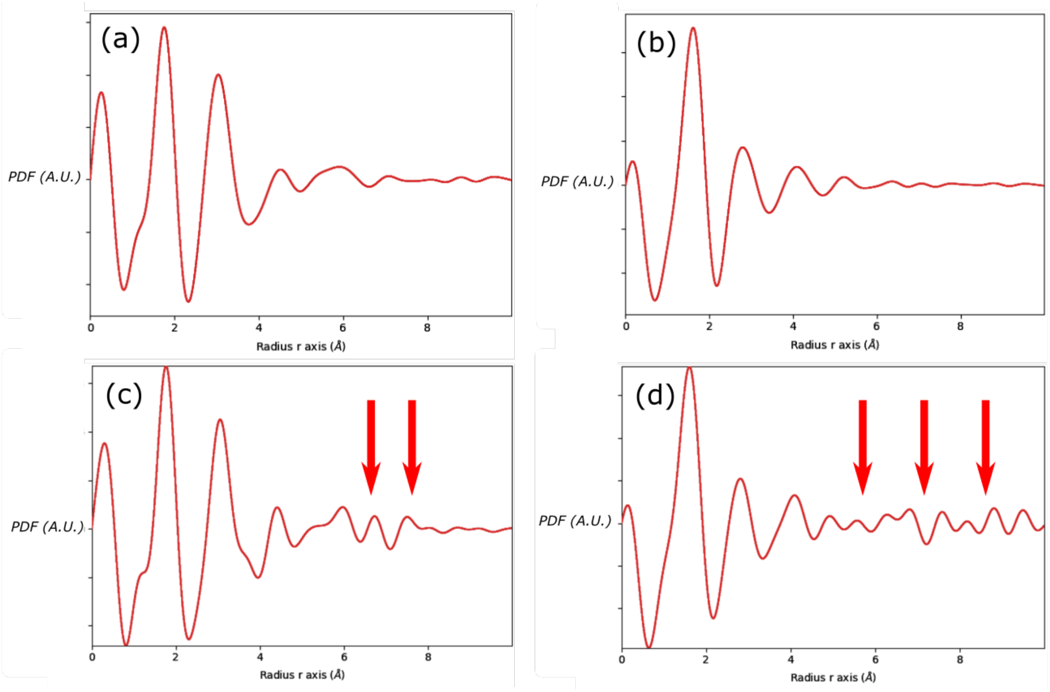

Figure A3: PDFs obtained from the CPU practice sets. The average PDF from the bottom (a) and top (b) amorphous SiO_2 layer. PDF from single pixels in the bottom (c) and top (d). Ripples in the single pixels indicated by red arrows are artifacts from the pre-processing.

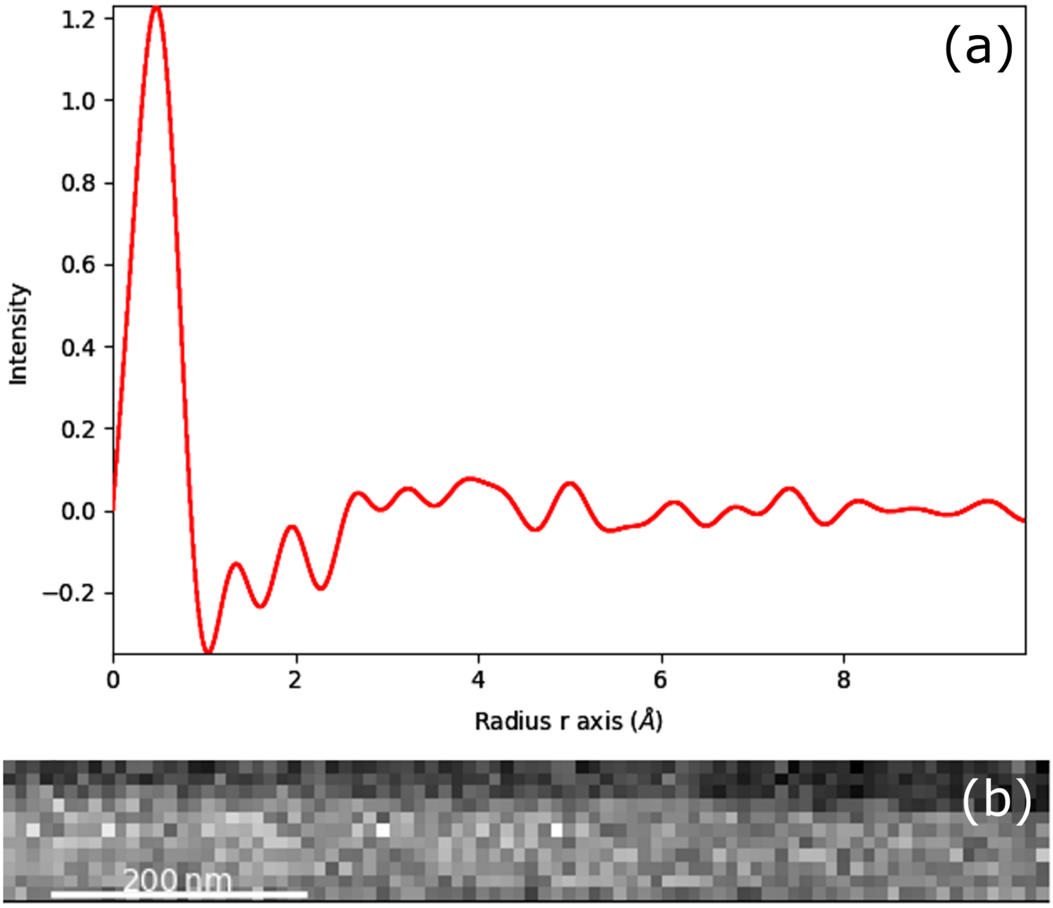

Figure A4: Third component (a) and its loading map (b) from the decomposition of the SPED datasett of the CPU multipurpose lamella.

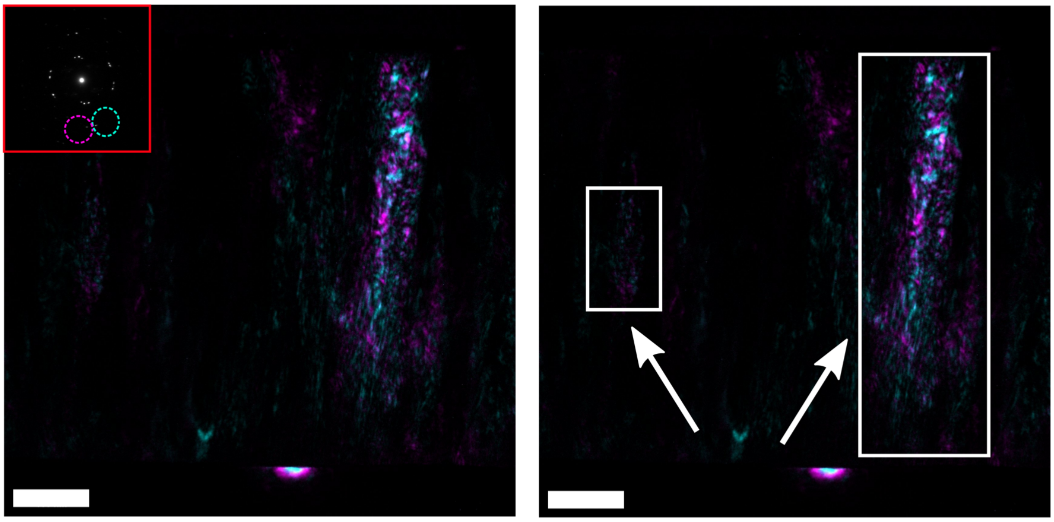

Figure A5: The following results are obtained from the lamella at the first plume center (-1.25 *cm*). DFTEM images from the two ($\bar{2}00$ reflections was obtained. The approximate location and size of the objective aperture is presented in the DP in (a), and the merged DFTEM image is included in (b). Scale bar is 100 nm.

B Appendix - Code for PDF analysis of Amorphous SiO_2

The following includes the code used for the PDF analysis on the layered amorphous SiO_2 CPU SPED dataset. Emil Frang Christiansen at the TEM Gemini group provided snippets for the centering of the direct beam and the mask. The transformation from the total scattered DP to the PDF follows the pyxem tutorial on PDF closely [84]. The code serve as a jupyter notebook governing the workflow for obtaining the PDF, which can be further developed.

```
# Import the necessary libraries
%matplotlib qt5

import numpy as np
import matplotlib.pyplot as plt
import hyperspy.api as hs
import pyxem as pxm

#Print version of pyxem, should be 0.14.0_dev to work...
if (pxm.__version__ != '0.14.0-dev'):
    prompt = input('You should get pyxem version 0.14.0-dev, continue anyways?
                    [y/n]')
    if prompt == '' or prompt.lower() == 'y':
        print("Ok, continuing...")
    else:
        pass
        print("Ok, do your changes...")
else:
    print(pxm.__version__)



# Import dataset and set metadata
file = r'Path to the data'

#Upload your dataset and inspect metadata
experimental_data = hs.load(file)
experimental_data.set_signal_type('electron_diffraction')
experimental_data.metadata.set_item("General.title", 'PDF Analysis: Amorphous SiO2')
print(experimental_data.metadata)
```

```
# Calibration diffraction scale on diffraction pattern of the substrate
from hyperspy.roi import Line2DROI

# a line profile accross known diffraction spots. Move to correct positions
x1 = -15
x2 = 13
y1 = -45
y2 = 45
line = Line2DROI(x1=x1, y1=y1, x2=x2, y2=y2, linewidth=2)
image1 = experimental_data.inav[100, 450]

image1.plot(vmax=0.1, norm='symlog',cmap="viridis")
line.add_widget(image1)

# Find intensity across line
trace = line(image1).as_signal1D(0)
trace.plot(norm="log")

import scipy.signal as sps
sps.find_peaks(trace.data)

# the number of pixels center to 111 peak
dist_002_pixels = (94 - 9)/4
# the distance in 1/A of the 111 peak
g_dist = 0.3143
diffraction_calibration = g_dist/dist_111_pixels

print(diffraction_calibration)

# Set calibration. Scan calibration known from film thickness and scan dimension
experimental_data.set_diffraction_calibration(diffraction_calibration)
experimental_data.set_scan_calibration(605/355)

#Now normalize intensities
experimental_data.data = experimental_data.data.astype('float64')
```

```
experimental_data.data *= 1 / experimental_data.data.max()

# Plot to inspect the data
experimental_data.plot(vmax=0.1, norm='symlog', cmap='magma_r')

# Navigate ROI to crop set
reg = hs.roi.RectangularROI(left=50, top=50, right=60, bottom=60)
experimental_data.plot(cmap='magma_r', vmax=0.1)
reg.add_widget(experimental_data)

# Crop and perfrom VDF to inspect data
roi_crop =reg(experimental_data)
roi_crop.plot(vmax=0.1, norm='symlog', cmap='inferno')
aperture_bf = hs.roi.CircleROI(cx=0.,cy=0, r_inner=0, r=0.07)
roi_crop.plot_integrated_intensity(aperture_bf)

# Crop summation of DPs to inspect any asymmetry in the data
maximums = roi_crop.max(axis=(0, 1))
maximums.plot(vmax = 0.1,cmap='magma_r', norm='symlog')

#The following snippet was provided by Emil Frang Christiansen for centering of
# the direct beam
roi_crop.set_diffraction_calibration(1)
roi_crop.set_scan_calibration(1)

#Make roi and check position and radii
roi = hs.roi.CircleROI(0, 0, 8)
maximums = roi_crop.max(axis=(0, 1))
maximums.plot(vmax = 0.1,cmap='inferno_r', norm='symlog')
roi.add_widget(maximums)

# Convert ROI from calibrated coordinates to pixel position
cx = int((roi.cx - maximums.axes_manager[0].offset)
          / maximums.axes_manager[0].scale)
cy = int((roi.cy - maximums.axes_manager[1].offset)
          / maximums.axes_manager[1].scale)
```

```
r = int(roi.r / maximums.axes_manager[0].scale)
print(f'I will use a mask around ({cx}, {cy}) with radius {r} for COM algorithm')

#Use center of mass function to find x- and y-shifts
com = roi_crop.center_of_mass(mask=(cx, cy, r))
com.plot()
com.get_bivariate_histogram().plot()

# Shift the diffraction to center:
roi_crop.shift_diffraction(shift_x = com.inav[0]-cx, shift_y = com.inav[1]-cy,
                           inplace=True)

# Create mask
roi_crop.data.shape
mask = np.ones(roi_crop.data.shape, dtype=bool)
mask = np.ones(roi_crop.data.shape, dtype=bool)
mask[:, :, roi_crop.get_direct_beam_mask(11).data] = 0 #Changed from 16
mask_signal = hs.signals.Signal2D(mask)
mask_signal.plot()

# Perform azimuthal integration to obtain a one-dimensional scattering profile
r_mean = roi_crop.radial_average(centre_x = 128, centre_y = 128, mask_array = mask)
r_mean.set_signal_type('electron_diffraction')
r_mean.set_diffraction_calibration(diffraction_calibration)
r_mean.set_scan_calibration(605/355)

# Perform VADFTEM image to study the scattering profile
r_mean.T.plot()

# Extract test image for the PDF analysis
test = r_mean.inav[150,35]
test = pxm.signals.ElectronDiffraction1D([[test.data]])
test.set_diffraction_calibration(diffraction_calibration)
test.plot()
test
```

```
# Extract background by the use of single atom scattering approximation
rigen = pxm.generators.ReducedIntensityGenerator1D(roi_crop)
elements = ['Si','O']
fracs = [0.333,0.667]
rigen.set_s_cutoff(s_min=0.9,s_max=2.9)
rigen.fit_atomic_scattering(elements,fracs,scattering_factor='lobato',
                            plot_fit=True,iterpath='serpentine')
ri = rigen.get_reduced_intensity()

# Damp low and high scattering angles by an error and Lorch function, respectively
ri.damp_low_q_region_erfc(offset=10)
ri.damp_lorch(s_max=2.6)

# Obtain the PDF for the pixel
pdfgen = pxm.generators.PDFGenerator1D(ri)
s_min, s_max = 0., 2.6
pdf = pdfgen.get_pdf(s_min=s_min, s_max=s_max, r_max=10)
pdf.metadata.set_item("General.title", 'Pair Distribution Function')
pdf.plot()

# Perform preprocessing on the whole set
rigen_all = pxm.generators.ReducedIntensityGenerator1D(r_mean)

elements = ['Si','O']
fracs = [0.333,0.667]

rigen_all.set_s_cutoff(s_min=0.9,s_max=2.9) # Originally 0.9 and 1.7
rigen_all.fit_atomic_scattering(elements,fracs,scattering_factor='lobato',
                                plot_fit=True,iterpath='serpentine')

ri_all = rigen_all.get_reduced_intensity()
ri_all.damp_lorch(s_max=2.6)
ri_all.damp_low_q_region_erfc(offset=10)

pdfgen_all = pxm.generators.PDFGenerator1D(ri_all)
```

```
s_min, s_max = 0., 2.9

pdf_all = pdfgen_all.get_pdf(s_min=s_min, s_max=s_max, r_max=10)
pdf_all.metadata.set_item("General.title", 'Pair Distribution Function')
pdf_all.set_scan_calibration(605/355)
pdf_all.plot()

# De-whitening to find number of principal components
pdf_all.change_dtype('float32')
pdf_all.decomposition(algorithm='SVD', output_dimension=100)

# Plot scree plot
pdf_all.plot_explained_variance_ratio()

# Perform ICA decomposition
pdf_all.blind_source_separation(number_of_components=3)
pdf_all.plot_bss_results()
loadings = pdf_all.get_decomposition_loadings()
factors = pdf_all.get_decomposition_factors()

# Save the components and their loading maps
loadings.save(r'loadings.hspy')
factors.save(r'factors.hspy')
```

C Appendix - Tables with d-spacings

The experimental and theoretical d-spacing are provided in this appendix for the indexation of the DP in this thesis. The values are presented in an overview table. The Spot ID v1 tool was used with an input error of ± 5 %.

Table C1: Theoretical and experimental d-spacing for indexation in Figure 29. Rutile [012] was identified as the phase and orientation present. The closes d-spacing of rutile and anatase is presented together with the zone axis candidates obtained from the Spot ID v1 tool in the Recipro software [79].

Indexation of DP		
Experimental DP	Rutile	Anatase
d1 = 2.286 Å	$d_{200,020}$ = 2.297 Å	$d_{110,112,021,201}$ = 2.332 Å
d2 = 1.684 Å	$d_{211,121}$ = 1.687 Å	$d_{012,102,121,211}$ = 1.666 Å
Recipro candidates	[012]	No candidate found

Table C2: Theoretical and experimental d-spacing for indexation in Figure 31. Rutile [001] was identified as the phase and orientation present. The closes d-spacing of rutile and anatase is presented together with the zone axis candidates obtained from the Spot ID v1 tool in the Recipro software [79].

Indexation of DP		
Experimental DP	Rutile	Anatase
d1 = 4.550 Å	d_{100} = 4.594 Å	d_{002} = 4.757 Å
d2 = 3.125 Å	d_{110} = 3.248 Å	d_{101} = 3.517 Å
Recipro candidates	[001]	No candidate found

Table C3: Theoretical and experimental d-spacing for indexation in Figure 32. Rutile [101] was identified as the phase and orientation present. The closes d-spacing of rutile and anatase is presented together with the zone axis candidates obtainted from the Spot ID v1 tool in the Recipro software [79].

Indexation of DP		
Experimental DP	Rutile	Anatase
d1 = 2.314 Å	$d_{200,020}$ = 2.297 Å	$d_{110,112,021,201}$ = 2.332 Å
d2 = 1.701 Å	$d_{012,102,121,211}$ = 1.687 Å	$d_{012,102,121,211}$ = 1.666 Å
d3 = 2.195 Å	d_{111} = 2.187 Å	$d_{110,112,021,201}$ = 2.332 Å
d4 = 2.482 Å	$d_{101,011}$ = 2.487 Å	$d_{103,013}$ = 2.431 Å
Recipro candidates	[101]	No candidate found

Table C4: Theoretical and experimental d-spacing for indexation in Figure 33. Rutile [100] was identified as the phase and orientation present. The closes d-spacing of rutile and anatase is presented together with the zone axis candidates obtained from the Spot ID v1 tool in the Recipro software [79].

Indexation of DP		
Experimental DP	Rutile	Anatase
d1 = 1.479 Å	d_{002} = 1.479 Å	$d_{123,213,204,024}$ = 1.493 Å
d2 = 2.510 Å	$d_{101,011}$ = 2.487 Å	$d_{103,013}$ = 2.431 Å
d3 = 2.310 Å	d_{111} = 2.297 Å	$d_{110,112,021,201}$ = 2.332 Å
d4 = 1.370 Å	$d_{301,031}$ = 1.360 Å	d_{116} = 1.364 Å
Recipro candidates	[100]	No candidate found

Table C5: Theoretical and experimental d-spacing for indexation in Figure 34. Rutile was identified as phase, and the orientation is a higher order Laue zone axis as there is only a single systematic row. The closes d-spacing of rutile and anatase from Recipro [79].

Indexation of DP		
Experimental DP	Rutile	Anatase
d1 = 3.226 Å	d_{110} = 3.290 Å	$d_{100,010,101,011}$ = 3.517 Å
d2 = 1.634 Å	d_{220} = 1.645 Å	$d_{012,102,121,211}$ = 1.666 Å
Recipro candidates	HOLZ	No candidate found

Table C6: Theoretical and experimental d-spacing for indexation in Figure 36. The closes d-spacing of rutile and anatase is presented.

Indexation of DP		
Experimental DP	Rutile	Anatase
d1 = 3.304 Å	d_{110} = 3.290 Å	$d_{100,010,101,011}$ = 3.517 Å

Table C7: Theoretical and experimental d-spacing for indexation in Figure 38. Anatase $[11\bar{1}]$ was identified as the phase and orientation present. The closes d-spacing of rutile and anatase is presented together with the zone axis candidates obtained from the Spot ID v1 tool in the Recipro software [79].

Indexation of DP		
Experimental DP	Rutile	Anatase
d1 = 2.447 Å	$d_{101,011}$ = 2.487 Å	$d_{112,110,201,021}$ = 2.332 Å
d2 = 3.610 Å	d_{110} = 3.290 Å	$d_{100,010,101,011}$ = 3.517 Å
d3 = 1.665 Å	d_{220} = 1.645 Å	$d_{012,102,121,211,333}$ = 1.666 Å
d4 = 1.364 Å	$d_{301,031}$ = 1.375 Å	$d_{220,002}$ = 1.338 Å
Recipro candidates	No candidate found	[111]

Table C8: Theoretical and experimental d-spacing for indexation of the indented DP in Figure 34. Rutile was identified as phase, and the orientation is a higher order Laue zone axis as there is only a single systematic row. The closes d-spacing of rutile and anatase from Recipro [79].

Indexation of DP		
Experimental DP	Rutile	Anatase
d1 = 3.226 Å	d_{110} = 3.290 Å	$d_{100,010,101,011}$ = 3.517 Å
d2 = 1.634 Å	d_{220} = 1.645 Å	$d_{012,102,121,211}$ = 1.666 Å
Recipro candidates	HOLZ	No candidate found

Table C9: Theoretical and experimental d-spacing for indexation of the indented DP in Figure 40. Rutile [111] was identified as the phase and orientation present. The closes d-spacing of rutile and anatase is presented together with the zone axis candidates obtained from the Spot ID v1 tool in the Recipro software [79].

Indexation of DP		
Experimental DP	Rutile	Anatase
d1 = 3.187 Å	d_{110} = 3.290 Å	$d_{100,010,101,011}$ = 3.517 Å
d2 = 2.516 Å	$d_{101,011}$ = 2.487 Å	$d_{103,013}$ = 2.431 Å
Recipro candidates	[111]	No candidate found

Table C10: Theoretical and experimental d-spacing for indexation of the indented DPs in Figure 41. Rutile [111] was identified as the phase and orientation present in the orange, blue and green colored pixels. The closes d-spacing of rutile and anatase is presented together with the zone axis candidates obtained from the Spot ID v1 tool in the Recipro software [79].

Indexation of DP		
Experimental DP	Rutile	Anatase
Orange		
d1 = 3.228 Å	d_{110} = 3.290 Å	$d_{100,010,101,011}$ = 3.517 Å
d2 = 2.516 Å	$d_{101,011}$ = 2.503 Å	$d_{103,013}$ = 2.431 Å
Recipro candidates	[111]	No candidate found
Light green		
d1 = 3.259 Å	d_{110} = 3.290 Å	$d_{100,010,101,011}$ = 3.517 Å
Recipro candidates	HOLZ	No candidate found
Cyan		
d1 = 3.297 Å	d_{110} = 3.290 Å	$d_{100,010,101,011}$ = 3.517 Å
Recipro candidates	HOLZ	No candidate found
Dark blue		
d1 = 3.307 Å	d_{110} = 3.290 Å	$d_{100,010,101,011}$ = 3.517 Å
d2 = 2.546 Å	$d_{101,011}$ = 2.487 Å	$d_{103,013}$ = 2.431 Å
Recipro candidates	[111]	No candidate found
Pink		
d1 = 3.348 Å	d_{110} = 3.290 Å	$d_{100,010,101,011}$ = 3.517 Å
Recipro candidates	HOLZ	No candidate found
Dark green		
d1 = 3.171 Å	d_{110} = 3.290 Å	$d_{100,010,101,011}$ = 3.517 Å
d2 = 2.498 Å	$d_{101,011}$ = 2.487 Å	$d_{103,013}$ = 2.431 Å
Recipro candidates	[111]	No candidate found

Table C11: Theoretical and experimental d-spacing for indexation of the dominant candidate in Figure 46 (f). Values from the lower left DP is provided. The indexation order follows that of indexation in Figure 32. Rutile [101] was identified as the phase and orientation present. The closes d-spacing of rutile and anatase is presented together with the zone axis candidates obtainted from the Spot ID v1 tool in the Recipro software [79].

Indexation of DP		
Experimental DP	Rutile	Anatase
d1 = 2.276 Å	$d_{200,020}$ = 2.297 Å	$d_{110,112,021,201}$ = 2.332 Å
d2 = 1.661 Å	$d_{012,102,121,211}$ = 1.687 Å	$d_{012,102,121,211}$ = 1.666 Å
d3 = 2.222 Å	d_{111} = 2.187 Å	$d_{110,112,021,201}$ = 2.332 Å
d4 = 2.497 Å	$d_{101,011}$ = 2.487 Å	$d_{103,013}$ = 2.431 Å
Recipro candidates	[101]	No candidate found

D Appendix - Training Issues and Lessons

This appendix mainly serves as a reflection over the issues that occurred in the training and during sample preparation. Both as a part of self-development, but also for transparency of the thesis work. It may additionally serve as a form of preparation for future master students to make their work more efficient preparing or overcoming these issues and setbacks.

Placing the TEM grid on the FIB holder is a delicate process. The grid may be misplaced or broken during the process, and if the grid contains a lamella at a finger, poor handling of the TEM grid can be a large issue. An image illustrating a misplaced TEM grid is visualized in Figure D1. A misplaced grid would make the transportation with the omniprobe difficult. An image illustrating a broken TEM grid is presented in Figure D2.

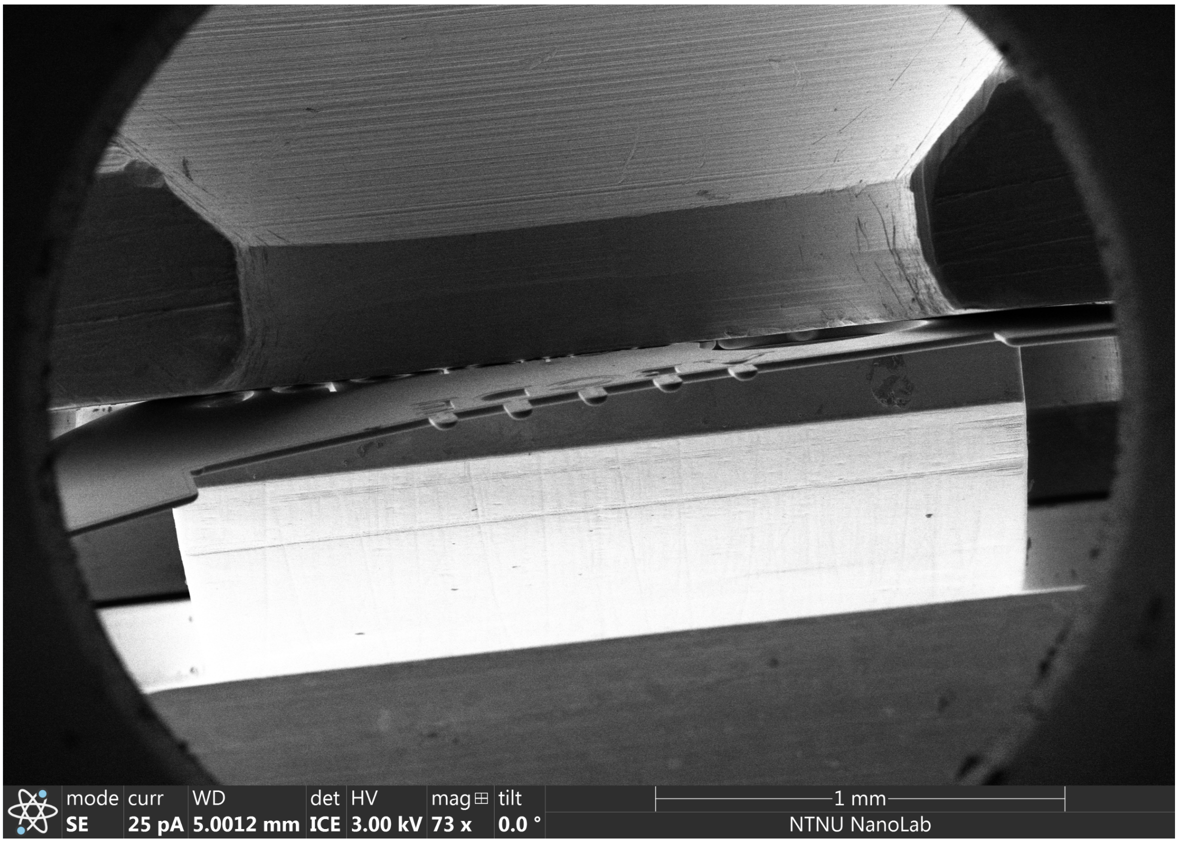

Figure D1: Top-view image of misplaced TEM grid in the FIB holder.

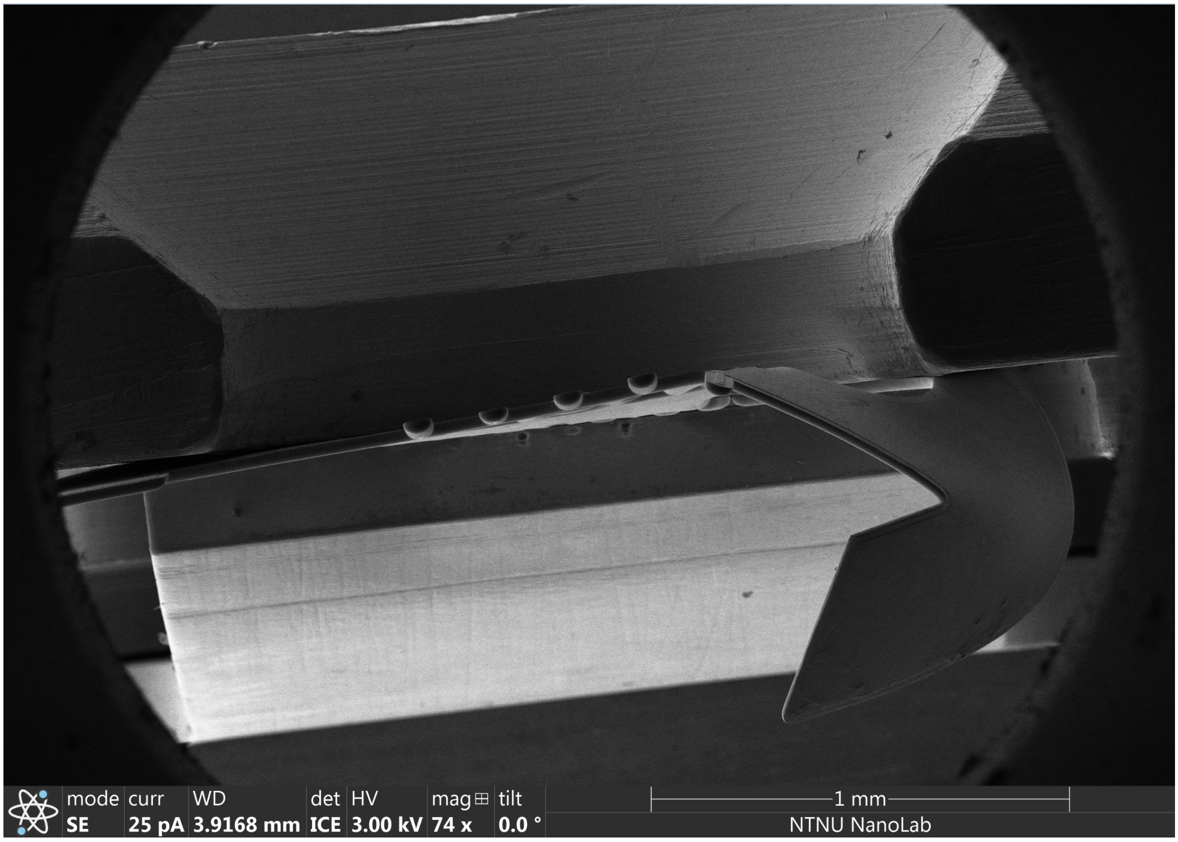

Figure D2: Top-view image of misplaced TEM grid in the FIB holder.

Due to risk of damaging the grid during transportation between the instruments, it is common procedure to only place a single lamella at each TEM grid. The benefit of this is that is reduces the risk. However, as the TEM holder only can hold a single grid at the time, one increases the time at the TEM instrument. When studing many separate lamellae, then this can become time consuming. Placing two to three lamella at the same grid can thus make the experiment more efficient as one can study multiple samples during the same TEM experiment. This also reducing the experimental variable between the different sessions. This thus give high reward, but with an increased risk as loss or damage to a TEM grid would thus more problematic. Extra consideration was given to the mounting step when placing the lamella to the grid. This was successful, and no lamellae or grids were broken during this thesis. A side-view image showing two lamellae placed on the same TEM grid, but at different fingers, is presented in Figure D3.

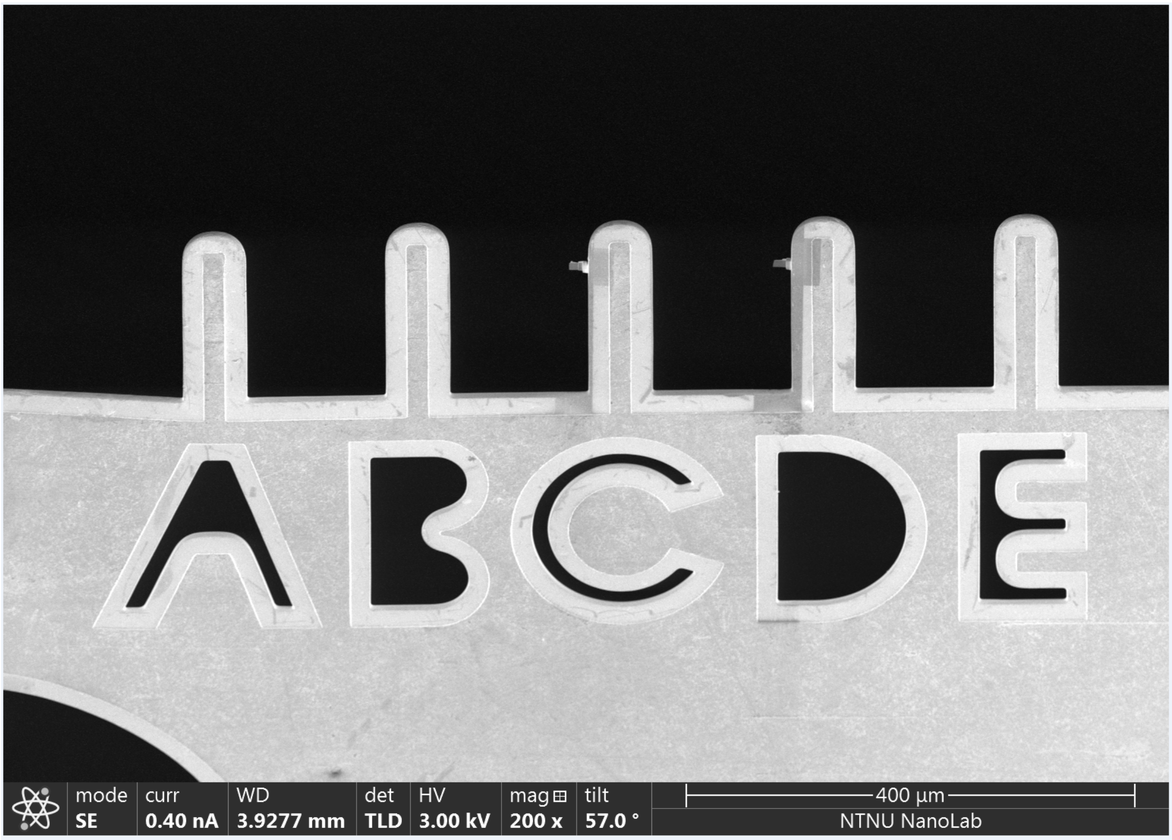

Figure D3: Side-view image of multiple lamellae on the TEM grid.

TiO_2 is a wide band gap semiconductor. It is thus not conducting charged particles. Charging effects was thus present on the film prior to the Au gold layer was deposited. Small distortion of the image is seen in Figure D4. Even though image is not severely distorted, charging effects may show up from deflection of the beam during deposition or milling. A quick check for charging effects such as this may be useful. Additionally, the GIS needle was not grounded during operation in one of the FIB sessions. This showed up as bending effects in the image when the needle was inserted. The sample was not damaged during this step which indicate that the needle was not touching its surface. This is presented in Figure D5.

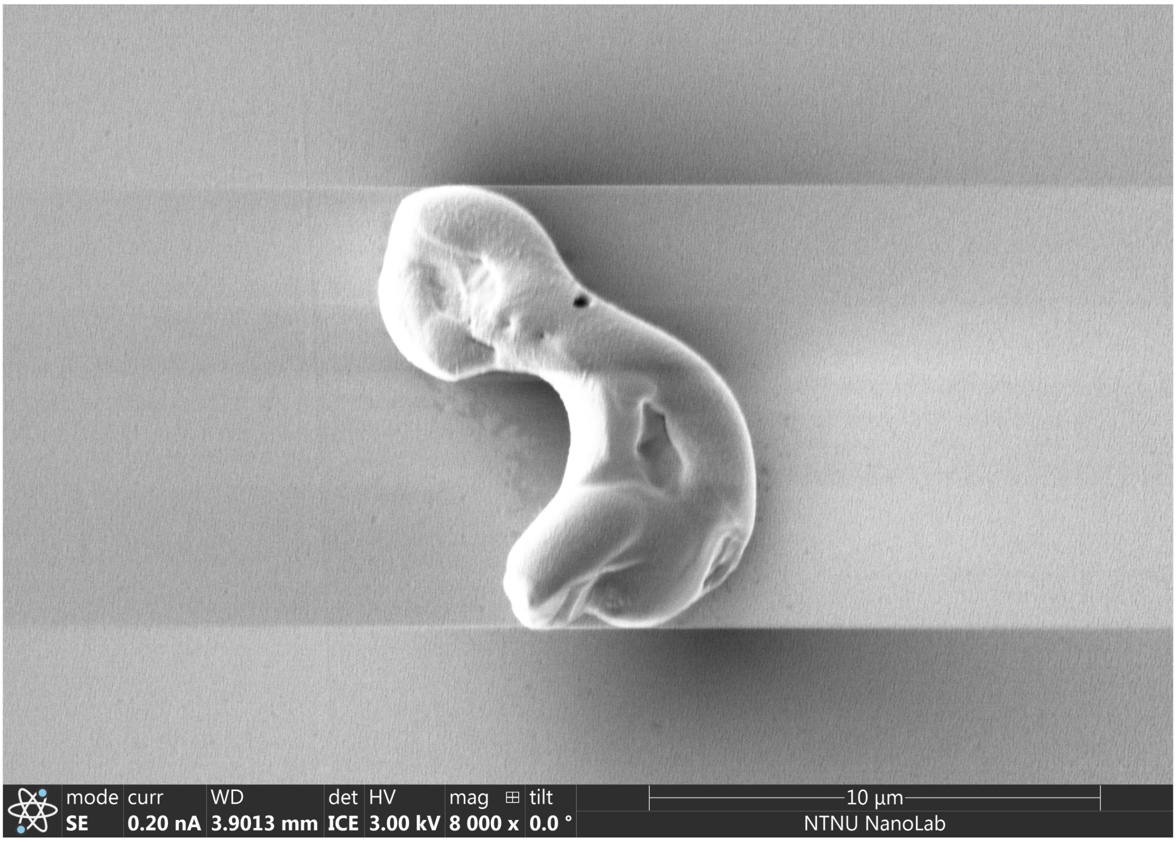

Figure D4: SEM image of charging effects on the surface of a non-conducting TiO_2 film.

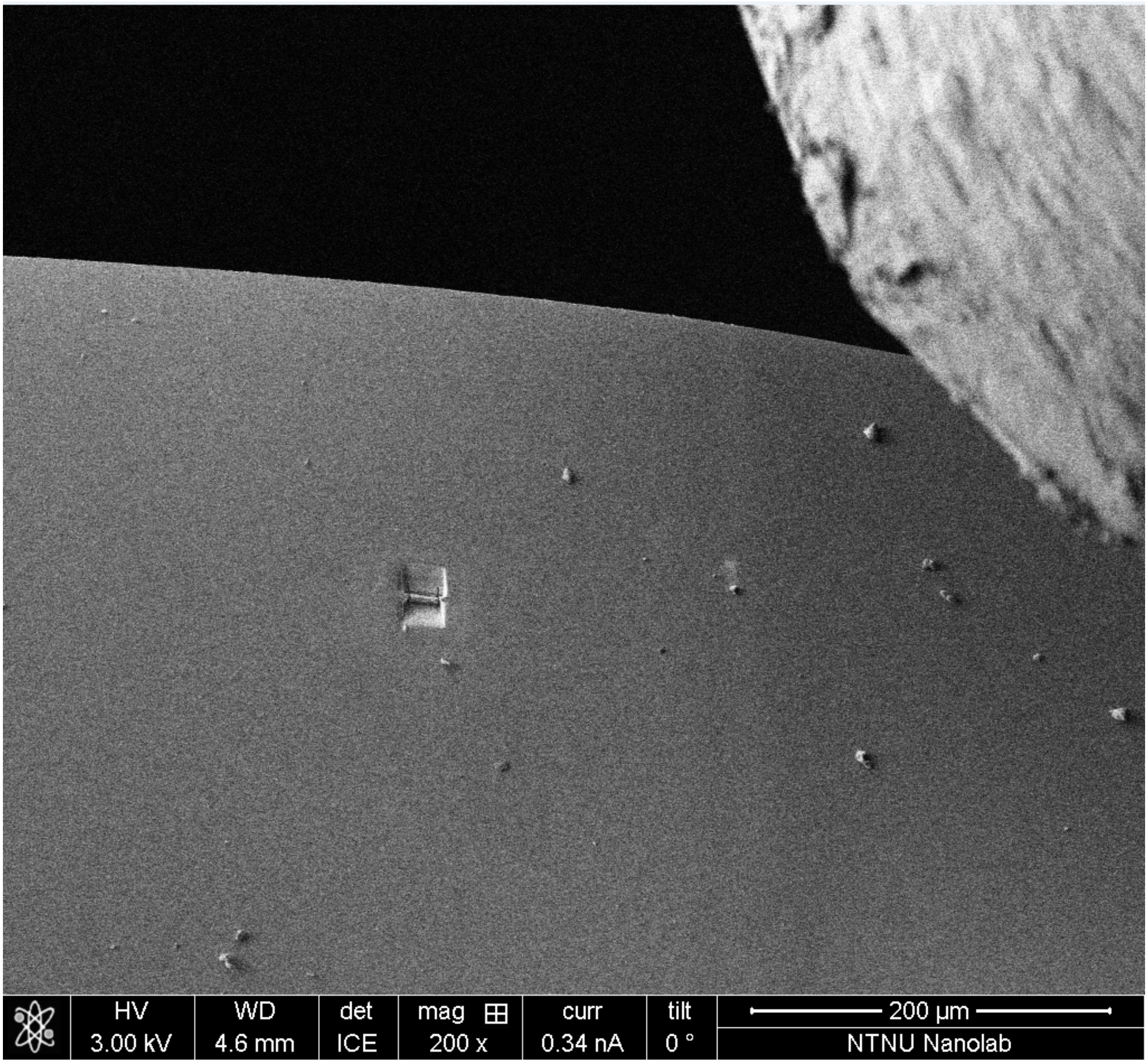

Figure D5: SEM image of charging effects from the GIS needle bending the image.